ACME

ARCHIVES
OF CIVIL AND MECHANICAL
ENGINEERING

Quarterly
Vol. II, No. 2

WROCŁAW 2002

ARCHIVES
OF CIVIL AND MECHANICAL
ENGINEERING

Contents

Spis treści

Shaping of the workpiece surface in single-disc lapping

A. BARYLSKI, M. DEJA

Gdańsk University of Technology, ul. Gabriela Narutowicza 11/12, 80-952 Gdańsk, Poland

Shape errors of the tool exert a dominant influence on the shape accuracy of the workpiece. The correlation between flatness errors of the lap and flatness errors of the workpieces was checked experimentally and determined analytically. Computer model of the workpiece shaping by lapping was developed. Evaluation method of the workpiece orientation as well as some simulation results for a lap with shape errors of convexity and concavity and for a circular workpiece of different diameters are presented in this paper.

Keywords: *lapping, flatness errors, computer model*

1. Introduction

Grinding, polishing, honing, lapping and superfinishing are the most common methods of producing fine surface finishes. Fine surface finish and high dimensional accuracy can be obtained in lapping with the use of relatively simple means of productions. This technology can be used for metallic parts, as well as for non-metallic machine elements, mainly for engineering ceramics which have found use in many engineering applications. The lapping system consists of several elements: lap, lapped sample, abrasive particles, kinematics, and load. They influence the lapping process quality which determines the product quality [1, 4]. Elements of this machining system are characterised by the set of structural, material and surface properties. The lap has an essential influence on the dimensional and shape accuracy. Hardness and microstructure of the material, flatness of an active surface during machining with the simultaneous minimisation of the wear, stiffness, corrosion resistance, the way of grooving, active surface roughness after the facing operations, ability to charge with abrasive are the main properties characterising the lap.

The active surface of the lap has some shape errors of concavity or convexity due to the wear [3, 6]. This exerts the main influence on the shape accuracy of the workpiece. The facing operations could be performed to maintain the flatness of the lapping plate and to correct its shape change. Kinematic method of the correction of the tool shape errors can be also applied. The contact between the workpiece and the tool depends on the lapping kinematics as well as on the workpiece size and shape. Changing the kinematic conditions, e.g. by placing the workpieces at different radii or by setting different rotational velocities, causes that the contact between the workpiece and the tool differs at a specific region of the lap.

2. Kinematics of single disc lapping

The conventional executory system of a single-disc lapping machine is presented in Figure 1. The workpiece (3) loaded against a lap (1) rotating at the angular velocity ω_t is placed in the separator (2) and in the conditioning ring (4). The angular velocity ω_2 at which the conditioning ring is rotating depends on the rotational velocity of the lap, its position on the tool determined by a radius R and on friction conditions in the contact zone. Kinematic parameters of a standard single-disc lapping machine can be changed in a certain range, mainly by changing the position of the workpiece in the separator or by changing the location of the conditioning ring on the lap (closer to the axis of rotation or farther from it).
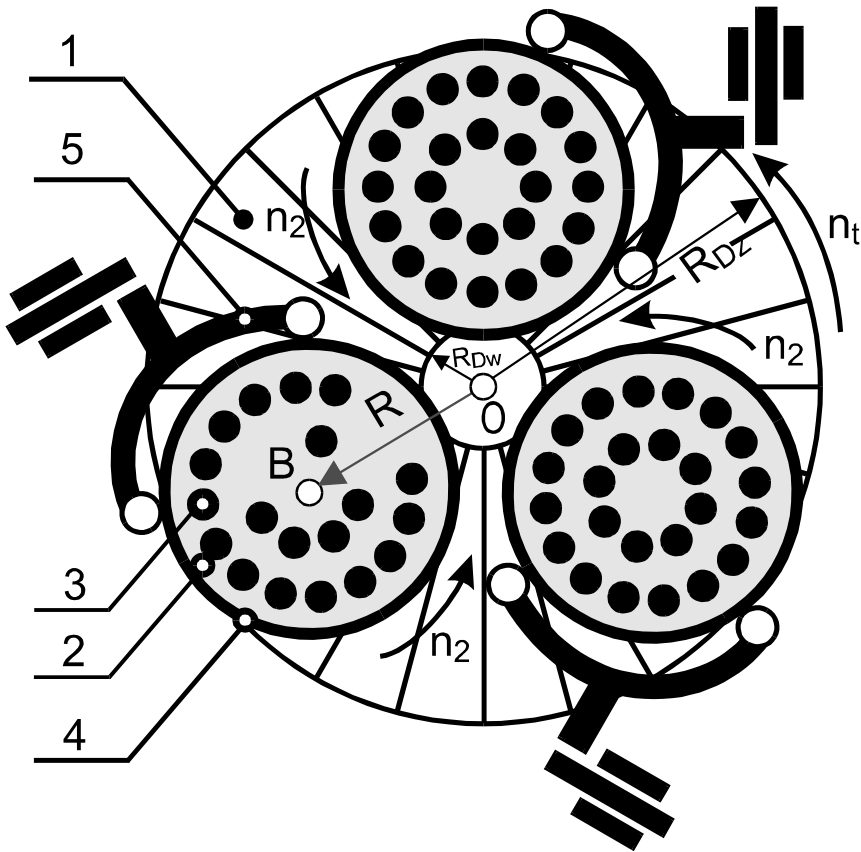
Fig. 1a. General arrangement of executory system of a single wheel-lapping machine:
1 – lap, 2 – separator, 3 – workpiece, 4 – conditioning ring, 5 – leading arm

Displacement trajectories of any point *P* belonging to the surface of the workpiece can be determined in two co-ordinate systems by the equations given in the Table. The relative co-ordinate system (*x–y*) belongs to the rotating lap (Figure 1). Displacement trajectories are the cyclic curves so the lapping velocity and acceleration also change in cycles.

The cycle time is calculated from the equation:

$$T_z = \frac{2\pi}{\left|\omega_j - \omega_2\right|} \; .$$

(1)
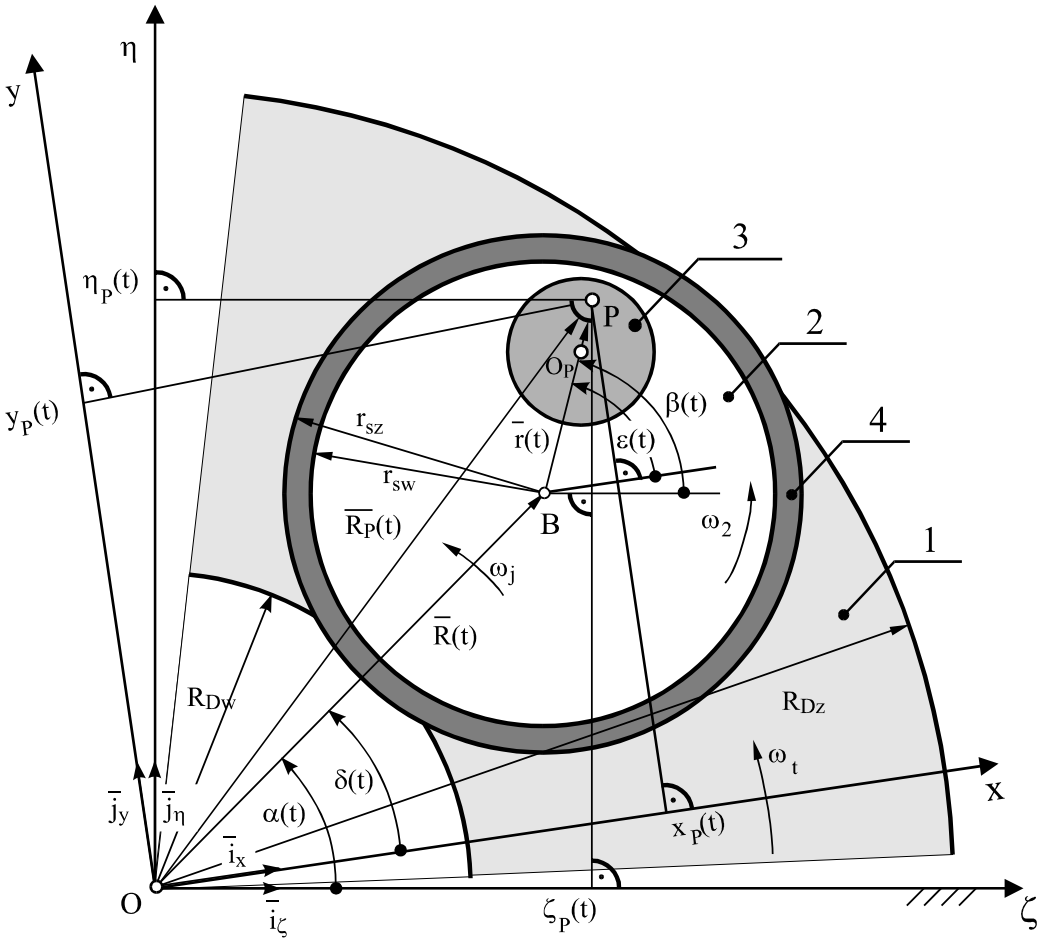
Fig. 1b. Kinematic scheme of executory system of a single wheel-lapping machine:
1 – lap, 2 – separator, 3 – workpiece, 4 – conditioning ring, 5 – leading arm

Table. Equations for displacement trajectories in absolute and relative co-ordinate systems

Absolute ζ–η co-ordinate system	Relative x–y co-ordinate system
$\overline{R_P}(t) = \zeta_P(t)\overline{i_\zeta} + \eta_P(t)\overline{j_\eta}$	$\overline{R_P}(t) = x_P(t)\overline{i_x} + y_P(t)\overline{j_y}$
$\begin{bmatrix} \zeta_P(t) \\ \eta_P(t) \end{bmatrix} = R\begin{bmatrix} \cos\alpha \\ \sin\alpha \end{bmatrix} + r\begin{bmatrix} \cos\beta \\ \sin\beta \end{bmatrix}$	$\begin{bmatrix} x_P(t) \\ y_P(t) \end{bmatrix} = R\begin{bmatrix} \cos\delta \\ \sin\delta \end{bmatrix} + r\begin{bmatrix} \cos\varepsilon \\ \sin\varepsilon \end{bmatrix}$
$\alpha(t) = \omega_j t$ $\beta(t) = \omega_2 t$	$\delta(t) = (\omega_j - \omega_t)t$ $\varepsilon(t) = (\omega_2 - \omega_t)t$

In the computer simulation, the velocity of an arm O–B was set as $\omega_j = 0$ because most of standard lapping machines have such kinematics.

3. Contact between the workpiece and the lap

Kinematics of lapping has an essential influence on the wear of the tool. Change of the kinematic conditions causes that the contact between the workpiece and the tool as well as kinematic parameters differ in specific regions of the lap. The greater the contact intensity is, the higher the wear rate is expected. Most of the simulation models of the tool wear are based on kinematic relations. The form of displacement trajectories depends on the ratio K defined as:

$$K = \frac{\omega_2 - \omega_t}{\omega_j - \omega_t} \,. \tag{2}$$
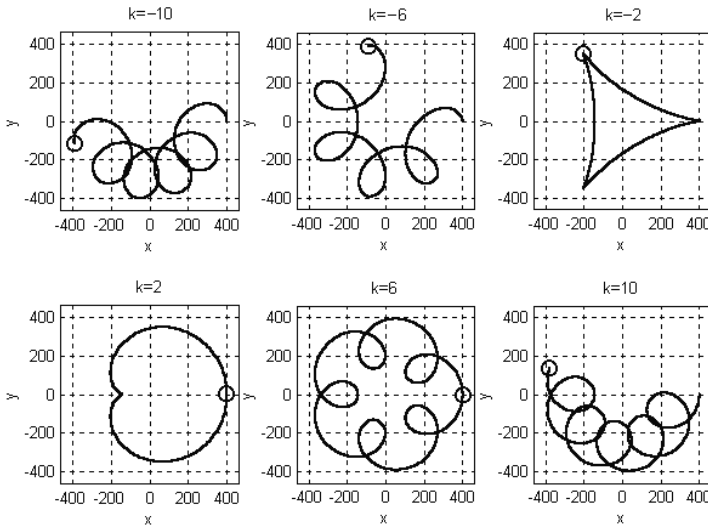
Fig. 2. Displacement trajectories for different values of the ratio K traversed during five cycles

Displacement trajectories for different values of the ratio *K* are presented in Figure 2.

Surfaces of the workpiece and the lap were digitized in order to calculate the contact between the workpiece and the lap. The workpiece area is divided into elementary areas and co-ordinates of their middle points P_{1i} are situated within the workpiece shape (Figure 3). An active surface of the lap is divided into m_1 ring sections (Figure 4) analogously to models described in [12–14].

Fig. 3. Description of the lapped surface by of elementary areas

Fig. 4. Description of the lap's surface for evaluating the wear during
motion of the workpiece divided into elementary areas A_{1i}

The length Δs_{iu} of the trajectory traversed within the area of the ring k_u by the middle point P_{1i} of an elementary area A_{1i} during time $t = t_{kiu} - t_{piu}$ is calculated from the equation:

$$\Delta s_{iu} = \int_{t_{piu}}^{t_{kiu}} v_{P_{1i}}(t)dt. \tag{3}$$

The intensity of the contact g_{1iu} between an elementary area A_{1i} and a ring k_u is expressed by the product:

$$g_{1iu} = A_{1i} \cdot \Delta s_{iu}, \tag{4}$$

where A_{1i} is an elementary area of the workpiece.

The intensity of the contact g_{1u} between the entire surface of the workpiece and the ring k_u is calculated from the equation:

$$g_{1u} = \lim_{n_4 \to \infty} \sum_{i=1}^{n_4} A_{1i} \cdot \Delta s_{iu}, \tag{5}$$

where n_4 is the number of elementary areas A_1 describing the surface of the workpiece.

In the case of equal elementary areas ($A_{1i} = A_1$ for i ranging from 1 to n_4), Equation (5) is simplified to the form:

$$g_{1u} = A_1 \cdot \lim_{n_4 \to \infty} \sum_{i=1}^{n_4} \Delta s_{iu}. \tag{6}$$

The density of the contact between the workpiece and the entire surface of the tool can be determined for all n_4 elementary areas A_1 as a function of the lap radius:

$$d_g(R_D) = \lim_{m_1 \to \infty} \left[A_1 \cdot \lim_{n_4 \to \infty} \sum_{i=1}^{n_4} \Delta s_{iu} \right]_{u=1,\ldots,m_1}. \tag{7}$$

The corrected contact density d_{gp} takes into consideration differences between the areas of the tool rings:

$$d_{gp}(R_D) = \lim_{m_1 \to \infty} \left[\frac{A_1}{2\pi R_{ku} \Delta w} \cdot \lim_{n_4 \to \infty} \sum_{i=1}^{n_4} \Delta s_{iu} \right]_{u=1,\ldots,m_1}, \tag{8}$$

where $\Delta w = R_{kzu} - R_{kwu}$ is the width of the ring k_u.

The contact density distribution can be normalized by the density for the radius $R_D = R$ coming always into contact with all elementary areas during the time of one cycle:

$$d_g'(R_D) = \frac{d_{gp}(R_D)}{d_{gp}(R)} \,.$$

(9)

a)   b)
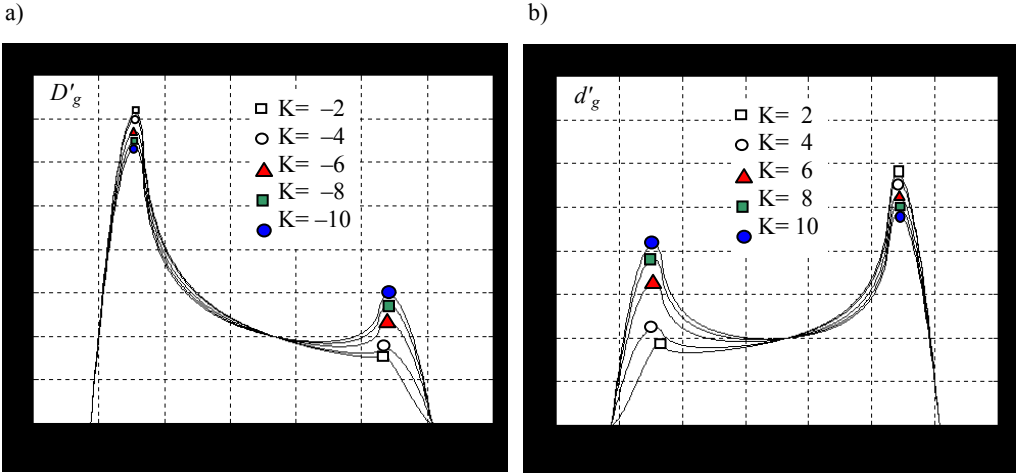
Fig. 5. Computational results of normalised contact density d_g' for: a) $K < 0$, b) $K > 0$; geometrical data used in computer simulations: $R = 273$ mm, $r_P = 20$ mm (ϕ 40), $r_{OP} = 110$ mm, $\Delta w = 1$ mm, $A_1 = 1$ mm^2

a)   b)
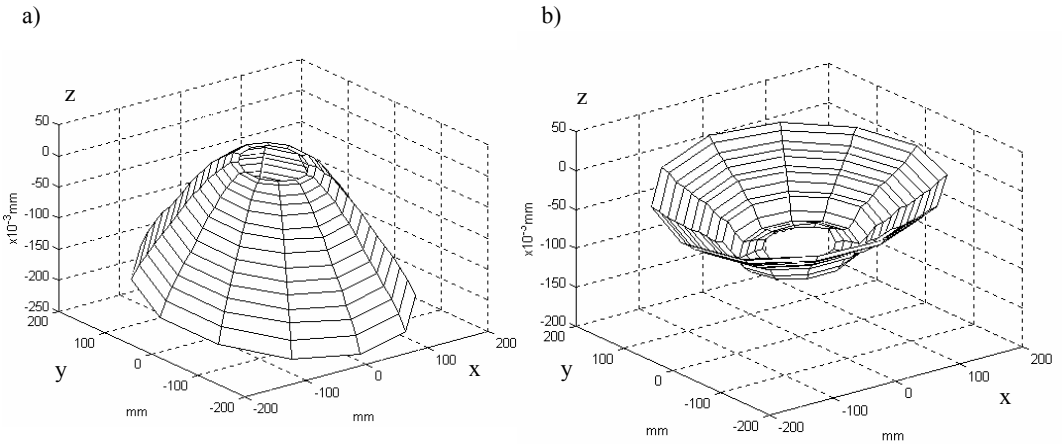
Fig. 6. Examples of an active surface of the tool with flatness errors of: a) convexity, b) concavity

Based on the distribution of the contact density $d_{gp}(R_D)$, the intensity of the wear in a specific region of the tool can be predicted – the greater the contact density is, the higher the rate of the tool wear is expected. A desired distribution of the contact density can be obtained e.g. by choosing an appropriate kinematics of lapping characterised by the coefficient K.

There is a clear dependence between different types of displacement trajectories (the coefficient K) and the distributions obtained (Figure 5).

The change of kinematic parameters results in flatness errors of concavity or convexity on the active surface of the tool (Figure 6).

Flatness errors of the tool exert a decisive influence on the shape accuracy of the workpiece. The workpiece orientation on the lap has to be found in order to calculate the distance between these two bodies. This orientation depends not only on the total shape error of the lap, but also on the shape and size of the workpiece. The movement of the sample on the active surface of the lap is analysed during the time of one cycle divided into several discrete time intervals.

4. Workpiece orientation on the lap

4.1. Evaluation of the equation of the lap surface

The surface of the lap must be described numerically in order to find the workpiece orientation. The equation of the lap surface is found after the measurement of the tool along the radius [2, 5, 6]. The radial profile is estimated by the calculation of the coefficients of a polynomial:

$$f(x) = a_r x^r + a_{r-1} x^{r-1} + ... + a_1 x + a_0, \tag{10}$$

where $a_r, a_{r-1},...,a_1, a_0$ are the searched coefficients.
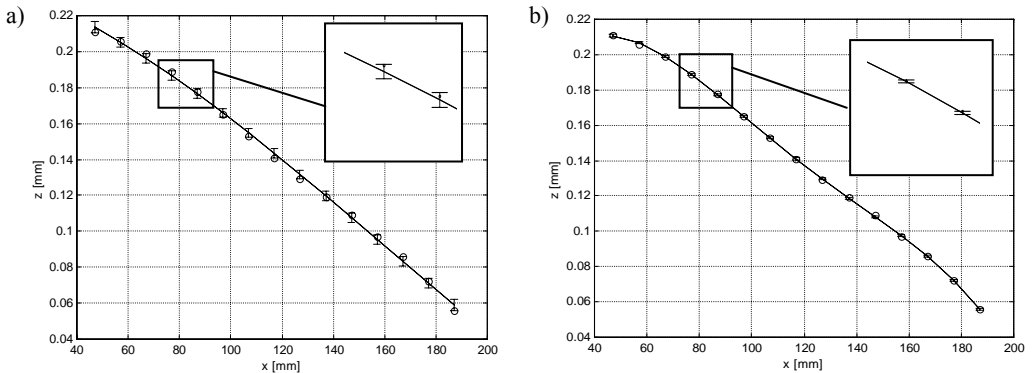
Fig. 7. Fitting the measuring data of a radial lap profile with a polynomial of the degrees:
a) $r = 3$, b) $r = 4$; exemplary error estimates are presented in the zoomed areas

Coefficients of a polynomial $f(x)$ of the degree r that fits the measuring data, $f\{x(i)\}$ to $z(i)$, are found in a least squares sense. The degree of a polynomial can be changed if the error estimations are higher than the acceptable errors. Measuring data can be also fit with the use of a function of any formula. Results of curve fitting with a polynomial of the degrees $r=3$ and $r=4$ are presented in Figure 7.

For the evaluation of the equation of the lap surface the following theorem was applied: if the curve determined in the plane $y=0$ by the equation of a generator $f(x,z)=0$ is symmetrical to the z-axis, then formed surface symmetrical about the z-axis is given by the equation:

$$f(\sqrt{x^2 + y^2}, z) = 0. \tag{11}$$

The surface of the lap, according to Equation (11) and for the generator described by Equation (10), is determined by:

$$a_r\left(\sqrt{x^2 + y^2}\right)^r + a_{r-1}\left(\sqrt{x^2 + y^2}\right)^{r-1} + ... + a_1\left(\sqrt{x^2 + y^2}\right) + a_0 - z = 0. \tag{12}$$

4.2. Evaluation of the workpiece orientation

The distance between the points belonging to the workpiece and the surface of the lap is calculated after finding the orientation of the plane containing the lapped surface. This is done in a few steps presented below with the use of a method applied to estimating the flatness errors, but the lap surface is limited to the area being in contact with the workpiece at the specified time of lapping.

I. Calculation of the x_P and y_P co-ordinates (using equations from Table) of all points P_1 (belonging to the surface of the workpiece) at the specified time t of lapping. The points P_1 of the digitised workpiece are presented on the plane $z=0$ in Figure 8.

II. Calculation of the z_D co-ordinate of analytical points P_D belonging to the surface of the lap using equation of this surface (12) solved for z and generally written as:

$$z_D = f(x_P, y_P). \tag{13}$$

Analytical points $P_D = (x_P, y_P, z_D)$ are used for searching the orientation of the plane containing the lapped surface. These points, located on the exemplary lap surface, are presented in Figure 8.

III. Evaluation of equation of reference and adjacent planes. A general equation of the reference plane is represented by:

$$A_p x + B_p y + C_p z + D_p = 0 \tag{14}$$
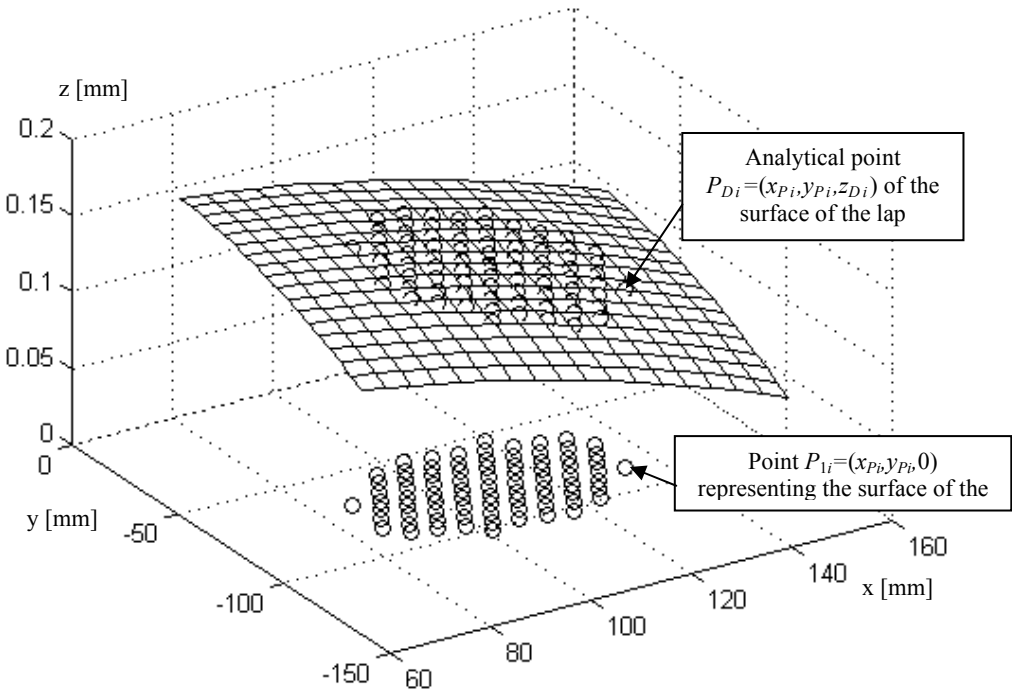
Fig. 8. Determination of the co-ordinates of analytical points P_D belonging
to the surface of the lap (steps I and II of workpiece orientation)

A directional formula of the plane can be obtained after solving Equation (14) for *z*:

$$z = a_P x + b_P y + c_P. \tag{15}$$

The coefficients α_P and β_P relate to the slope of the reference plane in the Cartesian co-ordinate system.

The distance d_o from analytical point P_D (belonging to the surface of the lap) to the reference plane is calculated from the equation (given without a free term c_P of the Equation (15)):

$$d_o = \frac{a_P x_P + b_P y_P - z_D}{\sqrt{a_P^2 + b_P^2 + 1}} . \tag{16}$$

Flatness and straightness errors are always determined in the direction of the *z*-axis [8–11] because of the minimal deviation of adjacent elements from the direction of the *x*- and *y*-axes, so Equation (16) can be simplified to:

$$d_o = a_P x_P + b_P y_P - z_D \,. \tag{17}$$

The orientation of the reference plane corresponds with the location for which a flatness error of the lap's surface limited to the area containing the analytical points $P_D = (x_P, y_P, z_D)$ is determined. A flatness error of this limited area can be evaluated by the function minimisation – the distance T_D between the farthest point from the reference plane and the closest point P_D to it acquires the minimum value:

$$T_D = \min(d_{o\,\mathrm{max}} - d_{o\,\mathrm{min}}) \,, \tag{18}$$

where $d_{o\,\mathrm{max}}$, $d_{o\,\mathrm{min}}$ are maximum and minimum distances between analytical points P_D and the reference plane.

The variables a_P and b_P, characterising the orientation of the reference plane, change at each step of the search for the minimum of the function given by Equation (18). Function minimisation is performed using functions of Optimization Toolbox of MATLAB 5.2, with the algorithm of Nelder–Mead simplex search[*].
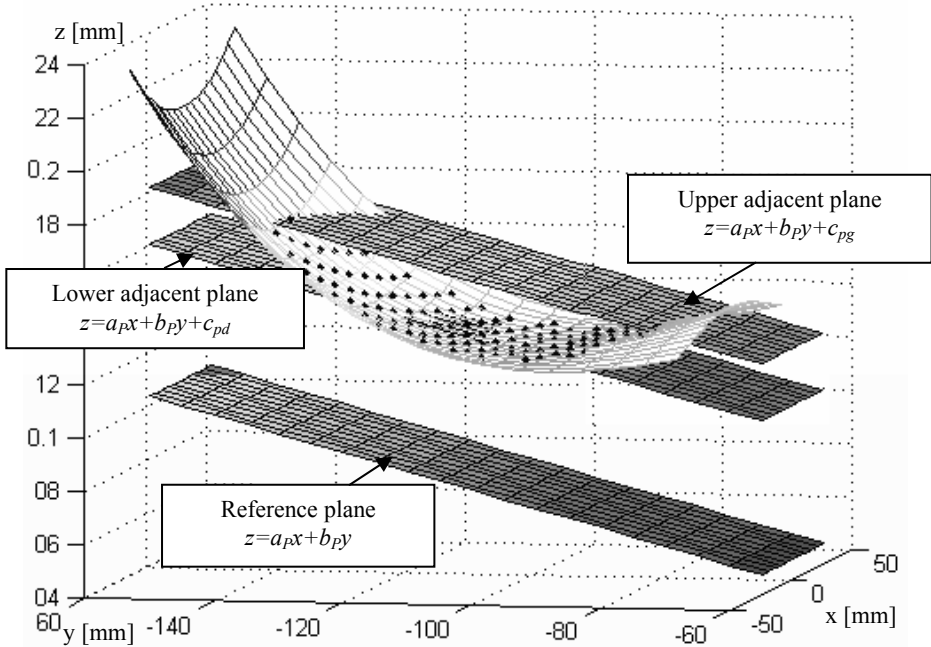
Fig. 9. Characteristic planes used for the calculation of the distance between
the workpiece and the lap (step III of workpiece orientation)

[*]Computation was performed using the computers and software of Academic Computer Centre in Gdańsk.

The exemplary location of the reference plane, evaluated for analytical points belonging to the concave surface of the lap, is presented in Figure 9. A directional formula of the evaluated reference plane is given by the following equation:

$$z = a_P x + b_P y. \tag{19}$$

The slope of adjacent planes is the same as the slope of the reference one. Co-ordinates of the analytical point P_D, the farthest from the reference plane, were used for the calculation of a term c_{pg} of the adjacent plane described by the equation:

$$z = a_P x + b_P y + c_{pg}. \tag{20}$$

A plane containing the point closest to the reference plane is determined by the equation:

$$z = a_P x + b_P y + c_{pd}. \tag{21}$$

The distance between those two planes given by (20) and (21) equals the flatness error of the lap's surface limited to the area containing the analytical points $P_D = (x_P, y_P, z_D)$ (Figure 9).
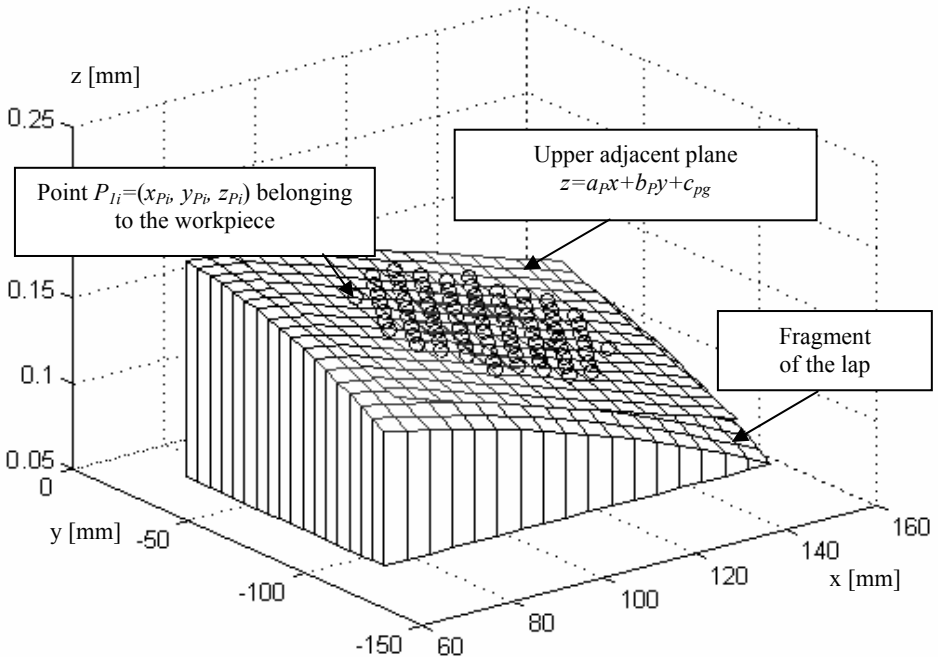
Fig. 10. The orientation of an adjacent plane with a circular workpiece
in the case of a convex lap (step IV of workpiece orientation)

IV. Location of the workpiece on the upper adjacent plane. The points P_1 are contained by the adjacent plane, so the z_P co-ordinate can be calculated from the equation of this plane (20) generally written as:

$$z_P = z_P(x_P, y_P).$$ (22)

The points P_1 of the workpiece located on an adjacent plane in the case of a convex lap are presented in Figure 10.

V. Calculation of the distance between the points P_1 and the lap's surface. It was assumed that the distance between any point $P_{1i} = (x_{Pi}, y_{Pi}, z_{Pi})$ and the lap's surface equals the distance between any corresponding point $P_{Di} = (x_{Pi}, y_{Pi}, z_{Di})$ and the upper adjacent plane. The distance d_p between analytical points P_D and the upper adjacent plane can be calculated from the equation:

$$d_p = \left| \frac{a_P x_P + b_P y_P - z_D + c_{pg}}{\sqrt{a_P^2 + b_P^2 + 1}} \right|.$$ (23)

The following equation can be used for calculating the distance in a direction of the z-axis:

$$d_p = \left| a_P x_P + b_P y_P - z_D + c_{pg} \right|.$$ (24)

5. Computational results

As it was mentioned above, the orientation of an adjacent plane containing the workpiece depends not only on the shape error of the lap, but also on the shape and size of the workpiece. During the computations the lap's surface is limited to the area containing the analytical points $P_D = (x_P, y_P, z_D)$ for each discrete location of the workpiece.

The concave lap for which the calculations were performed is presented in Figure 11a.

The movement of the circular workpiece is analysed and its four discrete locations are shown in Figure 11a. A discrete location for the specified time of lapping $t = (7/20)T_z$ ($T_z = 2.33$ s) and three diameters (ϕ 20, ϕ 40 and ϕ 60) were chosen to illustrate the dependence of the size of the workpiece on the orientation of an adjacent plane. This dependence is shown in Figure 11 b–d. The size of the workpiece clearly influences the slope of the plane determined by the coefficients a_P and b_P given in a legend of Figure 11.

The distance between each point of the workpiece and the surface of the lap depends on the orientation of the adjacent plane containing these points. The dependence

of the distance distribution on tool flatness errors was checked for concave and convex laps. The z' co-ordinates of a concave lap profile (Figure 12) were obtained from the basic one (presented in Figure 7b) after its transformation:

$$z' = -z. \tag{25}$$
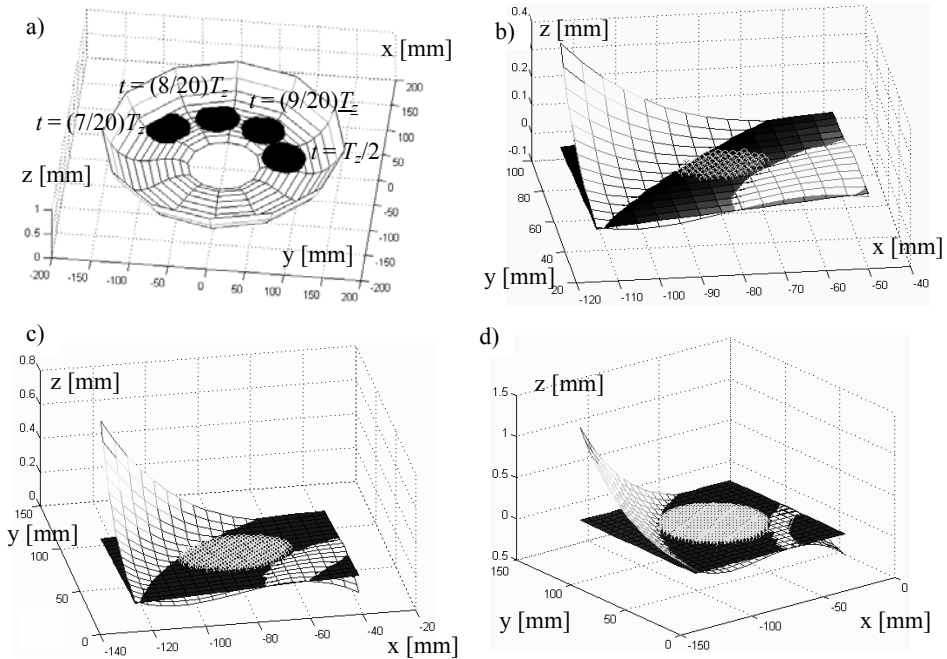
Fig. 11. Orientation of adjacent planes containing a circular workpiece of different diameters for one discrete location determined by the time of lapping $t = (7/20)T_z$, $T_z = 2.33$ s: a) shape of an active surface of the lap with four discrete workpiece locations, b) ϕ 20; $a_p = 0.0012$, $b_p = -0.0010$, c) ϕ 40; $a_p = 0.7448 \cdot 10^{-3}$, $b_p = 0.5947 \cdot 10^{-3}$, d) ϕ 60; $a_p = -0.8351 \cdot 10^{-4}$, $b_p = 0.6385 \cdot 10^{-4}$
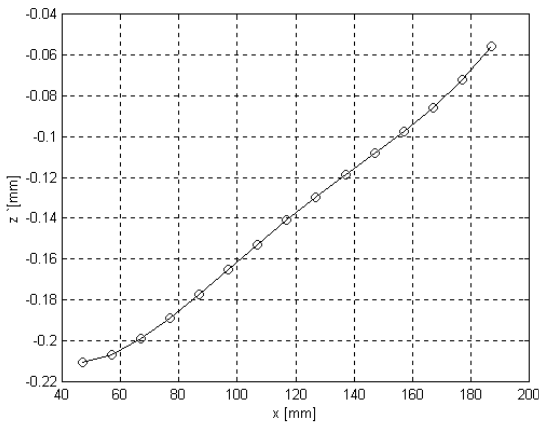
Fig. 12. The radial profile of a concave lap obtained after the transformation of a basic profile presented in Figure 7b

As a result of such transformation the absolute value of the flatness error of a convex lap (Figure 7 b) equals the flatness error of a concave lap (Figure 12).

The average distance (during the cycle time T_z) between the elementary area A_{1i} and the lap's surface is the main variable in a computer model developed for the estimation of the workpiece shape. The distance d_{1i} of the elementary area A_{1i} is calculated as a distance between its middle point P_{1i} and the lap's active surface, using Equation (23) or (24). The cycle time T_z is divided into m_2 time intervals which refer to all discrete locations of the workpiece on the tool. The average distance d_2 is calculated from the equation:

$$d_{2i} = \frac{\sum_{j=1}^{m_2} d_{1ij}}{m_2}, \qquad (26)$$

where:

d_{1ij} – average distance of an elementary area A_{1i} for a discrete location number j,
m_2 – number of time intervals.

Distributions of the distance d_2 for a circular workpiece (ϕ 18) and for a convex tool (Figure 7b) as well as for a concave one (Figure 12) are shown in Figure 13.
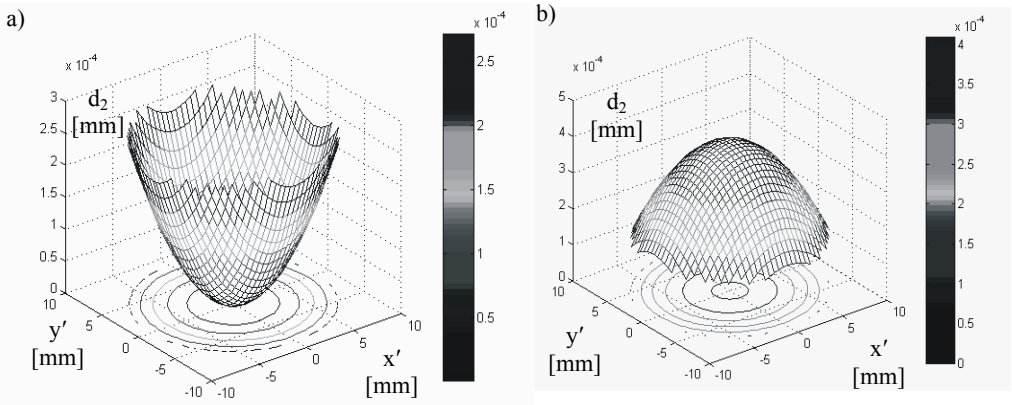
Fig. 13. Distribution of the average distance d_2 between the workpiece (ϕ 18) and the active surface of:
a) convex, b) concave laps; $R = 116$ mm, $r_{OP} = 30$ mm; $n_t = 50$ rpm, $n_2 = 43$ rpm

As it could be expected the point closest to the convex surface of the tool is the central one (Figure 13a). In the case of a concave lap, the central point is the farthest from the lap surface. This results indicate that concave workpieces should be obtained on the convex lap, and convex workpieces on the concave lap. The tendency presented was revealed during experimental tests, but the shape errors of the tool were not mapped exactly by the workpiece (Figure 14).

a)

b)
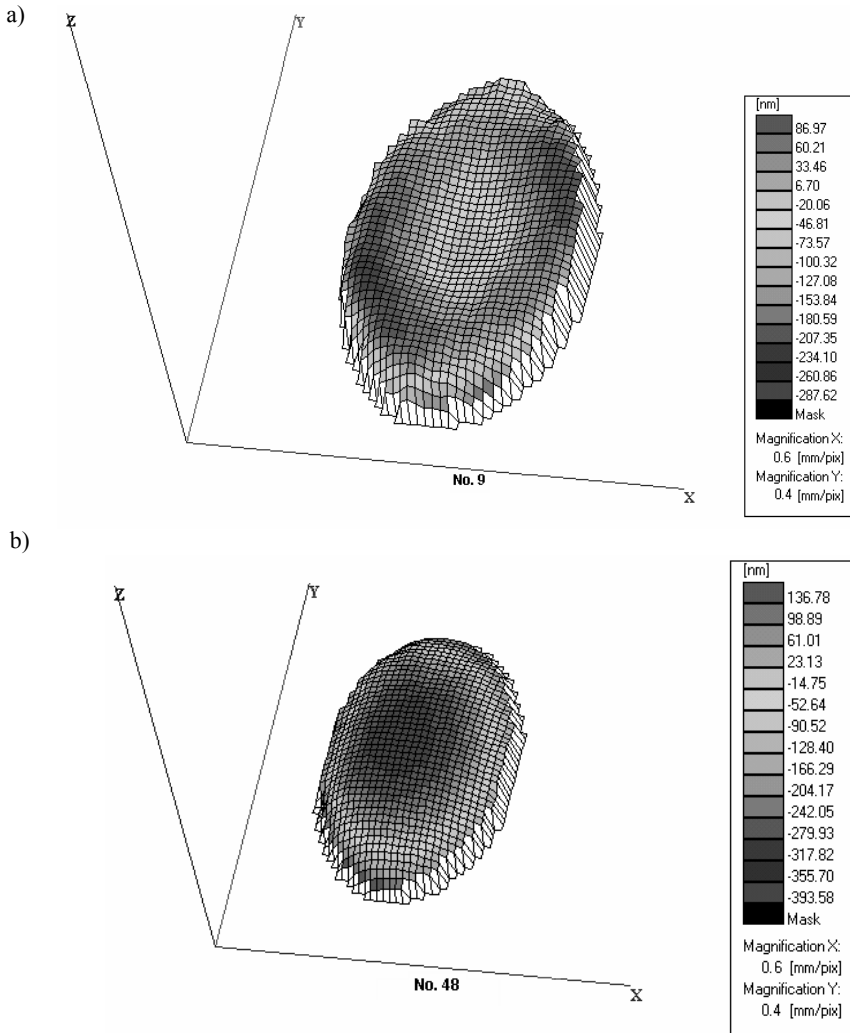
Fig. 14. Workpieces with different shape errors obtained by lapping
with the use of: a) convex, b) concave laps

The action of abrasive grains is more effective in the region of the workpiece edge, so the edge rounding can be observed even after lapping on a flat or a convex lap (Figure 14 a). Taking into account the effect of rounding, another variable, the so-called "edge distance", was evaluated in a computer model developed for the estimation of the workpiece shape [7]. The edge distance is a distance between the elementary area A_{1i} and the workpiece edge calculated in a tangent direction to the displacement trajectory of any point P_{1i}.

Concluding remarks

Computational and experimental results enable formulation of the following conclusions:

- The active surface of the lap has some shape errors of concavity or convexity due to the tool wear. This exerts a dominant influence on the shape accuracy of the workpiece after lapping. The intensity of the wear in a specific region of the tool can be predicted on the basis of the contact density distribution. A desired distribution of the contact density, which allows us to correct the flatness error of the lap, can be obtained by choosing an appropriate kinematics of lapping. The form of displacement trajectories (apart from the velocity and acceleration) exerts a dominant influence on the contact density distribution.

- Two variables: an average distance d_{2i} (during the cycle time T_z) between the elementary workpiece area A_{1i} and the lap surface as well as the edge distance d_{bi} calculated in a the direction tangent to the displacement trajectory are taken into account in a computer model developed for the estimation of the workpiece shape. Generally the flatness errors of the tool are copied by the workpiece, but also the action of abrasive grains (especially in the vicinity of the workpiece edge) must be considered in simulation models.

- Workpiece orientation on the lap has to be found in order to calculate the distance between these two bodies at specified discrete location and to determine the correlation between flatness errors of both surfaces. Description of the workpiece with the use of elementary areas makes it possible to evaluate of the workpiece orientation on an active surface of the lap. This orientation depends on the shape errors of the tool as well as on the size and shape of the workpiece.

- Distribution of the distance d_2 for a circular workpiece has a higher maximum value in the case of a convex lap compared with a distribution for a concave lap with the same absolute value of the shape error. This can explain why the workpiece flatness errors are higher if the concave lap is used, even if the lap concavity is smaller than the shape error of the convex lap.

- Error correlation for prismatic parts was also examined. Detailed analysis, which takes into account different shape errors of the tool, triangular and rectangular workpieces and the broad range of kinematic parameters of single disc lapping, is presented in [7].

- Application of the kinematic correction of the tool's shape errors seems to be easier in double wheel lapping than in single wheel one mainly because of higher possibilities of kinematic control. Experiments will be conducted with a double wheel lapping machine in order to transfer the model evaluated. The computer model of workpiece shaping is to be transferred to grinding with lapping kinematics.

References

[1] Barylski A., Deja M.: *Computer Aided Quality Control of Plane Lapping*, Journal of the Balcan Tribological Association, Vol. 4, No. 1, 1998, pp. 1–7.

[2] Barylski A., Deja M.: *Measurement of the profile wear in lapping using an image processing software*, Proceedings of the 6th ISMQC IMEKO Symposium *Metrology for Quality Control in Production*, Wien, September 8–10, 1998, pp. 35–40.

[3] Barylski A., Deja M.: *Evaluation and simulation of the profile wear of the lap in plane lapping*, Proceedings of the 4th Seminar on Finishing Machining, Gdańsk, 25th September, 1998, pp. 7–14.

[4] Barylski A., Deja M.: *Surface flatness control in single plate lapping*, Proceedings of the XVI IMEKO World Congres IMEKO 2000, September 25–28, 2000, Vienna, Vol. 2, Topic 2 *Photonic Measurements*, pp. 153–156.

[5] Barylski A., Deja M.: *Influence of conditioning rings positioning on the wear of a lap*, Proceedings of the Polnisch–Deutsches Seminar Fertigungstechnologien zur hochgenauen Endbearbeitung, Berlin, 29. Mai 2000, Inst. f. Werkzeugmasch. u. Fabrikbetrieb TU Berlin, 2000, pp. 20–28.

[6] Deja M.: *Zużycie powierzchni czynnej narzędzia w docieraniu jednotarczowym*, Posiedzenie Sekcji Podstaw Technologii KBM w Gdańsku, 6–7 grudnia, 1999, nr 64, s. 33–44, PAN, Komitet Budowy Maszyn, Sekcja Podstaw Technologii.

[7] Deja M.: *Analysis of single-disc lapping in the aspect of required flatness of lapped samples*, Doctoral dissertation, TU Gdańsk 2001, pp. 151.

[8] Huang S., Fan K., Wu J.: *A new minimum zone method for evaluating flatness errors*, Prec. Engineering, Vol. 15, No. 1, 1993, pp. 25–32.

[9] Huang S., Fan K., Wu J.: *A new minimum zone method for evaluating straightness errors*, Prec. Engineering, Vol. 15, No. 2, 1993, pp. 158–165.

[10] Kaiser M., Krishnan K.: *Geometry of the minimum zone flatness functional: planar and spatial case*, Prec. Engineering, Vol. 22, No. 3, 1998, pp. 174–183.

[11] Kanada T., Suzuki S.: *Application of several computing techniques for minimum zone straightness*, Prec. Engineering, Vol. 15, No. 3, 1993, pp. 274–280.

[12] Spur G., Eichhorn H.: *Kinematisches Simulationsmodell des Läppscheibenverschleißes*, IDR, Vol. 31, No. 2, 1997, pp. 169–178.

[13] Spur G., Eichhorn H.: *Untersuchungen zum Verschleiß von Läppscheiben beim Planparallelläppen*, Conference proccedings: Finishing of machine elements, Poznań, April 25, 1995, pp. 59–77.

[14] Spur G., Simpfendörfer D.: *Numerische Vorherbestimmung des Werkzeugverschleißes beim Planläppen*, VDI-Z, Vol. 128, No. 3, 1986, pp. 76–82.

Kształtowanie powierzchni przedmiotu w docieraniu jednotarczowym

Na dokładność kształtową przedmiotów docieranych wpływają głównie błędy kształtu narzędzia. Korelacja między błędami kształtu docieraka a błędami kształtu przedmiotów obrabianych została sprawdzona doświadczalnie i określona analitycznie, co pozwoliło zbudować komputerowy model kształtowania powierzchni docieranych. Przedstawiono sposób wyznaczania intensywności kontaktu między przedmiotem docieranym a docierakiem, opisanym za pomocą pierścieni podziałowych. Opracowano metodę wyznaczania położenia przedmiotu na

docieraku. Opiera się ona na obliczeniu błędu kształtu narzędzia dla kolejnych dyskretnych położeń przedmiotu docieranego. Błąd kształtu jest obliczany dla ograniczonego obszaru docieraka będącego w kontakcie z powierzchnią przedmiotu w dowolnym czasie docierania. Obszar powierzchni narzędzia będącego w kontakcie z przedmiotem poprzez ziarna ścierne zależy od przyjętych parametrów kinematycznych i kształtu przedmiotu. Przedstawiono wyniki symulacyjne położenia przedmiotów o różnych średnicach dla jednakowych współrzędnych środków geometrycznych i dla przypadku docieraka wklęsłego. W artykule przedstawiono obliczenia średniej odległości pomiędzy przedmiotem a narzędziem dla przypadku docieraka wypukłego i wklęsłego. Dla jednakowych całkowitych błędów kształtu narzędzi uzyskano większe odległości w przypadku docieraka wklęsłego. Badania eksperymentalne potwierdziły powstanie większych błędów niepłaskości przedmiotów w przypadku docierania na docieraku wklęsłym w porównaniu z narzędziem wypukłym, nawet przy mniejszych błędach kształtu narzędzia wklęsłego. Opracowane modele pozwalają uzyskać wymaganą płaskość przedmiotów obrabianych – nawet wtedy, gdy istnieją pewne błędy kształtu docieraków – przez zastosowanie odpowiednich parametrów kinematycznych obróbki.

Analysis of photoelastic stress of grinding wheels

W. FIKS

Technical University of Łódź, Stefanowskiego 1/15, 90-924 Łódź

The paper deals with the stress distribution and stress value in grinding wheels with ceramic binding obtained using the method of optically sensitive surface layer. The tests were conducted with the grinding wheels being loaded both statically and with inertial forces existing during rotation of the grinding wheel. The results obtained were compared to those concerning the dynamic strength of grinding wheels carried out with the bursting machine and also to the results of theoretical calculations using FEM. This comparison enables us to estimate the usefulness of a new method and to formulate final conclusions.

Keywords: *grinding wheel, stresses, optical layer*

1. Introduction

Photoelastic method is still widely used in different areas of experimental stress analysis [1−3]. Main advantages of this method are as follows:

• a possibility of measuring a stress at a given point and of observing a stress field as well,

• a possibility of experiments carried out on the models of complex shape and being subject to combined load,

• wide possibility of visual presentation of the results,

• a possibility of a quick, quantitative estimation of an influence exerted by the changes in a shape of the model and in a loading system on the stress state.

One of the methods that enables investigation of static and dynamic strain fields in the surface of a structural member is the method of photoelastic coatings [2].

Several materials which are transparent, when not loaded, display the birefringence of light beam that is proportional to their loading and basically vanishes after unloading. Such materials are called *optically sensitive* and their use in the experimental stress analysis allows us to obtain distinctive fringe patterns of *isochromatics* in a coating of relatively low thickness. One of the basic components of such materials are epoxy resins. Optical anisotropy induced by a load is described by a term *forced birefringence*. The photoelastic analysis starts from a basic assumption that the birefringence effect is unique and linearly related to both stresses and strains.

Generally, a basic principle of the photoelastic method consists in the birefringence of each light beam after its transmission through the optically sensitive layer into two beams situated in the planes of principal directions of stresses. The offset of two beams is proportional to the difference of principal stresses [2−4].

The paper deals with the estimation of the applicability of photoelastic coatings to the determination of magnitudes and distribution of stresses in grinding wheels with ceramic binder.

2. Description of the method applied

A method of the photoelastic coatings has been applied in order to investigate stress state in grinding wheels. Strain state in the outer surface of the structural element is determined on the basis of the test consisting in the transmission of polarised light through the optically sensitive layer (coating) that covers the surface tested.

A scheme of the measurement system using the photoelastic coating method is presented in Figure 1 [2].
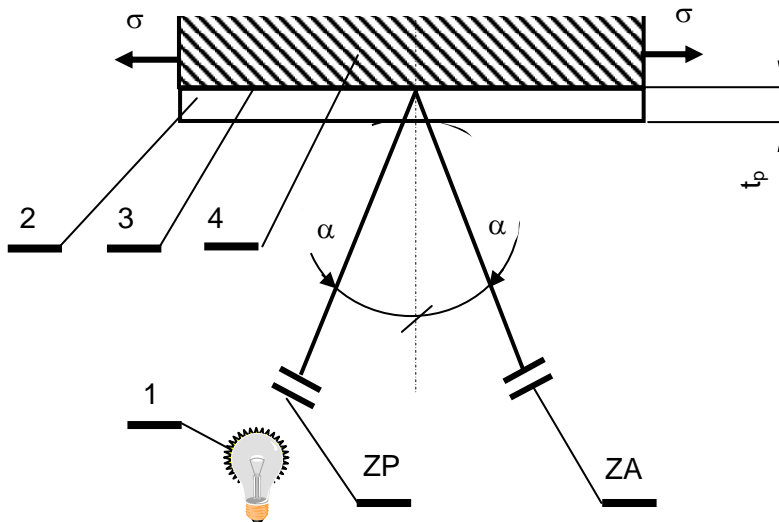
Fig. 1. A scheme of the measurement with using the photoelastic coating; 1 – light source, 2 – photoelastic coating, 3 – reflection layer, 4 – subject of investigation, ZP – polariser set, ZA – analyser set

The light beam from the source 1 passes through the polariser and the photoelastic coating 2 bonded with the flat surface of the tested element 4. The bond layer is simultaneously a reflection layer since it contains an aluminium powder. After the beam is reflected by the third layer it is transmitted trough the analyser which enables us to obtain the birefringence effect and, finally, interference fringe patterns.

When the coating is thin enough and its stiffness can be neglected, as well as on the condition that there exists a perfect contact, a strain in the coating and the outer surface of the tested element is assumed to be the same in the plane of contact.

It is also assumed that the difference in principal strains in the coating ($\varepsilon_{1p} - \varepsilon_{2p}$) is proportional to the difference in principal strains in the outer surface of the element investigated [2]

$$\varepsilon_{1p} - \varepsilon_{2p} = C(\varepsilon_{1e} - \varepsilon_{2e}), \tag{1}$$

where C is the proportionality ratio (for small thickness it can be taken as $C=1$).

The relative phase of the two refracted waves transmitted through the optically sensitive layer and reflected is expressed as

$$\delta = m \cdot \lambda = 2t_p \cdot K \left(\varepsilon_{1p} - \varepsilon_{2p} \right), \tag{2}$$

where:

K – photoelastic coefficient of optically sensitive layer,

λ – wavelength of the light used in the polariscope.

The difference in principal strains in the photoelastic coating can be expressed by means of isochromatic fringe order m

$$\varepsilon_{1p} - \varepsilon_{2p} = f \cdot m, \tag{3}$$

where f is the coefficient expressing a relative strain value per unit isochromatic fringe order.

According to Hooke's law for plane stress state, the difference in principal stresses is related to the difference in principal strains in the following way

$$\sigma_{1p} - \sigma_{2p} = \frac{E_p}{1+\nu_p} (\varepsilon_{1p} - \varepsilon_{2p}). \tag{4}$$

After insterting relation (3) into (4) we obtain

$$\sigma_{1p} - \sigma_{2p} = \frac{E_p}{1+\nu_p} f \cdot m, \tag{5}$$

and subsequently

$$f = \frac{E_p}{1+\nu_p} \cdot \left(\frac{\sigma_{1p} - \sigma_{2p}}{m} \right), \tag{6}$$

$$k_\delta = \frac{\sigma_{1p} - \sigma_{2p}}{m}, \tag{7}$$

where k_δ is the material coefficient of optically sensitive layer.

In the same way, one can relate the principal strains on the surface of the structural element to the principal stress

$$\sigma_{1e} - \sigma_{2e} = \frac{E_e}{1 + v_e} \left(\varepsilon_{1e} - \varepsilon_{2e} \right). \tag{8}$$

Since a difference in principal strains of the photoelastic coating and a difference in principal strains in the surface of the element tested are similar (1), knowing the Young modulus E_e, the Poisson ratio v_e and also f and C, as well as isochromatic fringe order at the certain point, we can calculate a difference in principal stresses on the surface of the element tested

$$\sigma_{1e} - \sigma_{2e} = \frac{E_e}{1 + v_e} \cdot \frac{f \, m}{C} . \tag{9}$$

In order to determine the stress components, we have to know not only the difference in principal stresses (9), but also the direction of principal stresses – angle of isoclinics and their boundary values as well [4]. For example, on a free edge of a *disc* being under in-plane load (edge of a hole) the additional data is a zero-value of one of the principal stresses.

3. Experimental investigations

Experimental investigations were carried out using the photoelastic coating method. The tests were conducted on half-ring specimens (half of the grinding wheel) subject to static three-point bending [5–6] or on rotating grinding wheels subject to dynamic inertial forces. The tests were performed on the experimental stand equipped with the polariscope for reflection of light. The polariscope consisted of circular and linear polarizers as well as of compensation analyser used for isochromatic order compensation. The fringe patterns were registered using the digital camera "Canon" type XM1 with the helical scanning system and two rotating heads for image recording. In order to obtain a proper focus of rotating grinding wheel, a 1/500 second shutter was applied.

A photoelastic coating (of 2 mm thickness, the Young modulus E_p=3450 (MPa) and the Poisson ratio v_p=0.35, was put on half-rings and grinding wheels.

A model photoelastic coefficient k_δ was determined for the material of the optically sensitive layer. Its value depended on:

- coating thickness,
- light source (wavelength λ),
- optical sensitivity of the material.

For the material used in the test it amounted to

$$k_\delta = 0.59 \left(\frac{MPa}{\text{unit fringe ord.}} \right).$$ (10)

Then, using relation (6), the coefficient *f* expressed by (3) was calculated based on elastic properties of the photoelastic coating material:

$$f = \frac{1 + \nu_p}{E_p} \cdot k_\delta.$$ (11)

After inserting the data into relation (11) the following value was obtained

$$f = 2.31 \cdot 10^{-4} \left(\frac{1}{\text{unit fringe ord.}} \right).$$ (12)

After a series of tests during which the specimens (half-rings) coated with the optically sensitive layer were loaded, fringe orders were determined from the isochromatic fringe patterns and subsequently the stresses in the half-rings tested were calculated.
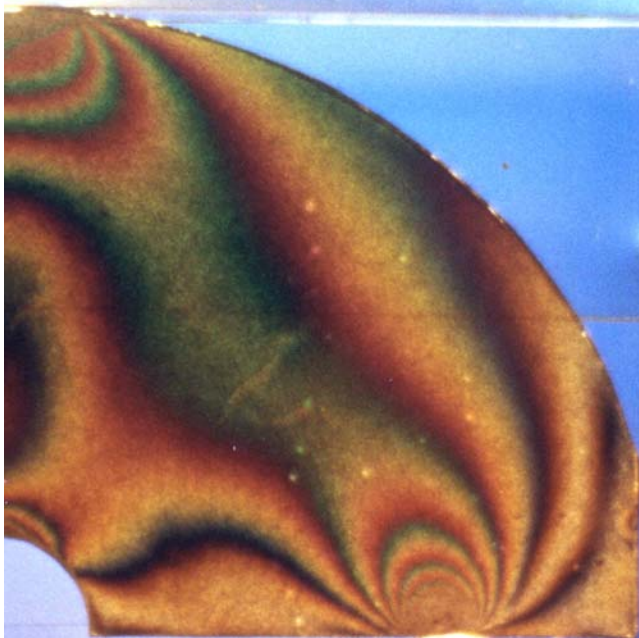
Fig. 2. Isochromatic fringe patterns in half-ring under the load $P = 10.5$ (kN)

In Figure 2, isochromatic fringe patterns are shown in the half-ring 99A 120M being under the load $P = 10.5$ (kN). The maximum fringe order shown in Figure 2 is 5. Using formulae (4), (5) and assuming $\varepsilon_{2p} = -\nu\varepsilon_{1p}$, the maximum strain was calculated

$$\varepsilon_{1\max} = \frac{f}{1+\nu_p} \cdot m . \tag{13}$$

After inserting the data it amounts to

$$\varepsilon_{1\max} = 8.55 \cdot 10^{-4} . \tag{14}$$

For the plane stress state (assuming that $\sigma_2 = 0$) from Hooke's law we obtain

$$\sigma_{1\max} = E_e \cdot \varepsilon_{\max} . \tag{15}$$

For the half-ring 99A 120 M 6, the Young modulus amounted to $E = 48280$ (MPa) [6]. Thus, maximum stress at the hole of the half-ring determined using the photoelastic method was

$$\sigma_{1\max} = 41.28 \ \left(\text{MPa}\right). \tag{16}$$

The results obtained were compared with theoretical isochromatic (isolines of difference in principal stresses) patterns received from the FEM programme ANSYS 5.6.2.
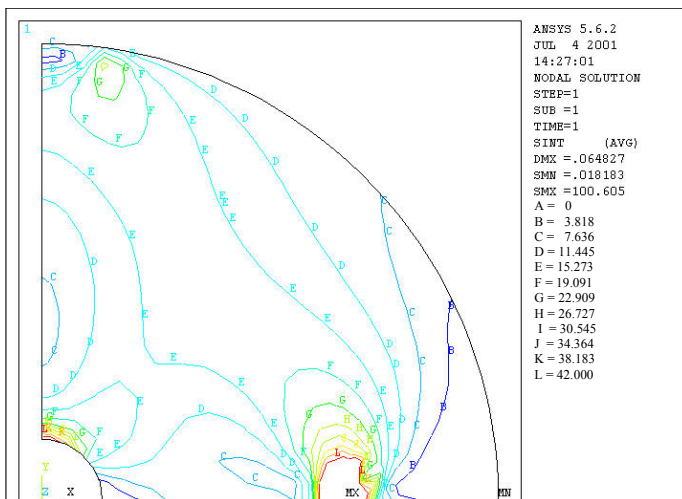
Fig. 3. Theoretical distribution of isochromatics in half-ring under to the load $P = 10.5$ (kN)

In Figure 3, theoretical distribution of isochromatics is shown for the half-ring 99A 120 M 6 under the load $P = 10.5$ (kN). The maximum stresses along the line L reached the value of 42 (MPa), where they were very close to $\sigma_{1\,max} = 41.28$ (MPa).

Fig. 4. Isochromatic fringe patterns at the hole of the grinding wheel
rotating at the angular speed of 1150 (1/s)
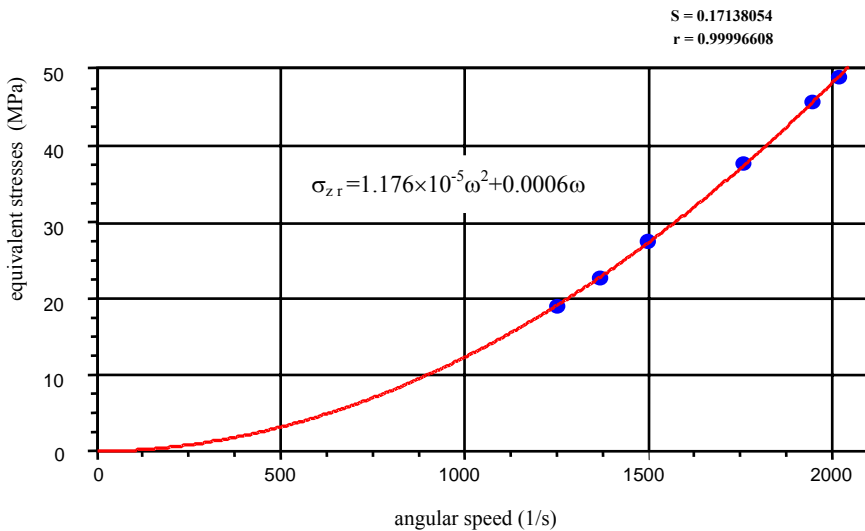
Fig. 5. Influence of the angular speed on equivalent stresses in grinding wheels

Isochromatic fringe patterns in grinding wheels subject to inertial forces were observed using the photoelastic coatings under the same conditions as in the case of half-rings.

Figure 4 shows the isochromatic fringe patterns in the photoelastic coating put on the surface of grinding wheel of the characteristics 150×13×20 99A120M6. The wheel rotated at the angular speed $\omega = 1150$ (1/s). In the example shown, the maximum fringe order was $m = 2$. Thus, the maximum strain according to (13) amounted to

$$\varepsilon_{1\max} = 3.42 \cdot 10^{-4}, \tag{17}$$

while the maximum stress according to (15) was

$$\sigma_{1\max} = 16.5 \; \left(\mathrm{MPa}\right). \tag{18}$$

Magnitudes of stresses in the rotating wheel obtained from the photoelastic experiment were compared with those obtained from theoretical calculations using the finite element method. In Figure 5, a diagram of equivalent stresses in terms of angular speed of the grinding wheel of the characteristics 99A 120 M 6 (taken from [5]) is presented. The diagram shows that for the angular speed $\omega = 1150$ (1/s), residual stresses reach the value of 15.8 (MPa) which is close to the maximum value $\sigma_{1\max} = 16.5$ (MPa) obtained using the photoelastic method (the relative error amounts to ca. 4%).

4. Conclusions

The presented method of photoelastic coatings proved to be useful for determining the magnitudes and distributions of stresses in the half-rings and grinding wheels tested. The stresses determined using this method were comparable with those obtained from finite element method. Similar results were also obtained using the strain gauge method [5–6].

Undoubtedly, a significant advantage of the method of photoelastic coatings is the possibility of obtaining a field information about the stress distribution in the whole area of the element tested. However, a disadvantage is a time-consuming process of the preparation of photoelastic coatings, particularly the process of its putting on the surface.

Thus, the applicability of optically sensitive layers seems to be limited, especially for rotating elements due to the necessity of using special cameras and other equipment. Nevertheless, this method can be applied in laboratories in order to visualize the stress fields in grinding wheels loaded with inertial forces and being under external loads.

References

[1] Cudny W., Dyląg Z., Orłoś Z.: *Application of Polarised Light and Optically Sensitive Materials to Large Strain Analysis*, Proceedings of the International Symposium on Mechanics of Inelastic Media and Structures, PWN, Warszawa, 1982.

[2] Dyląg Z., Orłoś Z.: *Niektóre zastosowania i techniki badań elastooptycznych*, PWN, Warszawa, 1977.

[3] Orłoś Z.: *Doświadczalna analiza odkształceń i naprężeń*, PWN, Warszawa, 1977.

[4] Dyląg Z., Jakubowicz A., Orłoś Z.: *Wytrzymałość materiałów*, WNT, Warszawa, 1997.

[5] Fiks W.: *Wytrzymałość dynamiczna ściernic ceramicznych*, Sekcja Podstaw Technologii Komitetu Budowy Maszyn PAN, XXI Naukowa Szkoła Obróbki Ściernej, Warszawa, 1998, s. 43–46.

[6] Fiks W.: *New Method for Investigation of Strength Properties of Grinding Wheels with Ceramic Binders*, Advances in Manufacturing Science and Technology, Vol. 26, No.1, 2002, pp. 81–98.

Badania elastooptyczne naprężeń w ściernicy

Przedstawiono wyniki badań dotyczących rozkładu i wartości naprężeń w ściernicach ze spoiwem ceramicznym, otrzymywane metodą optycznie czułej warstwy powierzchniowej. Badania przeprowadzono ze ściernicami obciążanymi statycznie (półpierścienie) oraz siłami bezwładności występującymi podczas wirowania ściernicy. Wyniki porównano z wynikami badań tensometrycznych, a także z wynikami obliczeń teoretycznych metodą elementów skończonych. Porównanie pozwoliło ocenić przydatność zaproponowanej metody.

Metrological characteristic and results of testing a measuring equipment for evaluation of cutting properties of superhard wheels

A. GOŁĄBCZAK, T. KOZIARSKI

Technical University of Łódź, ul. Stefanowskiego 1/15, 90-537 Łódź

In the paper, results of research concerning new measuring equipment for evaluation of cutting properties of superhard grinding wheels under production conditions are described. The results presented are focused on the selection of conditions for measurement and repeatability of the measurement. The sensitivity of the parameters being measured to variation of dressing conditions of CBN grinding wheels has also been checked.

Keywords: *superhard grinding wheels, cutting ability, measuring equipment, metrological characteristic*

1. Introduction

Grinding wheels with diamond or cubic boron nitride abrasives, also called *superhard grinding wheels*, have nowadays the best operational properties [1–4]. In order to use these superhard grinding wheels in economical way, it is necessary to supervise variations in their cutting ability during grinding process. This is a basis for decision-making process concerning dressing operation.

In industry, most of grinding machines are not equipped with any device which would allow evaluation and supervision of grinding wheel cutting ability, especially in the case of tool grinders. Decisions about selection of an appropriate moment for dressing operation still have been made by the operator. He decides when to start dressing process on the basis of his observations of workpiece (shape and dimensions) and the grinding wheel. This method however should not be recommended in the case of superhard wheels, where variation of their cutting ability is difficult to notice. Unnecessary dressing leads to high costs due to wear of the wheel and dressing tool. On the other hand, too late dressing can generate several undesirable changes in ground surface. The result of too late dressing, when machining with superhard wheels, can be serious, although not always visible, mainly because of possible stress in ground surface.

In the publications, there are a lot of laboratory methods for the examination of grinding wheel cutting ability [5–10]. They consist in direct and indirect descriptions of the glazing of grinding wheels. Direct methods describe: roughness of ground surface, residual stress in surface layer, microhardness of ground surface, ground surface colour, workpiece shape and dimension deviations and grinding wheel topography.

Indirect methods examine: grinding force components, grinding power, specific grinding energy, grinding temperature, chatter amplitude of machine–tool–fixture– workpiece system, acoustic emission and wheel saturation with grinding process waste. However, these methods are difficult to apply in industry due to limitation of equipment, technology, staff and methodology. Therefore an objective method for evaluating the cutting ability of superhard wheels is necessary, especially in industry.

The test, which have been carried out at Technical University of Łódź, may help to solve the problem of evaluation and supervision of superhard wheel cutting ability under industrial conditions [11–15]. Their results show that cutting ability of such grinding wheels can be evaluated using the method proposed, based on a few-seconds grinding test of special tester (thermocouple) under constant grinding conditions, outside grinding zone. As a result of grinding test, two basic parameters are determined:

• length decrement of the tester, described by the cutting ability factor Q'_t [µm/s], measured during movement of the tester towards the wheel with constant force,

• average grinding temperature of the ground tester Θ'_t [°C] measured during movement of the tester towards grinding wheel with constant speed.

Suitability of the above factors for cutting ability evaluation was checked on model stand [12–14]. Good results achieved at the model stand allowed a development of new measuring equipment, which might be applied in supervision of cutting ability of superhard wheels in industry. In the paper, the construction of measuring equipment, experimental results of its metrological characteristic and assessment of cutting ability of CBN grinding wheel in variable dressing conditions have been presented.

2. Measuring equipment

The scheme of construction of equipment for measuring and recording the parameters Q'_t, and Θ'_t is depicted in Figure 1. Tester *5* is connected with force sensor *6* fixed to a saddle *9* with bearing system, which makes precise movement towards the grinding wheel possible. The movement of the tester towards grinding wheel is realised by stepper motor *7*, belt (gear) transmission *8* and screw-rolling transmission *10*. The force sensor *6* enables permanent control of tester grinding force and tester movement in feedback path. Measuring cycle of the parameters Q'_t, Θ'_t is controlled by computer *12* equipped with multifunction DAS card and realised by computer program in two modes. The first mode concerns measurement of the factor Q'_t. In this mode, the tester is pressed towards the wheel with a constant force. Speed of the tester is controlled by force sensor, computer and stepper motor controller. In the second mode, the temperature of ground tester (Θ'_t) is measured. During this measurement the thermocouple travels towards grinding wheel with a constant speed. The speed is controlled by stepper motor and computer.
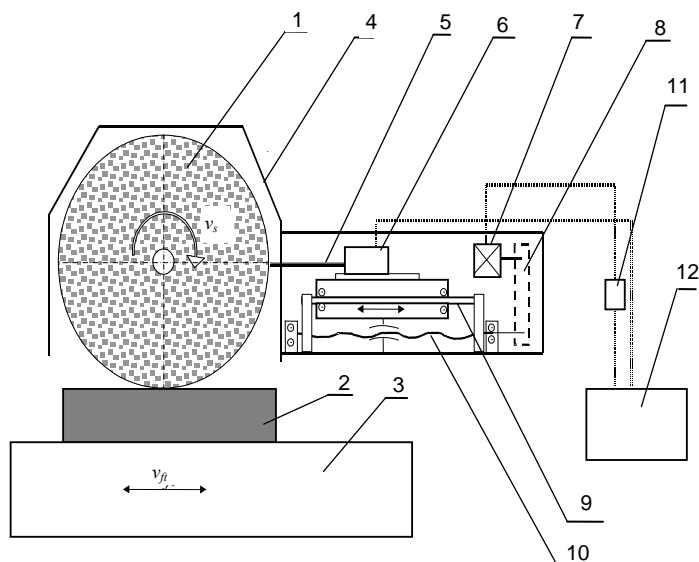
Fig. 1. The scheme of measuring device for evaluation of superhard wheel cutting ability: 1 – CBN wheel, 2 – workpiece, 3 – grinder's table, 4 – fast headstock, 5 – tester (thermocouple), 6 – force sensor, 7 – stepper motor, 8 – belt transmission, 9 – saddle, 10 – screw-rolling transmission, 11 – stepper motor controller, 12 – computer, v_s – grinding wheel peripheral speed, v_{ft} – tangential feed speed

3. Experimental

3.1. Metrological characteristic of measuring equipment

Investigations of metrological properties of measuring equipment have been carried out using surface grinder SPG – 30×80. The range of investigations included determination of reliable measuring conditions of the factors Q'_t and Θ'_t, i.e.: time-constant of measuring equipment, force and speed of the tester pressed towards the wheel, time of grinding of the tester and assessment of the accuracy of the measurement.

Conditions of measurement of cutting ability factors have been determined on the grounds of the tests of measuring equipment. These tests consisted in realization of series of measurements of indexes of cutting ability of CBN grinding wheel (1A1-1 350×20×127×5 LKU50 125/100 ST1K27 C100). The measurements were carried out for different values of the movement force of the tester towards the wheel (F_N = 8–12 N) and different movement speeds of the tester (v_{ft} = 500–2000 μm/s). Examplary results of measurement of the factors Q'_t and Θ'_t (recorded during tests of the measuring equipment) are presented in Figures 2 and 3.

Analysis of the diagrams (Figures 2 and 3) indicates that stable grinding process of the tester begins after the time T_0, the so-called time constant of the measuring equipment. The values of the time constant were established for different conditions of grinding of the tester. The values of the time T_0 are presented in Table 1.

a)

b)
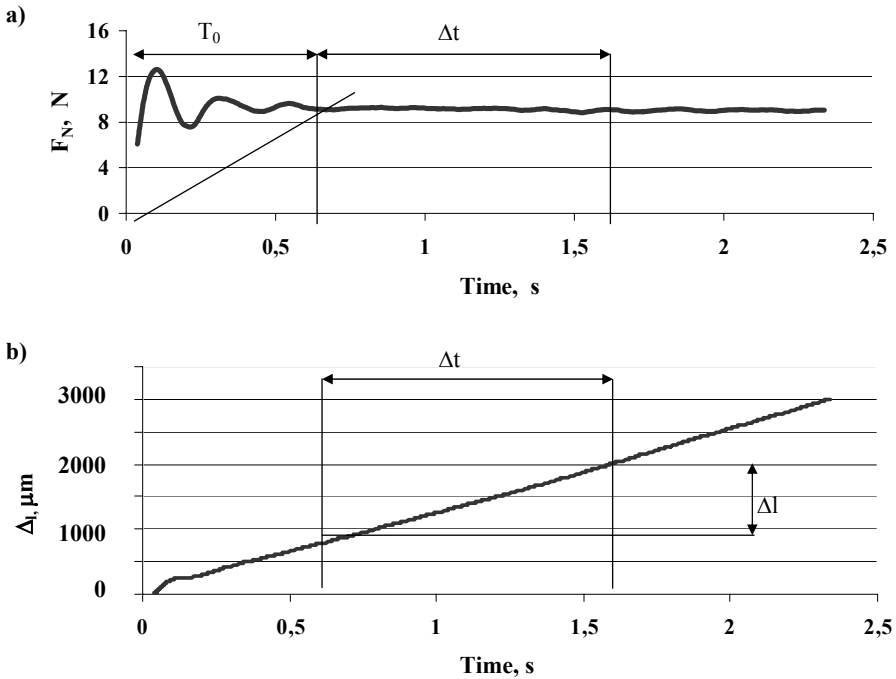
Fig. 2. Results of measurement of the index Q'_t: a) movement force of the tester
towards the wheel ($F_N = 10$ N), b) length decrement Δl of the tester
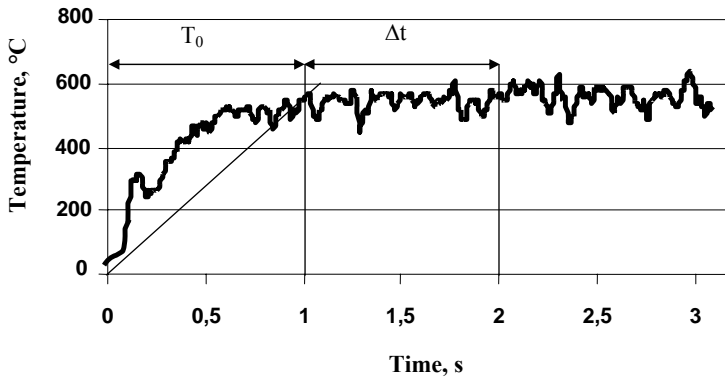
Fig. 3. Results of measurement of the grinding temperature Θ'_t of ground tester; $v_{ft} = 1000$ μm/s

The results of the tests made it possible to determine the time of grinding Δt of the
tester, which ensured a proper measurement of the factors Q'_t and Θ'_t. The results of
measurement of these factors for different time of grinding Δt of the tester are also
shown in Table 1.

Table 1. Conditions of testing the of measuring equipment

Time constant T_0			
Measurement of factor Q'_t		Measurement of factor Θ'_t	
Movement force of the tester F_N [N]	Time constant T_0 [s]	Movement speed of the tester v_{ft} [μm/s]	Time constant T_0 [s]
8	1.2	500	1.5
10	0.6	1000	1.0
12	0.5	2000	0.8
Grinding time of the tester Δt			
Measurement of factor Q'_t		Measurement of factor Θ'_t	
Δt [s] / Q'_t [μm/s] / Standard deviation S [μm/s] / Relative error [%]		Δt [s] / Θ'_t [°C] / Standard deviation S [°C] / Relative error [%]	

Δt [s]	Q'_t [μm/s]	Standard deviation S [μm/s]	Relative error [%]	Δt [s]	Θ'_t [°C]	Standard deviation S [°C]	Relative error [%]
0.5	1148	69.9	6.1	0.5	492	30.2	6.1
0.7	1196	66.2	5.5	0.7	516	24.0	4.6
1	1137	40.2	3.5	1	524	20.1	3.8

Influence of conditions of tester grinding							
Measurement of factor Q'_t				Measurement of factor Θ'_t			
Movement force of the tester F_N [N]	Q'_t [μm/s]	Standard deviation S [μm/s]	Relative error [%]	Movement speed of the tester v_{ft} [μm/s]	Θ'_t [°C]	Standard deviation S [°C]	Relative error [%]
8	698	107.9	15.50	500	286	27.3	10
10	1192	50.3	4.2	1000	532	34.9	6.5
12	1442	77.2	5.35	2000	705	54.0	7.7

Grinding wheel: 1A1-1 350×20×127×5 LKU50 125/100 ST1K27 C100

Shape and dimensions of the tester
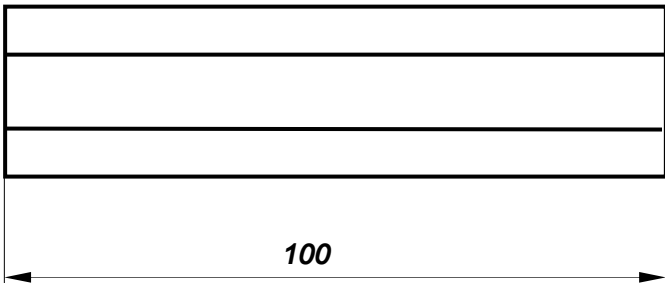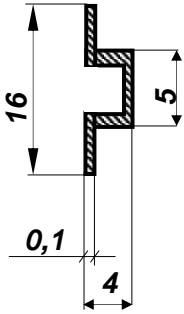
Material of the tester: toughened chromium steel: 6H13

Making an assumption that an acceptable measuring error of the factors Q'_t and Θ'_t is less than 5%, the time of grinding Δt of the tester is equal to 1 s.

The conditions of grinding of the tester, i.e. the values of force and speed of the movement of the tester towards the wheel, have been determined on the basis of the investigations obtained, which are presented in Figures 4 and 5.
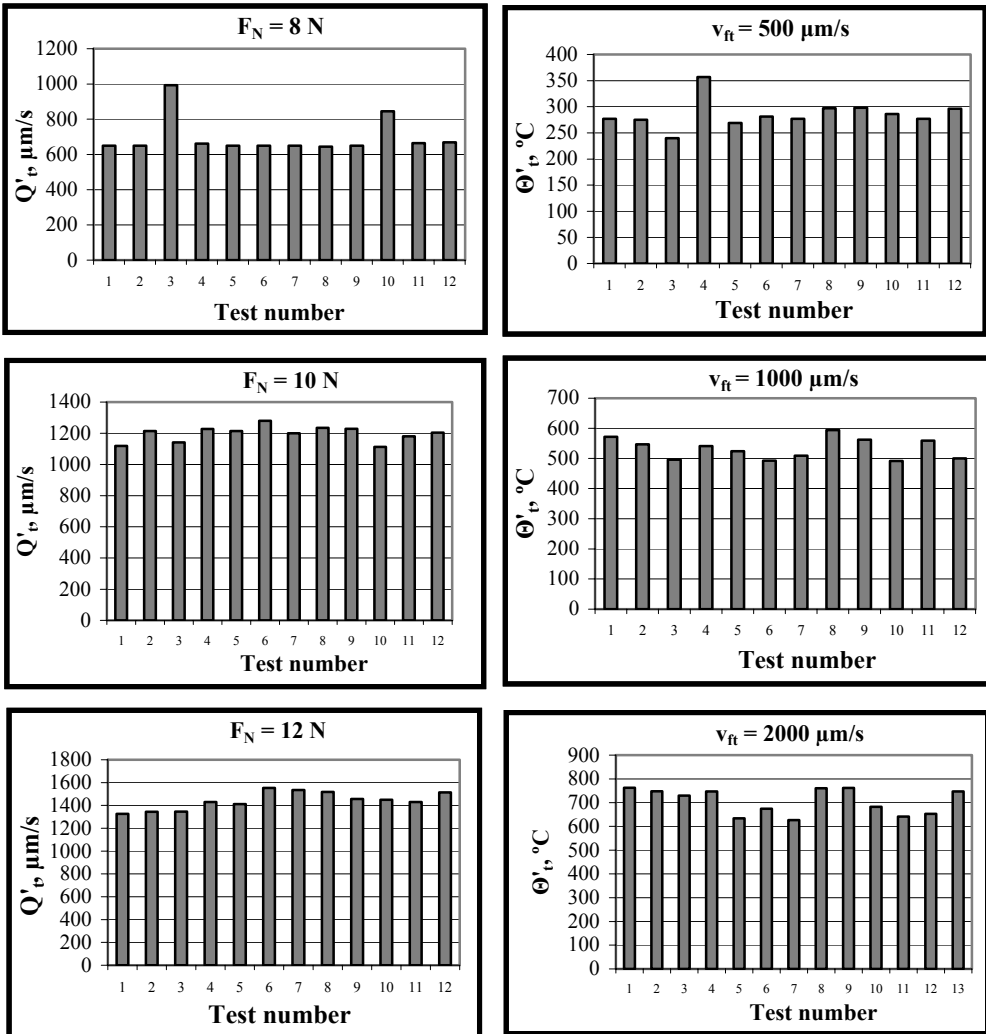
Fig. 4. The results of measurements of cutting ability factors in different conditions of tester grinding: a) factor Q'_t, b) factor Θ'_t

The analysis of the results (Figures 4 and 5) indicates that grinding conditions of the tester have essential influence on the values of Q'_t and Θ'_t and their dissipation. High values of standard deviations of the factors Q'_t and Θ'_t obtained at small forces and speeds of the movement of the tester towards the wheel indicate instability of

grinding of the tester process. A non-uniform increase in the values of Q'_t and Θ'_t obtained at high forces and speeds of the movement of the tester towards the wheel indicates that potential cutting ability of grinding wheel has been exceeded or that perturbation of grinding of the tester process caused by its vibration has occurred. In these conditions of measurement, the increase in standard deviation of Q'_t and Θ'_t has been observed.
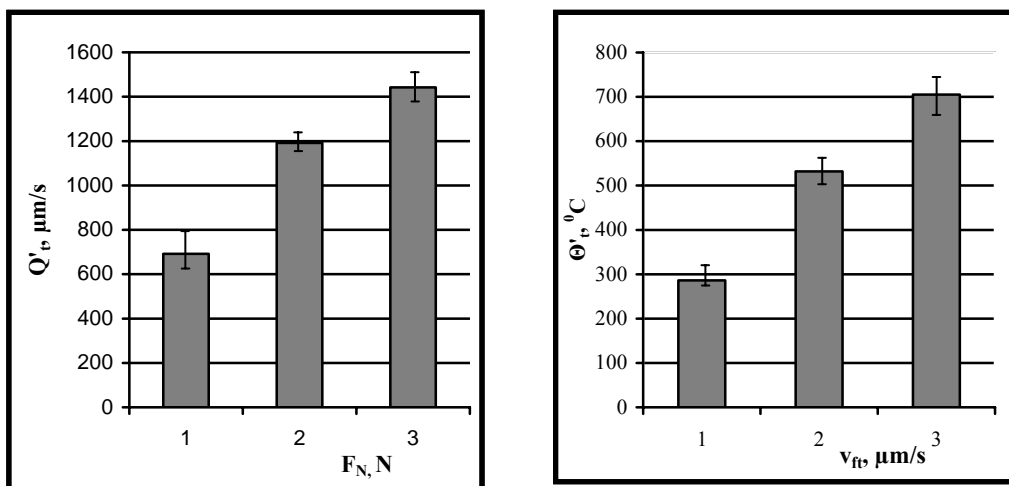
Fig. 5. Influence of grinding conditions of the tester on the factors Q'_t and Θ'_t

The analysis of the investigation results made it possible to choose proper conditions of grinding of the tester, i.e.:
- the movement force of the tester towards the wheel $F_N = 10$ N,
- the movement speed of the tester towards the wheel $v_{ft} = 1000$ μm/s.

In these conditions of grinding of the tester, the accuracy of measurement of the factors Q'_t and Θ'_t is equal to 4.5–7.5%.

3.2. Assessment of cutting ability of grinding wheel after dressing

The aim of the experiments was to verify the usefulness of the method and equipment proposed for the evaluation of CBN wheel cutting ability in varying dressing conditions. The range of investigations included verification of the sensitiveness of cutting ability parameters (Q'_t, Θ'_t) of CBN wheel (1A1-1 350×127×5 LKV50 125/100 ST1 K27 C100) after dressing process with PCD dresser. The dressing conditions of grinding wheel were differentiated by the change of the overlap ratio k_d (defined as the quotient of diamond's width b_d and dressing feed f_d). Dressing process and measurement of cutting ability parameters were carried out on SPG 30×80 surface grinder equipped with dressing control system and measuring device, which enabled meas-

urement of the parameters Q'_t, Θ'_t. Dressing conditions and conditions of cutting ability measurement are shown in Table 2.

Table 2. Dressing conditions and results of measurement of parameters Q'_t, Θ'_t

Dressing conditions		
1	Diamond width b_d [mm]	0.35
2	Overlap ratio $k_d = b_d/f_d$	1, 1.5, 2
3	Dressing in-feed a_d [mm]	0.02
4	Number of dressing passes i_d	4
5	Number of spark out i_w	2
Conditions of Q'_t and Θ'_t measurement		
1	Force F_N exerted on tester during Q'_t measurement [N]	10
2	Tester's speed v_{ft} during Θ'_t measurement [µm/s]	1000
3	Grinding time Δt [s]	1
4	Number of measurements for each overlap ratio	10

Results of measurement of parameters Q'_t, Θ'_t					
Overlap ratio $k_d = b_d / f_d$	Cutting ability factor Q'_t [µm/s]			Grinding temperature Θ'_t [°C]		
	Average value Q'_t [µm/s]	Standard deviation S [µm/s]	Relative error [%]	Average value Θ'_t [°C]	Standard deviation S [°C]	Relative error [%]
1	1158	57.7	4.8	527	23.9	4.5
1.5	725	40.7	5.6	591	36,6	6,1
2	635	43	6.7	631	36	5.7
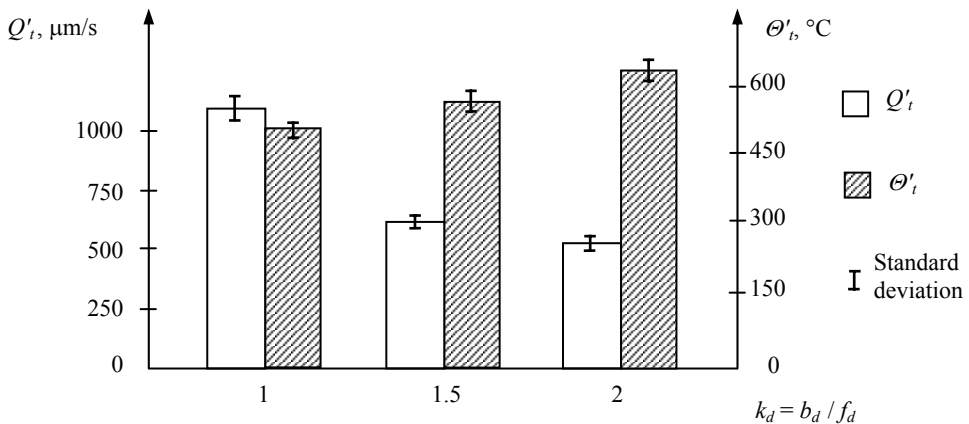
Fig. 6. Relationship between overlap ratio and cutting ability factors

Results of measurements of cutting ability factors (Q'_t and Θ'_t) are shown in Table 2 and in Figure 6. Analysis of the results confirms high sensitivity of the above factors to wheel cutting ability in different dressing conditions. The relationship between the factor values and varying dressing conditions (different overlap ratios) is clear. The

increase in the overlap ratio causes "smoothing" of GWCS micro- and macrogeometry which leads to poorer cutting ability. The cutting ability factor Q'_t decreased by about 55%, while the grinding temperature Θ'_t increased by about 20% with the increase of k_d from 2 to 1.

The measurement confirmed the sensitivity of factors Q'_t and Θ'_t in the case of three different overlap ratios. Significant differences in average values of the factors are greater than standard deviations, which can be seen in Figure 6. Accuracy of the measurement is also satisfactory. Relative error for individual dressing test did not exceed 6.7%.

4. Conclusion

The results obtained, enabled verification of metrological characteristic of new equipment for evaluation of cutting ability of superhard grinding wheels in industrial conditions. Reliable measurements of cutting ability parameters determine the conditions of grinding of the tester (force and speed of tester pressed towards the wheel), time constant of measuring equipment and time of grinding of the tester. The results of investigations confirmed a satisfactory accuracy of measurement of the parameters Q'_t and Θ'_t (relative error of 4.5–7.5%) and their sensitivity to variation of dressing conditions of grinding wheel. The favourable results encourage further tests on the usefulness of the method in superhard wheels with different technical characteristics.

References

[1] Bailey M. W., Juchem H. O.: T*he Advantages of CBN Grinding: Low Cutting Forces and Improved Worpiece Integrity*, IDR, Vol. 58 (1998) 3, pp. 83–89.
[2] Brockhoff T.: *Grind – Hardening: A Comprehensive View*, Annals of the CIRP, Vol. 48 (1999) 1, pp. 255–260.
[3] Inasaki I., Tōnschoff K., Howers T. D.: *Abrasive Machining in the Future*, Annals of the CIRP, Vol. 42 (1993) 2, pp. 723–731.
[4] Oczoś K.: *Kształtowanie ceramicznych materiałów technicznych*, monografia. Politechnika Rzeszowska, 1996.
[5] Borkowski J.: *Zużycie i trwałość ściernic*, PWN, Warszawa, 1990.
[6] Guo C., Wu Y., Varghese V., Malkin S.: *Temperatures and Energy Partition for Grinding with Vitrifield CBN Wheels*, Annals of the CIRP, Vol. 48 (1999), 1, pp. 247–250.
[7] Kato T., Fujii H.: Temp*erature Measurement of Workpieces in Conventional Surface Grinding*, ASME Journal of Manufacturing Science and Enginering, Vol. 122 (2000), pp. 297–303.
[8] Kato T., Fujii H.: *PVD Film Method for Measuring the Temperature Distribution in Cutting Tools*, ASME Journal of Manufacturing Science and Engineering, Vol. 118 (2000), pp. 51–58.
[9] Karpuschewski B., Wehmeier M., Inasaki I.: *Grinding Monitoring System Based on Power and Acoustic Emission Sensors*, Annals of the CIRP, Vol. 49 (2000), 1, pp. 235–240.

[10] Leżański P., Rafałowicz J.: *An Intelligent System for Cylindrical Grinding*, Annals of the CIRP, Vol. 42 (1993), 1, pp. 393–396.

[11] Gołąbczak A., Koziarski A., Rutkiewicz T.: *Ocena czynnej powierzchni ściernicy w warunkach przemysłowych*, Zbiór prac XXIII Naukowej Szkoły Obróbki Ściernej, Rzeszów, 2000, s. 249–256.

[12] Gołąbczak A., Koziarski T.: *Analysis of Functional Properties of CBN Grinding Wheels*, Mechanics and Mechanical Engineering, Vol. 4 (2000), 1, pp. 117–120.

[13] Gołąbczak A., Koziarski T.: *A Method of CBN Grinding Wheel Cutting Ability Evaluation and Measuring Equipment*, II International Conference on APE'2001, Warsaw, 2001, pp. 411–418.

[14] Gołąbczak A., Koziarski T.: *Badania zdolności skrawnych ściernic z regularnego azotku boru*, XXIV Naukowa Szkoła Obróbki Ściernej, Kraków, 2001, s. 349–356.

[15] Koziarski A.: *Czynna powierzchnia ściernicy*, monografia, Politechnika Łódzka, 1996.

**Charakterystyka metrologiczna i wyniki badań urządzenia pomiarowego
do oceny zdolności skrawnych ściernic supertwardych**

Racjonalne i ekonomiczne wykorzystanie atrakcyjnych właściwości użytkowych ściernic supertwardych wymaga oceny i nadzorowania ich zdolności skrawnych w procesie szlifowania. W pracy przedstawiono badania metrologicznych właściwości nowego urządzenia pomiarowego do oceny zdolności skrawnych tych ściernic w warunkach przemysłowych. Zdolności skrawne ściernic są oceniane na podstawie testu szlifowania testera (termopary) i rejestracji za pomocą urządzenia pomiarowego dwóch wskaźników, którymi są: ubytek liniowy testera Q'_t i temperatura szlifowania testera Θ'_t. Przeprowadzone badania umożliwiły uściślenie warunków pomiaru wskaźników skrawności Q'_t i Θ'_t, sprawdzenie powtarzalności pomiaru tych wskaźników oraz ich wrażliwości na zmianę warunków obciągania ściernicy. Wiarygodny pomiar wskaźników determinują warunki szlifowania testera (siła i prędkość dosuwu testera do ściernicy), stała czasowa urządzenia pomiarowego i czas szlifowania testera. Wyniki badań potwierdziły zadowalającą wrażliwość wskaźników Q'_t i Θ'_t na zmianę warunków obciągania ściernicy oraz dokładność ich pomiaru. Względny błąd pomiaru tych wskaźników wynosi około 4,5–7,5%.

Topographic model of active surface of grinding wheel with mixed grains and microbubbles

W. MOROZOW, E. LIANCE
Ukrainian Academy of Polygraphs, Lvov, Ukraine

T. KARPIŃSKI, J. KRZOS
Technical University of Koszalin, Poland

The paper presents the topographic model and geometrical parameters of the active surface of grinding wheels made of the mixture of two types of abrasive grains and a microsphere. A special filler, called a microsphere by the authors, is a novelty in the structure of such abrasive tools. The aim of this paper was to obtain the basic parameters of microgeometry of such grinding wheels by means of analytical approach. A model of such tools has been developed based on the theory of random processes. The experimental results were in agreement with the methods assumed. The geometrical parameters of the active surface resulting from the calculations are very similar to the results of measurements of real abrasive wheels.

Keywords: *topography, model of grinding wheel, mixed grains*

1. Introduction

One of directions of intensifying grinding process is an improvement in construction of an active surface of a grinding wheel (ASGW). This can be done, among others, by making use of new abrasives and new binders. Grinding wheels made of sub-microcrystalline-sintered corundum, which is sold under a trade name of SG (Seeded Gel) or Cubitron, are more and more often used nowadays. Grains of these abrasive materials include microcrystallines vitrified aluminium oxide. They are characterized by exceptional attrition because during the process of grinding fine particles fall out of the grain forming new, sharp points and cutting edges. Another valuable property of SG grains is that they comprise mostly grains with small point corner radii [3]. SG grains are more expensive than traditional grains, therefore it has been decided that they should be mixed with Al-oxide to make one abrasive compound.

Tools made of two-component mixture have different characteristics of wear of respective materials [2]. Fine Al-oxide, the so-called precious, wears by breaking off parts of the grain, so that the whole grain wears at 3–4 stages. Different types of wearing for SG grains and Al-oxide grains result in a complex character of micromachining, both with sharp and dull grains, and paradoxically contributes to an increased cutting output and surface quality.

In order to improve the properties of cutting ability of such a grinding wheel, it has been decided to increase the porosity of the tool by the addition of a special expanding

agent to the abrasive. This filler is in the shape of glass microbubbles with the diameter of 80–250 μm and the walls thickness of 1–2 μm. The microbubbles are getting crushed during the contact with the work material and the pores – cavities are formed on ASGW which can be filled with a grinding fluid, microchips and abrasive waste. This is conducive to carrying the heat away from the grinding area, causes a "cold" grinding, and increases the grinding stock removal [5]. Taking account of the above reasons it has been decided to develop a theoretical model of the tool of two-component abrasive and microbubbles and to compare it with a real grinding wheel.

2. Model of two-component grinding wheel

Basic guidelines to the model are as follows:

• the abrasive mixture consists of the following components: aluminium oxide grains, SG grains, binder, filler (microbubbles);

• grains of each component are considered to be elements of the abrasive mixture and are divided into fractions, depending on their dimensions; each fraction in a given period has its dimensional constraints;

• the proportion of each component in the abrasive mixture is exactly specified in a percentage;

• amount of a binder in the composition expressed in a percentage is exactly determined and depends on the required hardness of the grinding wheel.

Preparation of the specified abrasive mixture satisfying the conditions fixed for the model consists in carrying out the task of stochastic programming in which a relative set of grains in the abrasive mixture assumes a specified position [1] on the active surface and inside the grinding wheel. The output data results from statistical characteristic of components, which comprise the abrasive mixture. The surface of the grinding wheel is formed from a series of abrasive grains, microbubbles and binder. As a result of mathematic modelling the geometric parameters of abrasive grains, microbubbles and ASGW profile are calculated. Modelling of ASGW is carried out in three stages. Stage I comprises a set of mixture components. In the Table, a sample list is given where abrasive grains, 80 in size, were used [6].

Assuming that in given intervals the sizes of grains are random in character and subordinated to the law of uniform distribution with a probability density function (p.d.f.), stage II of this task is solved:

$$y = (x \mid a,b) = (1/b - a)I_{(a,b)}(x) \tag{1}$$

with an average value equal to $(a + b)/2$ and a variance $(b - a)^2/12$, where x – independent variable, b and a – upper an lower limits of grain dimensions. Elements of the abrasive mixture on ASGW are distributed in a random order – this probability depends on a given set of the abrasive mixture.

Table. Components of the abrasive mixture

Components of the abrasive mixture	Number and name of the abrasive-mixture fractions										part of component in abrasive mixture in %	abrasive and microsphere in total volume of abrasive mixture in %
	1 Limited		2 Coarse		3 Nominal		4 Fine		Total			
% fraction of components according to grain sizes	maximum	minimum	maximum	minimum	maximum	minimum	maximum	minimum	maximum	minimum		
Fraction of Al-oxide	4	1	60	50	50	20	2	0	100	95	35	
Size [μm]	314	251	249	201	199	161	124	1				
SG fraction	2	1	70	40	40	20	2	0	100	0	35	
Size [μm]	314	251	249	201	199	161	124	1				
Microsphere	3	1	30	3	80	20	2	0	100	0	20	
Size [μm]	500	300	299	250	249	80	79	1				
Fraction of binder	30	1	30	1	30	1	30	0	100	0	10	90
Size [μm]	150	120	119	85	84	66	65	1				

The following symbols are introduced:

$i = 1...N\_f$ – a number of fractions in abrasive mixture,

$j = 1...N\_k$ – a number of components in abrasive mixture,

d_{ij} – the ith part of this fraction in the j–mth component,

p_j – the jth part of component in the abrasive mixture,

mx_{ij} and mn_{ij} – maximum and minimum parts of the i–jth fraction of the jth component,

$s_j = \sum_i \delta_{ij} d_{ij}$, where $\delta_{ij} = 0.1$ – a total number of some fractions in the abrasive mixture,

mxs_j and mns_j – maximum and minimum values, which can assume variables s_j.

After regarding the symbols assumed the following constraints should be satisfied:

• for each components a sum of fraction parts is equal to 1:

$$\forall j \sum_i d_{ij} = 100\%;\qquad(2)$$

• total fraction of all components in the abrasive mixture is equal to 1:

$$\sum_j p_j = 100\%;\qquad(3)$$

• maximum possible value of fractions larger than minimum possible, all fractions lesser than 1 and minimum non-negative:

$0\% \leq mx_{ij} \leq 100\%$,
$0\% \leq mn_{ij} \leq 100\%$,
$mx_{ij} \geq mn_{ij}$,   (4)
$mn_{ij} \leq d_{ij} \leq mx_{ij}$;

  • for complex fractions the conditions are to be satisfied:

$0\% \leq mxs_{j} \leq 100\%$,
$0\% \leq mns_{j} \leq 100\%$,   (5)
$mxs_{j} \geq mns_{j}$,
$mns_{j} \leq s_{j} \leq mxs_{j}$;

It should be taken into consideration that if relations (2)–(5) are satisfied, then the incidental quantities d_{ij} become interdependent. Therefore, in order to obtain the abrasive mixture satisfying relations (2)–(5), according to a random set of elementary events, the relative minimum d_{ij} of the functional has been found:

$$F(D) = \sum k_{ij} \cdot ((mx_{ij} + mn_{ij})/2 - d_{ij})^2 + \sum ks_{j} \cdot ((mxs_{j} + mns_{j})/2 - s_{j})^2, \quad (6)$$

where the coefficients k_{ij} and ks_{j} become the random weighted means in relation to the values mx_{ij}, mn_{ij}, mxs_{j}, mns_{j} forcing by the same token deviations d_{ij} from averages. By solving equation (6) the random values of some fractions of the abrasive mixture components and in this way conditions (2)–(5) in relation to the abrasive-mixture composition will be satisfied. In a further sequence, the value d_{ij} was used to determine the uniform discontinuous (discrete) distribution occurrence of the abrasive-mixture element belonging to a respective fraction [4].

In the next stage, there are generated random numbers, which determine dimensions of components included in the abrasive-mixture composition and determine a sequence of their arrangement on ASGW by making use of random-number ranges from the discrete distribution of random variables obtained in the above stage of this task.

In general, the discontinuous distribution is characterized by the value ω_i of a random parameter (grain form in our case) in a finite set of a space fragment Ω (common grain set) and responding to the probability value $p_i = p(\omega_i)$, $i = 1,2,...$, where $p_i \geq 0$, $\Sigma p_i = 1$.

The probability of a measure of the subset $A \subset \Omega$ is determined by the following equation:

$$P(A) = \sum_{(i:\omega_i \in A)} p_i. \quad (7)$$

Because of the task at random arranged set A is obtained. The next step of this stage is a solution of the geometric problem of abrasive-grain forms included in the

mixture. It has been assumed that a geometric profile is approximated by broken lines using the information on the random character of apex-angle values and grain sizes.

The same procedure is used for programming the model. Introducing the data determined at stage 1, generator of random numbers Microsoft Excel was used. Then the algorithm of nonlinear optimization of Generalized Reduced Gradient (GRG 2) was used for the procedure of square-functional minimization. Next the information on the sequence of abrasive grain, microsphere and binder arrangement in a series, their coordinates and dimensions for further mathematical processing was introduced into the data base using the special macroassembly program written in Visual Basic. Further modelling of ASGW geometry, visualization and analysis of the data were implemented in an interactive environment of program MATLAB. Because of ASGW modeling the picture of abrasive grains, the microspheres and particles of grains arranged in one layer were obtained.

The grain profile obtained by synthesis in the model is approximated with a broken line connecting 10 points (0–9) in the coordinate system connected with the grain. Points 0 and 9 are conventionally hidden in the binder. Points 1–8 assume a random position in the interval limited by the size and the geometry of grain and the quantity of grinding apex angles. An apex angle of sharp alundum grain is contained within 90–135°. Points 4 and 5 in this grain supersede each other (Figure 1b), whereas in a dull grain are divided from a line segment (Figure 1a). The grains of SG have always a sharp apex with an angle of 60–100° [3]. Points 4 and 5 in the profile model for a sharp grain of SG always coincide (Figure 1c). The microbubble is always approximated with a fragment of a ball and a binder with a segment of an ellipsis with negative values on the *y*-axis. The binder for each own element assumes a random shape – which approximates the model to the real conditions.
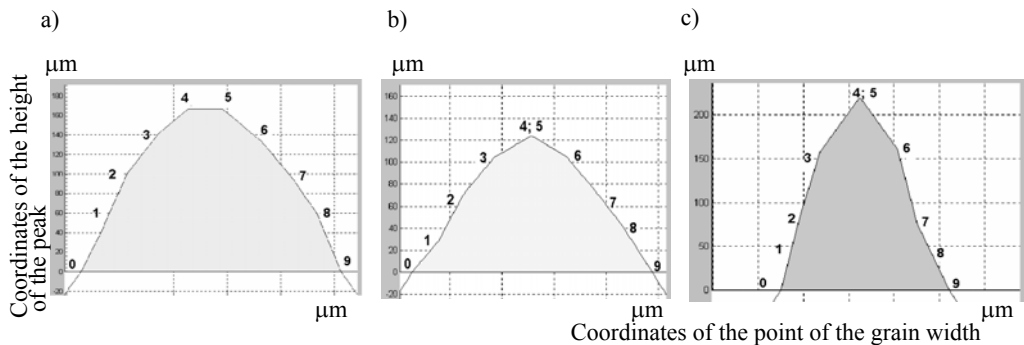
Fig. 1. Fragments of grains profile: a) dull alundum abrasive grain, b) sharp alundum abrasive grain, c) sharp SG abrasive grain

Fragments of ASGW made of multicomponent abrasive mixture are presented in Figure 2. Abrasive grains and other components of mixture in a cutting profile of a grinding wheel assume a random but not a steady position. A cutting profile can be

synthesized depending on the size of grain and binder in the intergrain space towards a vector of grinding wheel speed at its turn about a certain angle.
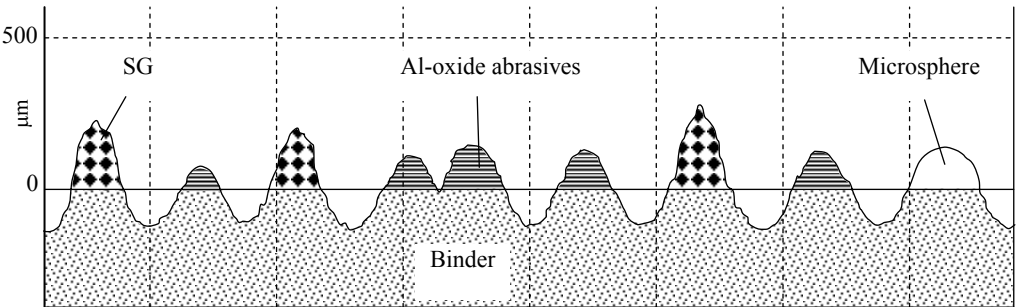
Fig. 2. Fragment of cutting profile of the active face of the grinding wheel made of multicomponent abrasive mixture

The experimental data obtained can be used for solving the virtual problems of output, wear and roughness of work surface while machining using a grinding wheel made of multicomponent abrasive mixture.

Based on computer processing of the model some calculations of microgeometry of ASGW were made taking account of the cutting profiles of abrasive grains. Parameters of grain dimensions and a fractional set were used to introduce the input data according to international standards. The data obtained was averaged and compared with the experimental ones collected with a profilogram of true profiles of grinding wheels.

3. Conclusions

Because of comparison of a ASGW and a real abrasive wheel it was found that the experimental data differs from the calculated ones by not more than 20%. The most accurate calculation results obtained by this method were provided for fine grains of abrasive materials with fillers, whereas greater inaccuracies occurred for coarse abrasive wheels, which is likely to be connected with the law of large numbers. The quality of binder has also an influence on forecasted results of calculations. The binder whose own roughness is not large enables us to obtain more accurate predictions of microgeometry parameters than the binder is with large own roughness. Finally, the model developed enables us to obtain by analysis the fundamental characteristics of the abrasive-wheel microgeometry without making use of expensive scientific equipment. It will be also easier to prepare a tool alone and to forecast approximated geometric parameters of ASGW and its roughness, depending on abrasive grain sizes and their fractional set, which is conditioned by the abrasive-mixture recipe and the way of tool preparation.

References

[1] Gorlenko O. A., Bišutin S.G.: *Model roboczej poverchnosti abrazivnogo instrumenta*, STIN, 1999, Nr 2, s. 25–28.

[2] Karpiński T., Markul J., Krzos J.: *Ściernice hybrydowe*, XXII Naukowa Szkoła Obróbki Ściernej, Gdańsk, 1999.

[3] Karpiński T., Krzos J.: *Mikrogeometria ziaren submikrokrystalicznego korundu spiekanego*, Zbiór Prac XXIV Naukowej Szkoły Obróbki Ściernej, Politechnika Krakowska, Łopuszna 2001.

[4] Koroliov A., Nowosilov Ju. K.: *Teoretiko-verojatnostnyje osnovy abrazivnoj obrabotki*, Izdatelstvo Saratovskogo Universiteta, 1989.

[5] Oczoś K.: *Materiały, narzędzia i obrabiarki do obróbki ściernej na EMO 2001 w Hanowerze*, Mechanik, 2002, Nr 2, s. 70.

[6] Woźniak K.: *Materiały ścierne. Wytwarzanie i własności*, Wydawnictwa Naukowo-Techniczne, Warszawa, 1982.

**Topograficzny model czynnej powierzchni ściernicy
z ziarnami mieszanymi i mikrosferą**

Przedstawiono topograficzny model i geometryczne parametry czynnej powierzchni ściernicy, którą wykonano z mieszaniny dwóch gatunków ziaren ściernych i mikrosfery. Nowością w budowie takich narzędzi ściernych jest specjalny wypełniacz, zwany przez autorów mikrosferą. Głównym celem badań było określenie na drodze analitycznej podstawowych parametrów mikrogeometrii takich właśnie ściernic. Model tego narzędzia opracowano, opierając się na teorii procesów losowych. Wyniki badań potwierdziły słuszność przyjętej metody. Wielkości geometryczne czynnej powierzchni otrzymane w wyniku obliczeń są w dużym stopniu zbliżone do wyników pomiarów rzeczywistych ściernic.

Manufacturing sintered corundum abradants

CZ. NIŻANKOWSKI

Mechanical Equipment Research and Development Centre, ul. Kochanowskiego 30, 33-100 Tarnów, Poland

Classical processes of manufacturing polycrystalline electro-corundum abradants, using the method of charge melting, have gradually been loosing their industrial significance because of two high energy consumtion, inability to manufacture abrasive grains with the pre-defined stereometry patterns, as well as the inability of the abrasive grains thus manufactured to undergo self-sharpening during grinding. The paper presents in detail manufacturing processes of modern micro- and submicrocrystalline sintered corundum abradants that are free of those defects.

The possibilities of modifying sintered alumina abradants by disintegration of the intermediate product, chemical composition enrichment as well as changing sintering period and temperature have been discussed.

There has been described the algorithm of coating the microcrystalline sintered alumina grains with copper. Two alternative methods of producing Al_2O_3 sol in submicrocrystalline sintered alumina production process have been presented. The possibility of ionic implantation of the abrasive grains as well as production of abrasive composites and compact grains from micro- and submicrocrystalline sintered alumina has been mentioned.

Keywords: *abradant, sintered corundum, manufacturing*

1. Introduction

Corundum is the most widely spread and durable crystalline form of α-Al_2O_3. As early as 5000 years B.C. it was highly valued in China as a mineral from which one could extract rubies, natural precious stones with their specific, raspberry-like colour.

About 800 years B.C., rich deposits of fine-grain corundum were discovered on the island of Naxos, in the Greek archipelago of Anatolia. That corundum was later called the Naxos stone. Because that natural alumina contained magnetite, hematite and quartz impurities, it was soon appreciated as a loose abrasive material for making tools, weapons and jewellery. Three hundred years later, in the vicinity of Smyrna, rocks of fine-grain corundum were discovered along with the beds of garnets. That corundum was then called emery. Emery was widely used as an abrasive material until the end of the 19th century. In 1890–1901, due to the research works by Hasslacher, Verlein, Hall and Higgins, the technology of manufacturing artificial corundum was developed. The product was called electro-corundum, after the name of electric arc furnaces in which it was melted. That technology has been preserved almost unchanged until the present day and is still used in many countries to manufacture various forms of electro-corundum abrasive materials.

However, the industrial applicability of that technology tends to be decreasing owing to the high energy-consumption of the processes, lack of a possibility of manufacturing abrasive grains with the pre-defined stereometric patterns and the inability of the grains thus manufactured to self-sharpen during grinding. The basic material used to manufacture electro-corundum abradants is the high-aluminium bauxite. In the process of obtaining standard or semi-precious electro-corundum, bauxite is crushed, baked and then melted (ca. 2350 K) with the addition of coke and iron fillings. When manufacturing semi-precious electro-corundum, larger quantities of reduction agents are added in order to reduce the volume of impurities. Typical electric arc furnaces can operate based in either periodical or continuous melting process. After cooling down and crystallising, the clinker is subjected to crushing, coarse grinding and milling. Next, it is cleaned magnetically and subjected to machine, thermal and chemical treatments. The resulting abrasive material is sieved, washed and separeted into particular grain fractions.

In the process of manufacturing alundum (with the Al_2O_3 contents exceeding 99%), we do not apply baked bauxite as the furnace charge but, instead, we use aluminium oxide obtained either by alkaline methods (e.g. Bayer's base method), or by acid methods (e.g. Michałowski's acid method). The choice of the method to obtain aluminium oxide depends on the so-called bauxite silicate modulus. In order to modify the properties of electro-corundum, which has a polycrystalline structure of abrasive grains, one melts the technological aluminium oxide with zirconium, chromium or titanium oxides to obtain the so-called alloy electro-corundum. In this case, the furnace charge includes only such components that crystallise in the same trigonal arrangement as corundum does. The zirconium electro-corundum may also be obtained through the method of reductive melting of bauxite and zirconium ores.

A separate group of abradants incorporates spherical types of electro-corundum which is also called bubble electro-corundum. It is manufactured by means of blowing the liquid electro-corundum stream with compressed air or steam. Empty electro-corundum balls being created in this process are, after they have cooled down and crystallised, segregated in accordance with their grain sizes. In the abrasive tool industry, the bubble electro-corundum is used not only as an abrasive material, but also as a porosity generation agent.

2. Manufacturing microcrystalline baked corundum abradants

Microcrystalline baked corundum abradants are abrasive materials separated into grains of specific sizes, containing minimum 80% weight of Al_2O_3 obtained as a result of sintering inorganic and non-metallic substances, either natural or synthetic, powdered into 2–5 μm particles. Sintering, in turn, is a process in which the set of fine particles (crystallites, aggregates and agglomerates) is subjected to spontaneous deformation at $(0.4 - 0.85)$ of absolute melting temperature, leading to the concentration of the particle set [1, 2].

For example, when sintering a set of chemically pure Al_2O_3 particles, the ratio of sintering temperature to the absolute melting temperature is 0.822. According to the general sintering theory, the process of concentrating the crushed material (powder), given its specific energy potential, takes place as a result of surface and volume diffusion processes. The more developed are the surfaces and material defects of powder particles, the faster is the course of the sintering process. If particle size exceeds 5–10 μm, the speed of sinter shrinking is small, and the probability of obtaining an abradant with high density is also low. In the sintered abrasive grains numerous, minute, closed pores are formed which are very difficult to remove. Therefore, sintering is an energetic process and its course depends on temperature and time conditions [3].

The methods of manufacturing particular types of sintered microcrystalline corundum abradants show distinct differences in respect of the origin and preparation of raw materials, generation of dispersed arrangements, as well as forming and sintering abrasive grains.

Standard microcrystalline sintered corundum is manufactured of calcined, baked bauxite with low silica content (up to ca. 10% weight) and iron oxide (up to 15% weight). The semi-precious, microcrystalline sintered corundum is manufactured either of the highest-quality bauxite, or of the mixture of baked bauxite and the so-called alumina (technical aluminium oxide) with the alumina contents not exceeding 60% of mixture weight. Precious microcrystalline sintered corundum is manufactured of alumina enriched with oxides (maximum 10% weight) which reduce the sintering temperature (e.g. SiO_2, TiO_2, Fe_2O_3, or CaO). This type of abradant, made of sintered corundum, is produced very seldom.

The properties of abradants made of microcrystalline sintered corundum can be modified through the addition of specially selected oxides, in the same way as in manufacturing alloy electro-corundum. For example, the addition of Cr_2O_3 in the amount of 2.5% weight (purple sintered corundum) or in the amount of 4.5% weight (pink sintered corundum) increases the abradant's cutting ability. The addition of ZrO_2 increases considerably the ductility and thermal resistance of microcrystalline sintered corundum grains, while the addition of TiO_2 stimulates the sintering process and increases the grains' resistance to cracking [4].

The weight of base raw material in forming the abrasive grains must be enriched with proper plasticising and deflocculating agents in order to ensure the grains' resistance in their raw state, accelerate milling and reduce the volume of water. Highly disintegrated bentonite clay is used most often as a plasticiser and a "technological glue". Also dextrin, post-sulphite lyes, polyvinyl alcohol or phosphoric acid (maximum 10% weight) can be used, while the so-called deffloculant or a surfactant is most often ferric ammonium citrate, together with citric acid [5].

After thorough mixing of milled and sieved base and auxiliary raw materials, filtering the obtained mass and removing air from it, the mass is subjected to extrusion moulding and forming to produce the required shapes of abrasive grains. In the process of grain forming, one uses hydraulic presses and screw extruders. The semi-fin-

ished extruded products form one metre long pieces of "spaghetti", each piece with circular, trapezoid, rectangular, square, triangle, rhombic, rhomboidal or ring cross-sections. Hence, the microcrystalline sintered corundum is called, in jargon, the "spaghetti corundum". Upon leaving the screen forming nozzles, the pieces are cut off by special knives and split into abrasive grain formations of the proper length (mostly three or six times the largest cross dimension of the grain section). The highest extrusion capacity (700 to 900 daN/h) can be obtained using hydraulic presses. The extrusion pressure is obviously a function of several variables (chemical composition of the mass, the press or extruder designs, the designs of nozzles and knives, plasticity and porosity of the mass, etc.), however, when shaping plastic mass formations, it does not usually exceed 9 daN/cm^2. It should also be stressed that, in addition to using plastic masses, there are also techniques in which the abrasive grain formations are made of loose or fluid masses [1].

```
┌─────────────────────┐  ┌───────────────┐  ┌───────────────────┐
│ Basic Raw Materials │  │     Water     │  │  Auxiliary Raw    │
└─────────────────────┘  └───────────────┘  └───────────────────┘
                    ┌────────────────────┐
                    │   "Wet" milling    │
                    └────────────────────┘
                    ┌────────────────────┐
                    │  Vibration sieving │
                    └────────────────────┘
                    ┌────────────────────┐
                    │  Propelled mixing  │
                    └────────────────────┘
        ┌──────────────────────────────────────────┐
        │  Pumping the mixture by membrane pumps    │
        └──────────────────────────────────────────┘
        ┌──────────────────────────────────────────┐
        │  Filtering in presses or filtration drums │
        └──────────────────────────────────────────┘
        ┌──────────────────────────────────────────┐
        │  Removing the air from filter slurry      │
        └──────────────────────────────────────────┘
        ┌──────────────────────────────────────────┐
        │  Transportation of filter slurry          │
        └──────────────────────────────────────────┘
        ┌──────────────────────────────────────────┐
        │  Mass pressing and formation              │
        └──────────────────────────────────────────┘
        ┌──────────────────────────────────────────┐
        │  Cutting the abrasive grain formations    │
        └──────────────────────────────────────────┘
                    ┌────────────────────┐
                    │  Radiation drying  │
                    └────────────────────┘
                    ┌────────────────────┐
                    │  Furnace charging  │
                    └────────────────────┘
                    ┌────────────────────┐
                    │      Sintering     │
                    └────────────────────┘
                    ┌────────────────────┐
                    │ Cooling and sieving│
                    └────────────────────┘
```

Fig. 1. Flow chart of the technological process of the manufacturing the modified zirconium and titanium submicrocrystalline sintered corundum [1, 3, 6, 7]

The selection of time and heating temperature in the particular furnace zones depends, first of all, on chemical composition, porosity and size of abrasive grain formations, as well as on the type of the furnace's reducing atmosphere. Within the maximum temperature zone, the process of abrasive grain sintering may occur in the temperature range of 1660–1990 K, while the periods of keeping the grains in that zone may vary from 850 s to 1700 s. After sintering, the abrasive grains of microcrystalline corundum are subjected to cooling and sieving. From the technological viewpoint, the essential factor is the speed of cooling, especially that concerning the modified varieties of microcrystalline sintered corundum, since the speed determines the formation of vitreous phases (ceramic glass, mullite), and intermediate phases (baddeleyite, tiellite), and, through that, the cutting capacities of abrasive grains. The last operations of the technological process of manufacturing microcrystalline sintered corundum are the following: sieving the abrasive grains in order to remove the grains which became cracked during sintering and separating the abrasive material into particular abradant fractions [1, 3].
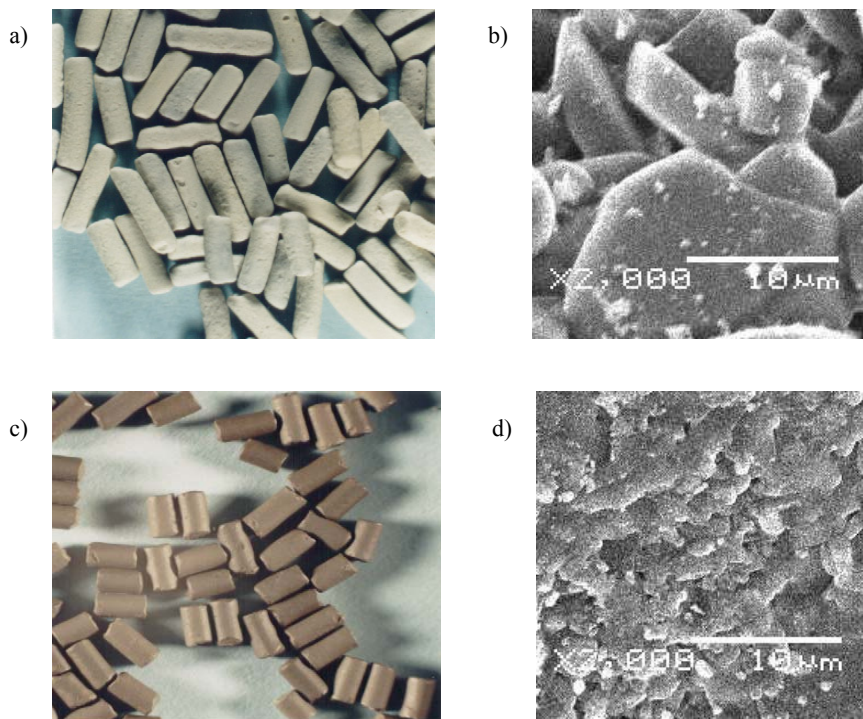

Fig. 2. Abradant of modified zirconium and titanium microcrystalline sintered corundum [1, 8]:
a) view of modified zirconium abrasive grains (×4); b) microstructure of modified zirconium
abrasive grain (×2000); c) view of coating abrasive grams with copper (×4);
d) microstructure of modified titanium abrasive grains (×2000)

Figures 1 and 2 show the technological process of manufacturing the modified zir-conium and titanium microcrystalline sintered corundum, as well as the images of such abrasive grains and their microstructures, respectively. Since microcrystalline sintered corundum abradants are applied mainly in abrasive tools designed for high-capacity machining (e.g. capacity grinding, high-pressure grinding) and during such processes single abrasive grains are subjected to considerable thermal and mechanical shocks, abradants are sometimes coated with thin layers of pure iron, copper, nickel or glass devitrificates [1].

```
┌─────────────────────────────────────────┐
│     Mechanical cleaning of grain surface │
└─────────────────────────────────────────┘
                    ↓
┌─────────────────────────────────────────┐
│        Two-stage degreasing wash         │
└─────────────────────────────────────────┘
                    ↓
                  ( 1 )
                    ↓
┌─────────────────────────────────────────┐
│         Compressed-air drying            │
└─────────────────────────────────────────┘
                    ↓
┌─────────────────────────────────────────┐
│      Loading into ionisation chamber     │
└─────────────────────────────────────────┘
                    ↓
┌─────────────────────────────────────────┐
│  Generating low vacuum (~1.5 Pa within 840 s) │
└─────────────────────────────────────────┘
                    ↓
┌─────────────────────────────────────────┐
│  Generating high vacuum (~$10^{-4}$ Tr within 540 s) │
└─────────────────────────────────────────┘
                    ↓
┌─────────────────────────────────────────┐
│  Cu ion implantation (~1 kV and 125 A within 110 s) │
└─────────────────────────────────────────┘
                    ↓
┌─────────────────────────────────────────┐
│  Cooling down in high vacuum (within 600 s) │
└─────────────────────────────────────────┘
```
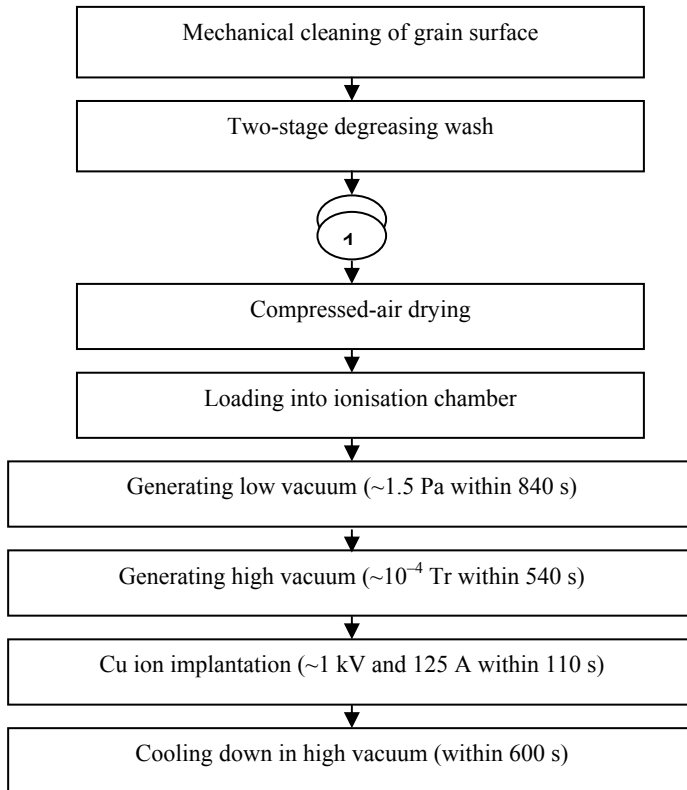
Fig. 3. Block diagram of the technological process of coating the abrasive grains
of microcrystalline sintered corundum with copper [1]

Those layers prevent the mechanically fatigued abrasive grains from accelerated dropping off the tool's binding material, as well as accelerated destruction of binder bridges around the grain occurring through the accumulation of thermal streams from the micromachining zone. The technological process of coating the abrasive grains of microcrystalline sintered corundum with copper, developed by the author of this report and by M. Dąbrowski from the Cracow Polytechnic, is shown in Figure 3.

3. Manufacturing abradants of submicrocrystalline sintered corundum

In the first half of the 1980s, a few initial references have appeared, which were related to submicrocrystalline sintered corundum which was then called Cubitron. The first world's manufacturer of that type of abradant was the American corporation 3M (Minnesota Mining and Manufacturing Co.). Until the end of 1992, Cubitron was placed on the COCOM lists and it was forbidden to export it to the former COME-CON countries. Currently, at least several countries have mastered the technology of manufacturing sub-microcrystalline sintered corundum and they produce it under their own brands. For example, an abradant made of that type of abrasive material by NORTON Company (from Saint-Gobain Abrasives Corporation) was called "Seeded Gel" and the one manufactured by German Norddeutschen Schleifmittelwerke is called "Blue Sapphire" [4, 8, 9].

It soon turned out that the submicrocrystalline sintered corundum, due to its characteristics, is able to displace from the market not only the classical electroco-rundum abradants, but partly even the microcrystalline sintered corundum ones. In many specific industrial applications, the submicrocrystalline sintered corundum be-came a reasonable option even for diamonds and regular boron nitrides [1, 9]. Its abil-ity to self-sharpen in the course of abrasive treatment, susceptibility to abrasive grain shape forming and the significantly lower cost of manufacturing compared to electro-corundum have strengthened the market position of the new abradant. The submicro-crystalline sintered corundum is manufactured with the use of the sol–gel method. First, a synthesis of organometallic aluminium compounds is carried out (e.g. $AlCl_3$ salts), which are then hydrolysed. The directly created colloidal solution, called sol, is composed of Al_2O_3 solid particles dispersed in a liquid medium.

Al_2O_3 sols can also be obtained through dispersing freshly precipitated aluminium hydroxides in a diluted acid. It is also necessary to control the concentration of colloi-dal particles in sol in order to maintain its stability [10, 11]. Figure 4 shows a flow chart of the technological process of manufacturing abradants of submicrocrystalline sintered corundum.

Next, during constant stirring of sol, proper grain growth inhibitors are introduced into it (e.g. MgO or lanthanum) [12]. The sol thus enriched is added, drop by drop, to the solvent which extracts water and stabilising anions causes the formation of the Al_2O_3 gel as a result of coagulation [6, 7]. The Al_2O_3 gels can also be obtained through adding proper gelling agents to the sol (e.g. HNO_3, $Mg(NO_3)_2$) and evaporating the liquid until the moment when the gel begins to form [3]. Another technological opera-tion is gel rolling or constant pressing.

The obtained gel panels (plates) are then dried, under constant monitoring of shrinking and calcined at the temperature of ca. 950 K. After the calcined Al_2O_3 panels have been crushed and powdered, one obtains submicropowders with the grain size ranging from 0.1 μm to 1 μm [11, 12, 15].

```
┌─────────────────────────────┐        ┌─────────────────────────────────┐
│ Aluminium salt synthesis    │   ↔    │ Al hydroxides precipitated in acid│
└──────────────┬──────────────┘        └─────────────────┬───────────────┘
┌──────────────▼──────────────┐        ┌─────────────────▼───────────────┐
│         Hydrolysis          │        │ Al hydroxides dispersed with water│
└──────────────┬──────────────┘        └─────────────────┬───────────────┘
```

Al₂O₃ sol formation

Sol mixing

Introduction of grain growth inhibitors

Addition of gelling agents   Adding the gel drop by drop to solvent

Al₂O₃ gel formation

Gel rolling   Gel pressing

Gel panel forming

Gel panel drying

Gel panel calcination (baking)

Al₂O₃ panel crushing

Al₂O₃ powder forming   Al₂O₃ powdering

Al₂O₃ powder sintering   Al₂O₃ block crushing

Sieving

Abradant segregation

Fig. 4. Flow chart showing the technological process of manufacturing abradants
of submicrocrystalline sintered corundum [9–12]

   The submicropowders of aluminium oxide are then sintered at the temperature
much lower than that applied to microparticles when making microcrystalline sintered
corundum. By changing the submicropowder grain size, the sintering temperature and

time, it is possible to obtain submicrocrystalline sintered corundum with different physical properties and different cutting abilities (e.g. SGB, SGA, SG). It is also possible to control the shape of abrasive grains through the proper formation of submicropowders prior to their sintering (e.g. TG, TGA). Using the sol–gel method and given the proper solution viscosity, it is possible to obtain, through drawing operations, submicrocrystalline fibres of sintered corundum [7]. It seems, however, that this technology has not been fully developed technically and justified economically yet. Instead, fully real and purposeful in some applications is the technology of manufacturing abradants of submicrocrystalline sintered corundum reinforced with SiC n-whiskers (e.g. Cubitron 421) [8, 13, 14]. The abradant of submicrocrystalline sintered corundum from 3M and NORTON 3M is shown in Figure 5.

a)

b)

c)

d)
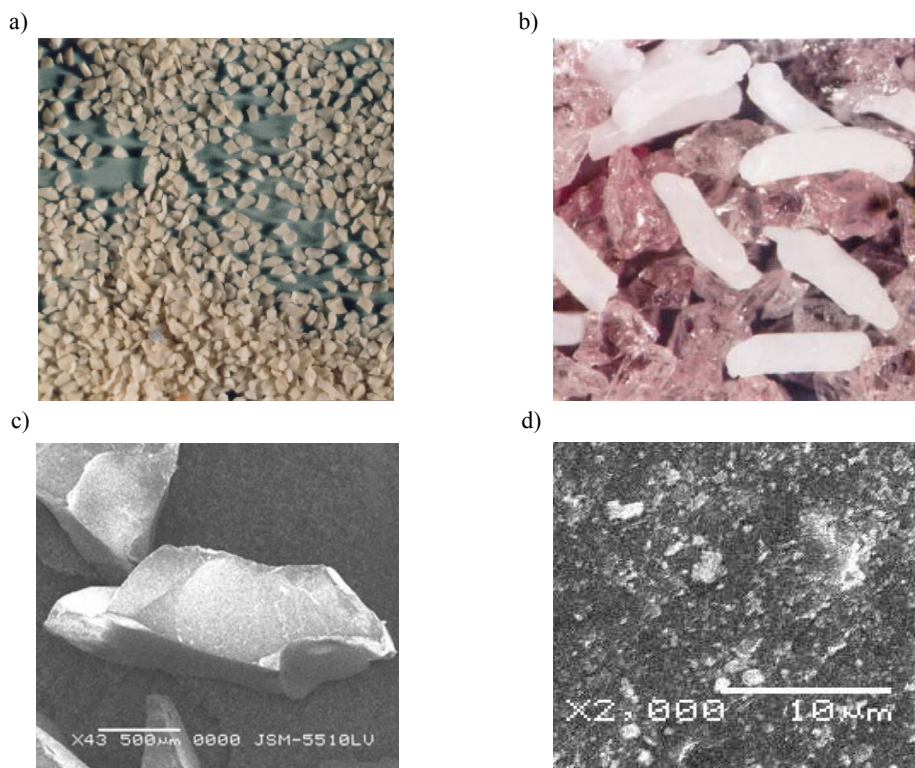
Fig. 5. The abrasive grain of submicrocrystalline sintered corundum:
a) Cubitron from 3M (×2) [8]; b) TGP + CrA from NORTON (×10) [9];
c) single Cubitron 3M abrasive grains No. 46 (×43);
d) microstructure of Cubitron abrasive grains (×2000)

It should be remembered that, owing to the necessity to avoid patent claims of companies competing in manufacturing of such types of abradants, technological

processes and, therefore, also the characteristics of abrasive grain sets in submicro-crystalline sintered corundum display sometimes essential differences. It should also be stressed that abradants of submicrocrystalline sintered corundum are being con-tinuously developed and improved. Examples of this trend may be the technology of submicrolayer ceramic composites, which are manufactured by means of alternately laying the Al_2O_3 gel and Al_3Ti or Al_3Zr gel phases, as well as the technology of modi-fying the properties of submicrocrystalline sintered corundum by high energy (ion energy >20 keV) implantation of the suface layer of abrasive grains with N_2^+ ions to the depth of 300 nm, with the generation of AlNO phase, having crystallites larger (ca. 0.8 μm) than those inside abrasive grains (0.2−0.5 μm). Both innovative technologies enable significant growth of durability, resistance and ductility of abrasive grains made of submicrocrystalline sintered corundum [10, 16, 17]. The abrasive grains from Cubitron 321 with submicrocrystalline sintered corundum platelets are shown in Figure 6. Figure 7 shows a single abrasive compact grain from Cubitron 321, view of the platelet-grain structure and microstructure of single platelet. Experimental tests which were made by W. König, T. Ludewig and D. Staff shows that abradant from Cubitron 321 has three times less attrition than abradant from Cubitron 3M and two times less attrition than abradant from SG [12, 18]. Technology of abradant from Cu-bitron 321 developed by Minnesota Mining and Manufacturing Corporation was not published so far. The same company invented also the way of producing submi-crocrystalline sintered corundum formed like little pyramids with size between 6 and 70 μm. The development lines of corundum abradant technologies presented in this paper prove the constant striving on the side of manufacturers and customers using abrasive tools to obtain abradants with higher and higher cutting abilities, against a simultaneous and constant reduction of manufacturing process costs.
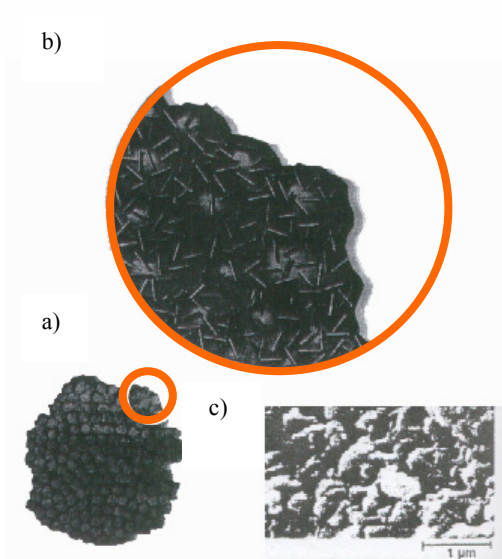

Fig. 6. Abradant from Cubitron 321 (×10)

Fig. 7. Abrasive grain from Cubitron 321 [18]
a) single abrasive compact grain (×100);
b) view of the platelet structure (×1000);
c) microstructure of single platelet

4. Conclusions

Sintered alumina abradants arose as a result of the need to eliminate of energy-consuming and expensive processes of producing classical electroalumina abradants.

Producing micro- and submicrocrystalline alumina abradants by sintering enables not only forming any shapes of abrasive grains, but also the changes of their features. In order to increase cutting abilities of sintered alumina grains, the grains are being sintered into compact grains or abrasive composites.

References

[1] Niżankowski Cz.: *Badania ścierniw z korundu spiekanego*, Sprawozdanie BW/2/94/PK, Politechnika Krakowska, Kraków, 1994.

[2] Pampuch R.: *Materiały ceramiczne*, PWN, Warszawa, 1988.

[3] Пыльнев А.А., Филиппов С.Н.: *Научно-техничэские основы получения спеченных абразивных материалов*, АН СССР, Свердловск 1982, с. 73–83.

[4] Hermes Schleifmittel GmbH & Co., Hamburg, 2001.

[5] Woźniak K.: *Materiały ścierne – wytwarzanie i własności*, WNT, Warszawa, 1982.

[6] Patent US No. 3387957, kl. 51 – 298, 1974.

[7] Patent GB No. 944936, kl. C1A, 1976.

[8] Minesota Mining & Manufacturing Co., Washington, 1999.

[9] Saint–Gobain Abrasives Europe, Paris, 2000.

[10] Niżankowski Cz.: *Submikrokrystaliczny korund spiekany – stan obecny i tendencje rozwojowe*, XXII NSOŚ, Gdańsk, 1999, s. 215–220.

[11] Oczoś K.E.: *Kształtowanie ceramicznych materiałów technicznych*, Ofic. Wyd. Politechniki Rzeszowskiej, Rzeszów, 1996.

[12] König W., Ludewig Th., Stuff D.: *Sol–Gel–Korunde eröffnen neue Leistungspotentiale*, WT – Produktion und Management, Vol. 85, No. 1–2, Springer Verlag, 1995.

[13] Heuer W.: *SG – Wirtschafliche Alternative*, Industrie – Anzeiger, No. 69, 1990, 44–46.

[14] Thangaraj A., Weinmann K.: *On the Wear Mechanism and Cutting Perfomance of Silicon Carbid Whisker-Reinforced Alumina*, Journ. of Eng. for Ind., Vol. 114, 1992, pp. 301–308.

[15] Tönshoff H.K., Friemuth T., Glatzel T.: *Anforderungsgerechte Einsatzvorbereitung von mikrokristallinem Al_2O_3 – Shleifkorn IDR*, Vol. 34, No. 1, 2000, 41–56.

[16] Świderska A. et al.: *Powder Metallurgy of the Al/Al_3Ti Composite*, Inżynieria Materiałowa, No. 4, 1998, pp. 1159–1162.

[17] Углов В., Черенда Н., Ходасевич В.: *Модификация оксида алюмина имплантацией йонами азота*, Физика и химия обработки, Но. 2, 1998, с. 37–40.

[18] Ellis N.: *The drive to improve wheel quality*, Machinery and production engineering, No. 16, 2001.

Wytwarzanie ścierniw z korundu spiekanego

Klasyczne procesy wytwarzania polikrystalicznych ścierniw elektrokorundowych metodą topienia wsadu stopniowo tracą znaczenie przemysłowe. Przyczynami tego zjawiska są duża

energochłonność procesów, brak możliwości wytwarzania ziaren ściernych o z góry określonej stereometrii i brak zdolności tak wytworzonych ziaren ściernych do samoostrzenia podczas szlifowania. W artykule szczegółowo omówiono pozbawione tych wad procesy wytwarzania współczesnych mikro- i submikrokrystalicznych spiekanych ścierniw korundowych.

Wskazano możliwości modyfikowania właściwości spiekanych ścierniw korundowych przez rozdrobnienie półproduktów, wzbogacenie składu chemicznego oraz zmiany okresu i temperatury spiekania. Opisano algorytm powlekania miedzią ziaren ściernych mikrokrystalicznego korundu spiekanego. Przedstawiono alternatywne metody wytwarzania zoli Al_2O_3 w procesie produkcji submikrokrystalicznego korundu spiekanego. Zasygnalizowano możliwość jonowego implantowania ziaren ściernych oraz tworzenia kompozytów i kompaktów (agregatów) ściernych z mikro- i submikrokrystalicznego korundu spiekanego.

Fractal model of the cold martensite transformation in steels

M. RYBACZUK, G. ZIĘTEK

Institute of Materials Science and Applied Mechanics, Wrocław University of Technology,
ul. Smoluchowskiego 25, 50-370 Wrocław, Poland

The paper proposes an approach employing fractal geometry to describe growing martensite phase in an austenitic steel. Inside macroscopic volume (specimen), the distribution of martensite is depicted by measure, and the scaling properties of this measure describe the important, long scale changes of materials characteristics. In fact, distribution of martensite relates to two measures. The first one establishes the mass distribution, and the second one corresponds to additional energy concentrated in martensite phase. The initial postulate consists of specific form of free energy. Besides the uniform material part, it contains also terms coming from each exact-dimensional measure contributing to dimension decomposition of the measure depicting martensite. The final macroscopic constitutive equation becomes some integral over "partial" ones. Calculations make use of the essential simplification – stratification into discrete cells. Various models are studied. Experimental tests were carried for austenitic steel under uniaxial stress states.

Keywords: *fractal model, martensite, constitutive equation*

1. Introduction. Dimension decomposition of measures

Under external load (also cyclic one) the centres of martensite phase become to grow up inside austenitic steel. The entire process is very complicated and various approaches were proposed to describe the changes of materials characteristics. Probably, also from practical, engineering point of view the corresponding changes of constitutive equations appear to be most important. Yet, all calculations of strength of materials are based on them. The basic problem discussed in this paper is the correspondence between microscopic (or mesoscopic) picture of materials structure and macroscopic characteristics like constitutive equations. To some extent, the proposed approach may be treated as generalisation of single fractal model proposed in [4]. In both cases, the increasing amount of accumulated energy with spatial distribution depicted by the scalar value measure controls the running process.

Inclusions of martensite have very complicated form and roughly varying spatial distribution. Therefore, it appears quite natural to depict them with the help of a measure (in the mathematical sense). In the standard approach, the volume ratio of martensite plays an essential role, without paying too much attention to the spatial distribution. The proposed approach puts forward energy as the quantity responsible for phase transition. Every centre of martensite requires some energy corresponding to phase

creation energy and to surface energy (separating phases). In effect growing up martensite can be depicted by a measure μ constituting energy distribution. As a rule this measure does not happen to be exact dimensional (in the mathematical sense) and we employ its natural decomposition into measures which are of exact dimensions. Once a measure has fixed (exact dimension) one may make use of scaling arguments to predict effects corresponding to macroscopic range of scales. Let us underline that the involved measure should equal the energy difference between the uniform austenite phase and a newly formed martensite precipitation. Therefore, we neglect processes occurring and running solely in austenite.

The dimension decomposition of measures is a powerful technique described in [2, 3]. Let μ be a given measure. The lower and the upper local dimensions of μ at the point x are defined in the following way:

$$\underline{\dim}_{\text{loc}}\mu(x) = \lim_{r\to 0}\inf \frac{\ln \mu(B(x,r))}{\ln r},$$

$$\overline{\dim}_{\text{loc}}\mu(x) = \lim_{r\to 0}\sup \frac{\ln \mu(B(x,r))}{\ln r},$$

(1)

where $B(x,r)$ denotes a ball with the radius r centred at x. The most important result from geometrical measure theory is a close correspondence between scaling properties of measure and fractal characteristics of supports (i.e., sets at which the measure under examination is concentrated). In turn, support of the energy measure μ is just the collection of martensite centres (i.e., spatial distribution of martensite). Due to two possible definitions of (lower and upper) local dimensions of a measure one may define two different dimension decompositions of measures. Here we follow the book [2] and make use of lower dimensions.
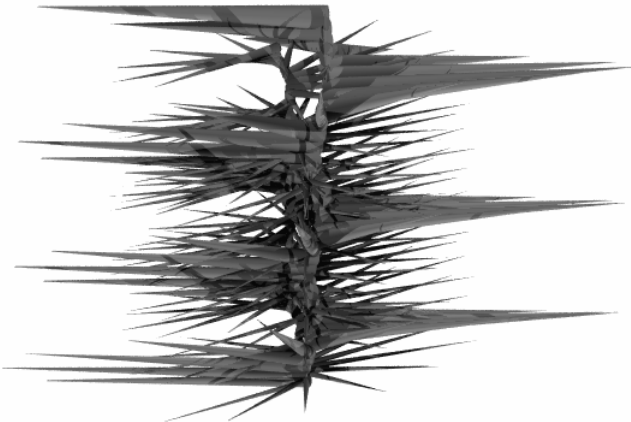

Fig. 1. Generated fractal with needle-like structure depicting possible form of martensite precipitation growing in the bulk volume

For completeness we have to define (see [2] for more details) specific increasing collection of sets $\underline{E}_{\leq s}$ for every positive real number s

$$\underline{E}_{\leq s} = \{x : \underline{\dim}_{\text{loc}} \mu(x) \leq s\} . \tag{2}$$

To some extent the above sets $\underline{E}_{\leq s}$ depict splitting of the support of μ into fragments with fixed or limited scaling properties (in the sense of fractal geometry). The representation theorem from [2] allows us to reduce every (also energy) measure μ to the collection of probability measures (spatial distribution) and to single spectrum density (describing energy per interval of scaling power exponents). Let A be any set. The amount of energy $\mu(A)$ concentrated at A can be expressed as the following integral (see [2]):

$$\mu(A) = \int_0^3 \nu_t(A) d\hat{\mu}(t) , \tag{3}$$

where $d\hat{\mu}(t)$ denotes spectral density and ν_t is the collection of probability measures. The detailed mathematical presentation of (3) as well as the respective theorems are given in [2, 3]. Here we confine ourselves to intuitive arguments solely.
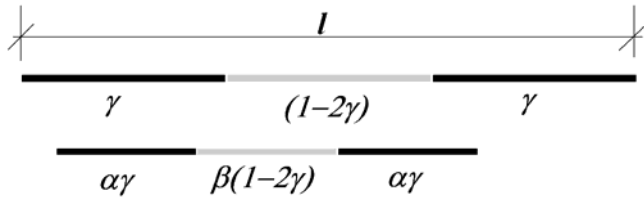

Fig. 2. The intuitive example. First line depicts the initial step of the middle γ-Cantor set made up from various materials. Due to different strength properties, the ratio between length of segments changes in the same way at every stage of recurrence. This entails the suitable shift of fractal dimension

To some extent the essential idea follows from analysis of the intuitive example. Suppose that the spatial distribution of the newly formed martensite has the form of agglomeration of needles presented in Figure 1. Volume of the new phase is relatively small but the surrounding surface separating martensite from austenite can be very large and complicated. Based on theorems from [2] we determine fractal dimensions via planar cross-section of the surface. Suppose now that the exemplary cross-section along some line may have the form of the generalised Cantor set depicted in Figure 2. Therefore, we have a straight segment with the linear size l, which at every stage of recurrence generating the Cantor set is divided into equal parts given by scaling ratio

γ (the so-called middle γ-Cantor set). The initial (box-counting or Hausdorff) fractal dimension equals $D_0 = -\dfrac{\ln 2}{\ln \gamma}$. Applying forces to both ends, thus shrinking or elongating our initial segment, we observe the shift of scaling ratio corresponding to different strength properties of materials (depicted in Figure 2). Simultaneously, the fractal dimension changes itself to $D = (1 + \varepsilon_D)D_0$. Simple calculations give

$$D = -\frac{\ln 2}{\ln \dfrac{\alpha\gamma}{\beta + 2\gamma(\alpha - \beta)}} = -\frac{\ln 2}{\ln \gamma + \ln \dfrac{\alpha}{\beta + 2\gamma(\alpha - \beta)}}. \tag{4}$$

Therefore, for $\alpha \neq \beta$ the corresponding fractal dimension never remains constant under applied deformations. Once the involved deformations being plastic ones are stored in materials we observe the evolution of fractal dimensions. Of course, this is only simple intuitive one-dimensional (contained in a straight line) example, for more realistic, but much more complicated models, calculations become difficult. However, the general idea remains the same.

2. Stratification into cells

The increasing family of sets (2) establishes stratification of various martensite centres into classes with limited fixed scaling properties. In turn probability measures ν_t depict spatial distribution inside each class. Finally, the spectral density $d\hat\mu(t)$ gives amount of energy corresponding to centres from each class. For example, supposing that all martensite inclusions have linear form, one obtains spectral density $d\hat\mu(t) = E\delta(t-1)$, where E is the total energy and $\delta(t-1)$ denotes the Dirac δ-function concentrated at 1 (i.e., at the dimension of a line). The only contributing (in the integral (3)) probability measure is just $\nu_{t=1}$, i.e., $\nu_{t=1}(A)$ is the probability that the centre of martensite enters the given set A. Due to the construction, the energy distribution over a set with fixed scaling properties of the measure must be uniform. The amount of energy (depicted by spectrum) corresponds to the entire probability measure without differentiating various spatial fragments. Very close (single fractal) approximation has been used in [4] to study the growth of defects in fibrous composite.

All notions and variables appearing in previous Equations (1), (2) and (3) are continuous. However, continuous functions can be approximated in terms of step plots and similarly for measures. Such approximation technique coincides with discrete, stepwise picture. We have adopted this method in subsequent calculations. In spite of the fact that (3) gives a decomposition of a measure, the same formula can be used in the opposite approach. Sometimes it is much easier to establish the spatial distribution

(thus the family of probability measures) and the spectrum (this in turn gives spectral density measure like spectral density of energy). Then, (3) is applied to reconstruct the measure from the assumed decomposition.

The entire macroscopic volume A has been divided into small, equal cells. Each cell may contain the inclusion of martensite. Moreover, inside a cell the (possibly existing) martensite phase is assumed to be a (dimensionally uniform) fractal with given fractal dimension. There are many various, nonequivalent fractal dimensions. As a rule in theoretical considerations we refer to the Hausdorff dimension, but in practical calculations the box-counting dimension will be put forward.

The stratification of a macroscopic volume into discrete cells A has also physical justification. The entire specimen corresponds to the macroscopic range of length scales. At the opposite limit, in microscopic range of length we meet separate atoms or molecules with their individual degrees of freedom. However, in every material there exists also an intermediate interval of length scales named the mesoscopic range. It should be so large as to make continual approximation working, but still very small compared with macrolevel. Our cells are just objects modelling this mesoscopic range of length scales.

Once the macroscopic volume has been divided into finite number of cells, the number of various values of dimensions of fractals filling separate cells should also be finite. Therefore we split the interval of possible fractal dimensions (i.e., the interval [0,3]) into finite subintervals. All fractals with dimensions from some interval (let it has an index i) are assumed to have the same fractal dimension D_i. This assumption is exactly the same as stepwise approximation of spectral function. Then the spectral density measure $d\hat{\mu}(t)$ reduces itself to the linear combination of the Dirac δ-functions. Coefficients are just the energies related to inclusions with separate fractal dimensions D_i.

Inside each cell filled with a fractal formed from martensite, the single fractal approximation (described in [4]) should work. The reason is that inside the cells, the centres of martensite are dimensionally uniform. Within the single fractal model energy is proportional to the fractal (Hausdorff) measure according to the generalised energy density from [4].

The amount of the newly formed martensite phase is small. Therefore, the system is expected to be below the critical point corresponding to a suitably large δ-parallel body of fractal (see [2] for more details). No effects related to limited volume are visible. Since all cells have the same linear size, assuming that the fractal of martensite fills entire cell, the energy depends only upon number and distribution of cells with inclusions corresponding to separate values of fractal dimensions. This allows us to perform calculations and to determine macroscopic mean values.

Under external loads, the responses of individual cells depend upon the martensite contained in a cell. For martensite fractals with different structure (fractal dimension)

the responses will be different. In turn, the macroscopic constitutive equation can be derived via averaging over the underlying structure of cells.

The energy involved into a specimen is fixed. Therefore, the total energy of a structure is the only constraint limiting ambiguity of distribution of cells with fractal martensite. We recall that due to the small amount of martensite all terms corresponding to finite volume (see [4]) should be neglected.

The macroscopic volume A should be large enough to make the above procedure working. We expect that for sufficiently large sets A the spatial distribution may vary, but the averaging over underlying mesoscopic structure will give the same results for any set A. Effectively we arrive at statistical assembly of realisations of (large enough) sets A.

Under external loads the martensite phase grows up. At the same time the amount of energy dissipated into newly formed phase increases. Calculating average constitutive equation for each level of energy stored in a macroscopic set A we arrive at constitutive equation, depending upon the energy stored in the newly formed martensite. This final equation includes some parameters to be taken from experiments (or equivalently there are empirical parameters depicting mesoscopic centres of martensite). At the last step of the proposed procedure the mean constitutive equation is verified for real cyclic tests carried out for austenitic steel.

3. Technique of averaging

The macroscopic volume A contains N cells filled with martensite fractals of various fractal dimensions D. Let k_i denote the number of cells with the dimension D_i:

$$N = \sum_{i=1}^{n} k_i \, . \tag{5}$$

Cells without martensite are assumed to correspond to $D=0$. The number of cells with various martensite fractals inside becomes limited by the energy involved into entire system. The fractal measure of each fractal is proportional to the linear size of a cell. Therefore all fractal measures should coincide with various powers of the same linear size. According to the single fractal model from [4], the energy E concentrated at fractal with dimension D and fractal measure v_D equals:

$$E = a(D)v_D \, , \tag{6}$$

where $a(D)$ denotes some generalised energy density and $v_D = l^D$ (for cells with linear size l entirely filled with a fractal). Under external loads the ratios applied in the construction of a fractal inside every deformed cell change. In effect, fractal dimensions of martensite centres vary. Moreover, there are also newly born centres with

small (close to zero) fractal dimension. This depicts the growth up of martensite phase. The generalised energy density $a(D)$ deserves special attention. For various values of D, the values of $a(D)$ become different physical quantities (with different physical dimensions, see [4] for more details). According to the single-fractal approximation from [4] every generalised energy density $a(D)$ distinguishes some length scale, possibly specific to the current value of D. We are not able to determine $a(D)$ from experimental measurements (at present time there is no any experimental technique allowing us to do this). On the other hand, just this specific length scale coming from $a(D)$ should play the role of the mesoscopic length scales. The simplest possible model of $a(D)$ assumes the unique, universal with respect to D, length L_0 (simultaneously constituting mesoscopic range of length scales). Then $a(D) = E_0 / L_0^D$ and according to previous arguments L_0 should coincide with individual cell size (all cells have the same size), in turn E_0 is some fixed portion of energy. Moreover, for the fractal filling entire cell $v_D = L_0^D$. Under this approximation or model, energy of each individual fractal centre equals E_0 independently of the fractal dimension D. Therefore, within this approximation, the fixed amount of involved energy means just the fixed number of cells containing martensite centres. According to our assumption every such configuration may occur with the same probability (the standard problem in the probability theory). In this case, solely the number of possible configurations determines the value of probability of a single event. Once more we underline that the volume of the set A must be large enough (the macroscopic volume) to avoid substantial differences between various choices of A (large fluctuations). This can be even essential in more advanced models with more complicated forms of the function $a(D)$.
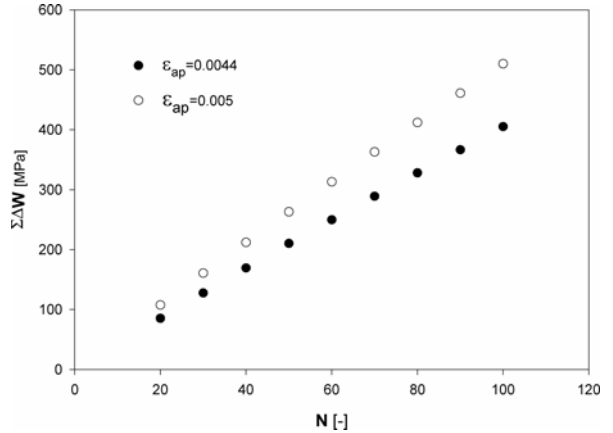
Fig. 3. Experimentally obtained relationships between $\sum_{i=1}^{N} \Delta W$ and the number of cycles N

We assume that the plastic deformation is uniform inside the entire A, and the stress σ changes due to the fractal dimension approaching the value (σ_i). Choosing

m cells from the volume A we obtain the set of possible configurations $\Pi(m_1,...m_n)$ and $m = \sum_{i=1}^{n} m_i$. We calculate the (macroscopic) mean value of the stress Σ:

$$\Sigma = \sum_{\Pi} \left[\sum_{i=1}^{n} \sigma_i m_i \right] P(\Pi) = \sum_{i=1}^{n} \sigma_i \sum_{\Pi} m_i P(\Pi), \tag{7}$$

where $P(\Pi)$ denotes the probability of the appearance of the configuration Π. After simple calculations we obtain:

$$\Sigma = \frac{m}{N} \sum_{i=1}^{n} \sigma_i k_i . \tag{8}$$

This establishes the macroscopic constitutive equation if one knows the corresponding mesoscopic models.

4. Identification

4.1. Experiment

The purpose of the experiment was to record the influence of appearance of a new phase, i.e., martensite, in austenite on cyclic properties of material, in particular, on constitutive equations. The material used was metastable austenitic steel. The tests were carried out using hydraulic pulser (MTS-810) under constant plastic strain amplitude ε_{ap}. Cylindrical specimens were tested under uniaxial tension–compression (R=−1). The measured quantities were: total (ε), elastic (ε_e) and plastic (ε_p) strains, stress (σ) and hysteresis loop area (ΔW).
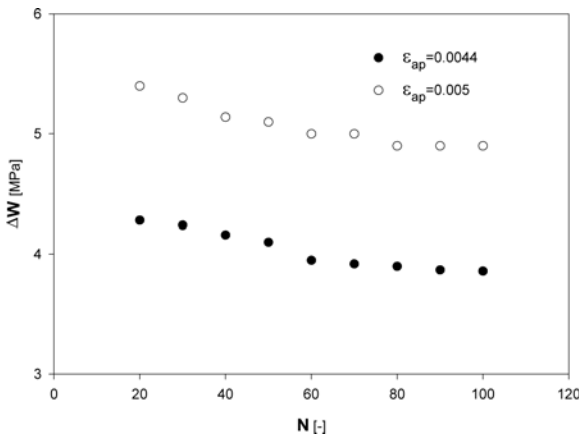

Fig. 4. Experimentally obtained relationship between $\Delta W(N)$ and the number of cycles N

It has been assumed that the growth up of martensite takes place intensively during initial cycles of deformation and we have confined ourselves to the first 100 cycles. Figures 3 and 4 present experimentally obtained plots of $\sum_{i=1}^{N} \Delta W$ and $\Delta W(N)$ for selected plastic strain amplitude.

The SigmaPlot package has been used in identification of parameters in the proposed models.

4.2. Models

Two different materials models were applied, namely, the Ramberg–Osgood model commonly used for cyclic loads and the elastoplastic model with kinematic hardening.

The Ramberg–Osgood model. In this model, the equation linking total stress and strain has the following Osgood form

$$\varepsilon + \varepsilon_a = \frac{\sigma}{E} + \left(\frac{\sigma + \sigma_a}{K} \right)^n , \qquad (9)$$

where ε_a and σ_a are amplitudes of total strain and stress, respectively, and E denotes the Young module.
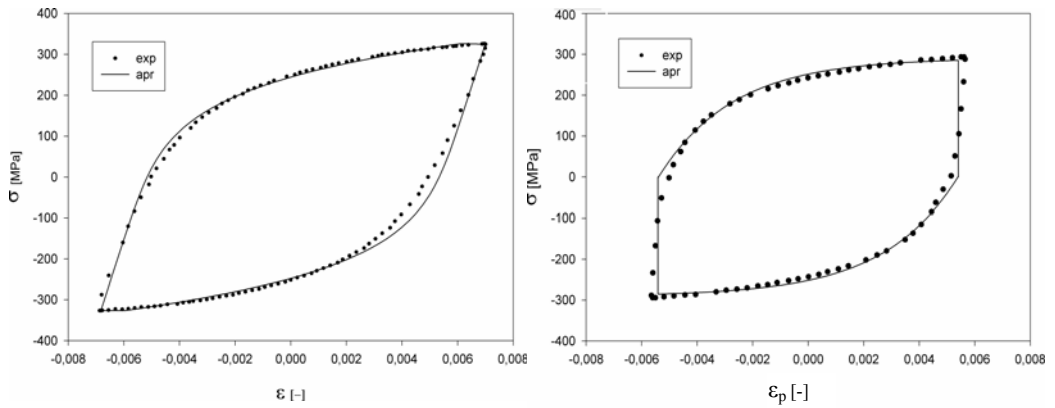

Fig. 5. Identification of the chosen hysteresis loops

Analysis of experimental results suggests that the power exponent n is constant (independent of number of cycles, thus energy independent) and equal to 6.5. Figure 5 depicts the results of identification of the chosen hysteresis loop, Figure 6 presents the dependence of the parameter K upon the energy dissipated in material.
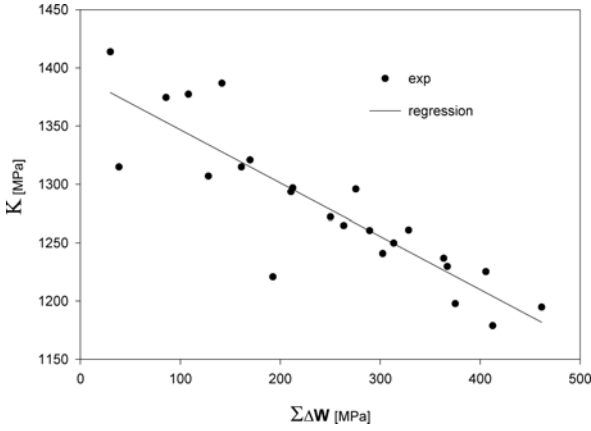
Fig. 6. The (fitted to experimental data) dependence of the parameter K upon the energy dissipated in material $K(W) = -0.46W + 1398$

The elastoplastic model with kinematic hardening. The form of plasticity surface has been assumed as the manifold widely known in literature devoted to elastoplastic media with kinematic hardening, namely:

$$|\sigma - X| - \sigma_o = 0, \tag{10}$$

where σ denotes compression or tension stress, X is the kinematic hardening parameter, and σ_o means the plasticity limit. Plasticity surface shifts itself only without either expansion or compression. Moreover, we assume that the total strain is a sum of elastic and plastic deformations (therefore the transformation strain has not been separated and both processes, i.e., plastic deformation and phase transition, are treated as the coupled ones)

$$\varepsilon_c = \frac{\sigma}{E} + \varepsilon_p. \tag{11}$$
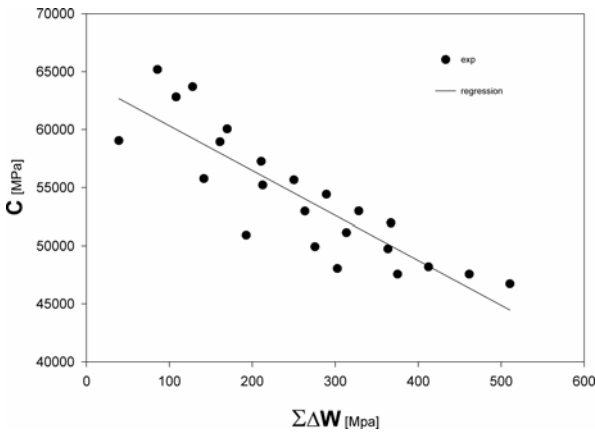
Fig. 7. The (fitted to experimental data) dependence of the parameter C upon the energy dissipated in material $C(W) = -39W + 64193$

The Young modulus E does not change during phase transition (remains the same for both phases).

The evolution equation for kinematic parameter has been accepted in the form of the Frederick–Armstrong equation (see [1]):

$$dX = Cd\varepsilon_p - \gamma d\lambda. \tag{12}$$

The $X(\varepsilon_p)$ can be derived from Equation (12). For increasing branch of hysteresis loop one obtains the following dependence:

$$X(\varepsilon_p) = \frac{C}{\gamma}\left(1 - \frac{\exp(-\gamma(\varepsilon_p + \varepsilon_{ap}))}{\cosh(\gamma\varepsilon_{ap})}\right) + \exp(-\gamma\varepsilon_p)f(N), \tag{13}$$

where ε_{ap} is the plastic strain amplitude, and

$$f(N) = \frac{C}{\gamma}\exp(-4N\gamma\varepsilon_{ap})\left(\frac{2 - \exp(\gamma\varepsilon_{ap}) - \exp(3\gamma\varepsilon_{ap})}{2\cosh(\gamma\varepsilon_{ap})}\right). \tag{14}$$

Since the function $f(N)$ approaches zero very fast, for example, for $\varepsilon_{ap} = 0.005$, and $C/\gamma = 150$ (the value derived for the material under examination after large number of cycles) $f(4) = 3 \cdot 10^{-9}$, the second term in Equation (13) is negligible. Next, Equations (12), (13) entail the relationship between plastic strain and stress:

$$\sigma = \frac{C}{\gamma}\left(1 - \frac{\exp(-\gamma(\varepsilon_p + \varepsilon_{ap}))}{\cosh(\gamma\varepsilon_{ap})}\right) + \sigma_o \tag{15}$$

for $\sigma \geq \sigma_o - \dfrac{C}{\gamma}\tanh(\gamma\varepsilon_{ap})$ as well as for increasing branch of the hysteresis loop.

Therefore it can be assumed that the obtained hysteresis loops are symmetric with respect to compression and tension. That entails the similar formulas for the decreasing branch of hysteresis loop with the same model parameters.

Results of identification show that the parameter γ is constant and C is the only parameter dependent upon the number of cycles (thus dependent upon energy). For the chosen hysteresis loops the results of identification are presented in Figure 7.

5. Discussion

In spite of many efforts and an enormous number of papers, the detailed description of strain-induced martensite transition is still missing. As a rule the parameters depicting the appearance of the newly formed phase are volume or mass ratios. However, such term can include a contribution coming from phase formation solely. In contrast, the observed fragments of martensite have very complicated geometry. An example of such structure is depicted in Figure 1 (fractal model). Besides phase creation energy there is also some amount of energy coming from the surface separating martensite and austenite. For structures like needles from Figure 1 this surface term can dominate.
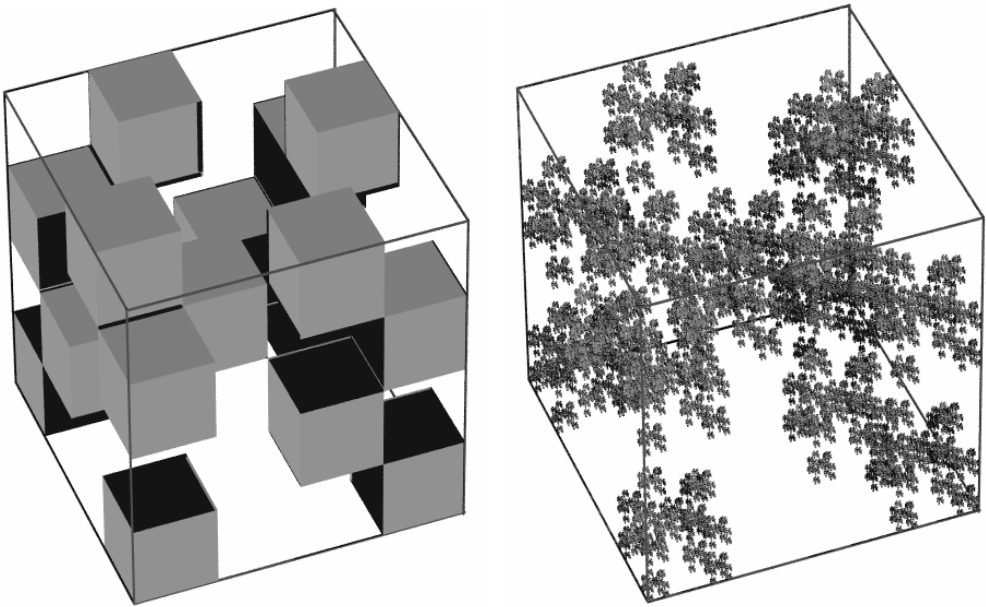

Fig. 8. Exemplary construction, 3-dimensional generalisation of the ordinary Cantor set recurrence. At every stage of recurrence each box will split into smaller sub-boxes according to identical rule. Choosing various ratios and configurations of boxes one may construct a fractal with all values of dimensions between 0 and 3

In contrast to current literature, we propose the fractal model of individual martensite centres. The exemplary construction of such fractals is depicted in Figure 8. Changing ratios and choosing smaller cubes (in selfsimilar way) we may construct fractal with every dimension between 0 and 3. One may think that fractals of this type (3-dimensional generalisation of the ordinary Cantor set recurrence) fill individual cells. Such simplified fractal models are widely applied in papers dealing with fractals (the so-called toy models).

The so-called multifractals are the standard mathematical technique to describe the differentiated (with respect to local dimension) collection of fractals. However, we have found multifractals rather useless in this problem. The dimension decomposition of measures appears much more effective. Since this method has been never used for similar problems the detailed presentation of averaging technique should be also included. According to Equation (6) energy becomes also a measure in rigorous, mathematical sense.

From the very practical point of view, the macroscopic constitutive equation appears to be the most important material characteristics. Accepting some constitutive equation for each individual cell we may calculate mean macroscopic quantities for any given energy stored in martensite centres. Such averaging depends upon probability distributions solely. The entire "fractality" becomes hidden in the way of averaging. Two simple but widely applied model constitutive equations are compared and fitted to experimental data. The relatively small scatter of data appears to support our theoretical ideas. On the other hand, at present time there is no experimental technique allowing direct observation of martensite growing in large bulk volume of austenitic steel. Therefore only improper experimental verification via macroscopic constitutive equations may support our models.

References

[1] Lemaitre J., Chaboche J. L.: *Mecanique des materiaux solides*, Dunod, Paris, 1985.
[2] Falconer K.: *Techniques in fractal geometry*, John Wiley & Sons, Chichester, 1997.
[3] Mattila P.: *Geometry of sets and measures in Euclidean spaces*, Cambridge University Press, 1995.
[4] Rybaczuk M., Stoppel P.: *The fractal growth of fatigue defects in materials*, Int. Journal of Fracture, 2000, Vol. 103, pp. 71–94.

Fraktalny model przemiany martenzytycznej w stalach

Przedstawiono próbę zastosowania geometrii fraktalnej do opisu wzrostu fazy martenzytycznej w stali austenitycznej. Wewnątrz makroskopowej objętości próbki rozkład martenzytu zadaje miara i własności tej miary z uwagi na skalowanie opisują istotne własności materiału w zakresie długich skal. Faktycznie rozkład martenzytu jest związany z dwoma miarami. Pierwsza określa rozkład masy, a druga odpowiada dodatkowej energii skupionej w fazie martenzytycznej. Podstawowy postulat to specyficzna postać energii swobodnej. Oprócz jednorodnego członu związanego z materiałem zawiera ona również człony pochodzące z każdej miary wymiarowego rozkładu miary opisującego rozkład martenzytu. W rezultacie makroskopowe równanie konstytutywne staje się całką po częściowych wkładach. Obliczenia wykorzystują istotne uproszczenie – rozkład na komórki. Zbadano różne modele. Testy eksperymentalne przeprowadzono dla stali austenitycznej w jednoosiowym stanie naprężenia.

Modelling of workpiece surface layer
state after grinding process[*]

M. URBANIAK

Department of Production Engineering, Technical University of Łódź, Stefanowskiego 1–15, 90-537 Łódź

In the paper, a neural model allowing us to forecast chosen surface layer features of the ground workpiece is described. The model was used for analysing the influence of wheel characteristics and dressing conditions on surface roughness of workpiece and residual stresses. The relationships published in literature were also taken into account. An example of the model application was shown as well.

Keywords: *surface roughness, residual stresses, modelling*

1. Introduction

The problem of the influence of grinding wheel cutting surface state on grinding process result is one of main topics of research works carried out in the field of abrasive machining. As the problem is complex, its description by modelling seems to be a good solution. There are two areas the problem: evaluation of workpiece surface layer state and surface roughness [1]. The first one describes the influence of heat and plastic deformation during grinding. In Tönshoff's publication [1], review of 13 modelling solutions describing the influence of mechanical and heat factors on the material being ground were shown. As a result, he observed such changes of microstructure as change of hardness, phase changes and structural changes, which cause also changes of volume. As a result of model action, the forecast of stress level in workpiece surface layer was made. Residual stress may lead to workpiece material damage and deformations. Most of heat models are based on the the Carslaw–Jaeger model of temperature distribution in workpiece with movable heat source. The finite element method is usually applied in evaluation of stress. The models constructed by Mishr, Tönshoff and Choi concern the influence of thermal and mechanical phenomenon. In order to improve modelling accuracy, grinding force, energy and specific grinding power were taken into consideration. Those models can be compared now with Malkin's model, which describes critical specific energy and critical temperature, above which burns occur on the surface being ground. On the basis of research carried out at the beginning of the last decade, specific grinding power was found to be a characteristic feature of the process. It was related to residual stress using thermo-physical

---

functions. It was assumed that application of different grinding methods and different grinding wheels did not influence basic relation.

If heat generated in contact zone is not distributed uniformly (change of speed, different allowance) the above models need to be corrected. In such a situation, experimental models based on finite elements method are frequently applied. Their practical applications seem to be more universal [1]. Rowe [2] determined the quantity of heat being transmitted to workpiece material using foil thermocouple. 50% share was reached for CBN wheel and 80% for alumina wheel. It decreased together with the increase in the dressing in-feed (from 2 to 14 μm) by about 20%. He showed theoretical model, in which thermal factors of grinding wheel and workpiece were introduced.

In Kruszyński's publication [3], a model of temperature distribution in workpiece based on measurement of tangential component of grinding force was described. High compatibility between measurement results and computing results was achieved. The author presented also software, which enabled determination of workpiece surface layer properties on the basis of three-dimensional distribution of temperature in this layer. Those researches lead to elaboration of the factor B_p, which determines the amount of heat transferred to workpiece (product of energy flux density and time of its action) [4]. The factor can be applied during forecasting of residual stress in workpiece surface layer. The method is useful for evaluation of surface layer state.

The second area of problem touches the quality of the surface being ground and is connected with the surface roughness modelling and description of wheel's microstructure [1]. Some models contain a constant value, representing the workpiece material instead of wheel's microstructure factor. Typical model is shown below:

$$R_t = C_{wp} \cdot C_{gw} \cdot \left(\frac{1}{q}\right)^{e_1} \cdot a^{e_2} \cdot \left(\frac{1}{d_{eq}}\right)^{e_3}, \tag{1}$$

where:

R_t – parameter of surface roughness,
C_{wp}, C_{gw} – workpiece material constant and wheel constant value, respectively,
q – quotient of workpiece speed and wheel speed,
a – grinding in-feed,
d_{eq} – equivalent wheel diameter,
e_1, e_2, e_3 – exponents.

Constant values usually contained in models need to be determined experimentally. Those models are based on the idea of grinding process stability and good results are achieved for small values of grinding in-feed. Grinding time causes variation in wheel topography which leads to the variations in surface roughness parameters. In another models, additional constant factors being in accordance with dressing conditions were introduced. Changes of surface roughness during wear process of the wheel are de-

scribed by linear function of ground material volume. Application of these models requires large number of experiments in order to determine constant values. In fact, practical model of surface roughness has not been developed yet.

In other words, precise and easy in use model of workpiece surface layer state has not been found. A large number of parameters and factors which influence grinding process cause unsatisfactory results as only few of them are taken into consideration. Also a considerable number of experiments need to be carried out in order to find desired constant values in the model, for adequate grinding conditions. Although basic research in this matter is essential, practical approach is needed. There is a chance of fast, practical applications of neural models. They enable precise description of the problem without simplifications, besides their labour consumption is similar to that of mathematical models. However, the unknown function of the model, in the form of weight matrix, is the main disadvantage of such models.

2. Workpiece surface layer state modelling

The aim of workpiece surface layer state modelling was to find the relationship between technological input values and particular surface layer features of the work-piece being ground. According to the above-mentioned arguments, a neural model method was applied.

2.1. Data set preparation

Database for the model construction, according to input values, included wheel characteristics and dressing conditions (Table 1).

Output values were: grinding process results described by a parameter of work-piece surface layer state, i.e. maximum residual stress $\sigma_{\max}$, and surface roughness parameter R_a measured after a few grinding passes.

Equation determined empirically [4, 5] was applied. The above-mentioned factor B_p of surface grinding can be calculated from the following relation:

$$B_p = \frac{v_s \cdot F_t}{v_{ft} \cdot b_p} \quad [\text{Ws/mm}^2].$$
(2)

The relationship between maximum residual stress in surface layer and the factor B_p is presented as follows:

$$\sigma_{\max} = 144.45 \cdot B_p + 273.64 \quad [\text{MPa}].$$
(3)

When equation (2) is introduced into regression equation (3) one can arrive at the following relation:

$$\sigma_{\max} = 144.45 \frac{v_s \cdot F_t}{v_{ft} \cdot b_p} + 273.64 \quad [\text{MPa}], \tag{4}$$

where:

    v_s, v_{ft} – speeds of grinding wheel and workpiece, respectively,

    F_t – tangential component of grinding force,

    b_p – grinding width.

Table 1. Conditions of research

Characteristics of wheels made by Saint Gobain Abrasives KORUND	1A1 350×40×127 38A 46/60/80 J/K/L 5 VBE
Dressing conditions	
Type of dresser	M 1010, single-point diamond
Diamonds width b_d [mm]	0.8−1.1
Number of dressing passes	5
Dressing in-feed a_d [mm]	0.005, 0.015, 0.025
Overlap ratio $k_d = b_d/f_d$	1.2−2.5
Grinding kinematics on the SPG 30×80 surface grinder (PONAR-GŁOWNO)	
Grinding speed v_s [m/s]	26.5
Workpiece speed v_{ft} [m/s]	0.16−0.33
In-feed a_e [mm]	0.005−0.025
Number of grinding passes	4
Workpiece material	SW7M (HRc 60−62°)

The relation enables forecasting of stress level in the surface layer on the basis of grinding force component measurement.

In this research, a workpiece state is determined in initial stage of grinding process, where the influence of dressing conditions is obvious.
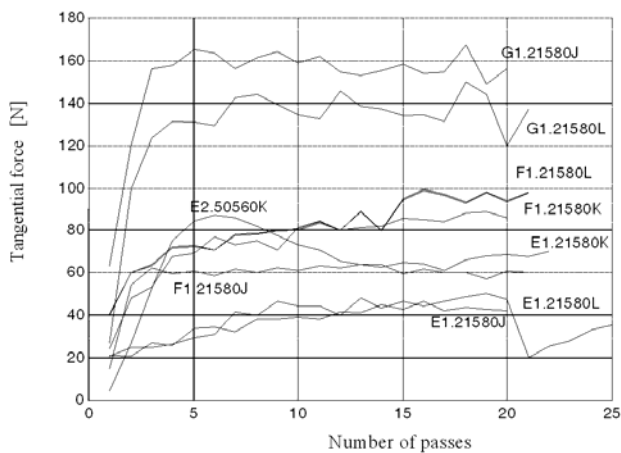

Fig 1. Tangential component of grinding force as a function of number of passes

Minimum number of grinding passes were determined experimentally. Grinding process was carried out until process conditions were stabilised. Measurement of grinding forces was applied as the best factor, which shows behaviour of the machine–tool–fixture–workpiece system. Tangential component of grinding force for different wheels and process conditions is shown in Figure 1.


Granularity of grinding wheel	Grain size (average) [mm]
46	0.390
60	0.275
80	0.196
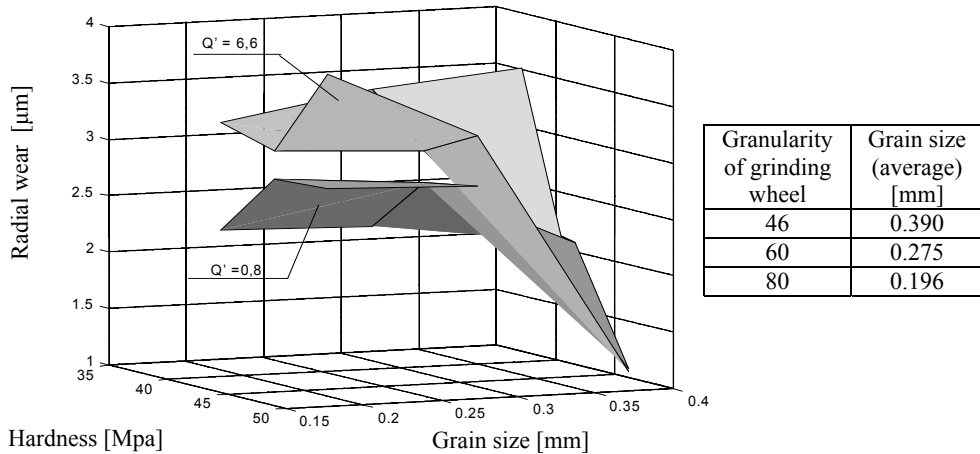
Fig. 2. Radial wear of wheels versus hardness and grain size of grinding wheels (k_d=1.8, a_d=0.01)
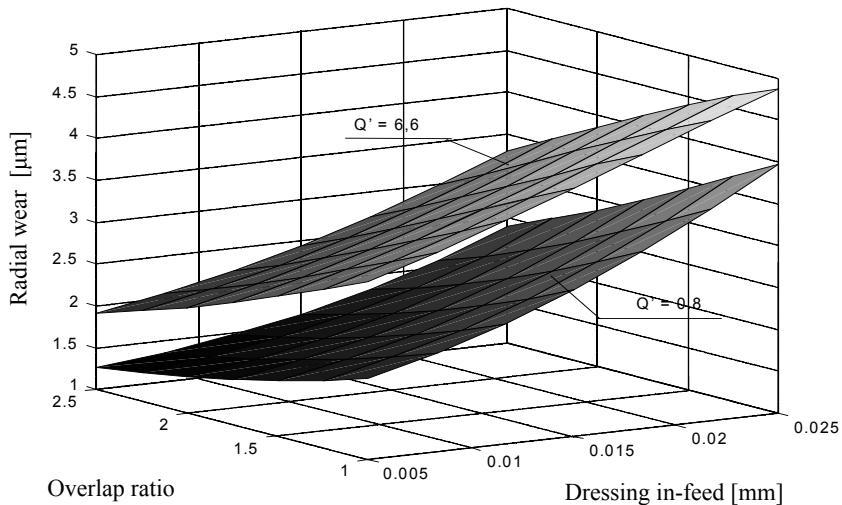
Fig. 3. Radial wear of wheels versus overlap ratio and dressing in-feed (38A60K5VBE wheel)

Specific grinding efficiency is designated by:
– productivity $Q' = 0.8$ mm²/s (E), $Q' = 2.5$ mm²/s (F), $Q' = 6.6$ mm²/s (G),
– overlap ratio $k_d = 1.2, 2.5$,
– dressing infeed $a_d = 5, 15$ μm.

After a few grinding passes (3–5) a fast increase in grinding forces is stopped and stabile performance of the wheel is observed. On the basis of the above observations the analysis of workpiece surface layer state was decided to be carried out after four grinding passes. Radial wear of GWCS, which appears at the same time, is shown in Figures 2 and 3.

The smallest radial wear (about 1.1 μm) was achieved for "46L" wheels, independently of grinding intensity (Figure 2). Signs of wear of other types of grinding wheels were comparable, however greater wear was observed during intensive grinding (over 3.5 μm). The influence of dressing conditions on radial wear was also important (Figure 3).

Stronger influence of dressing in-feed was here observed. Firefold increase of the in-feed value caused increase of wear by about 80%. Over twofold decrease of the overlap ratio k_d caused 200% reduction of wear. The changes in the working area of GWCS took place up to 5 μm depth. This must have been due to the fact that no spark-outs were allowed, as they would interfere with influence of dressing parameters.

Finally experimental database for construction of neural model was created on the basis of measurements of grinding force tangential component and surface roughness parameter R_a. Force measurement was carried out using the Kistler force measurement device (model 9257B). Measurement results were elaborated in the Matlab environment. In order to evaluate the stress level in workpiece surface layer, an average value of grinding force component measured during the fourth grinding pass was used. Surface roughness parameters were measured with the Hommel-Werke 1000 profile-measurement device.

2.2. Model description

The model was formulated using MLP network (multilayer perception) with one hidden layer. Neuron activation function in hidden and output layers was the arctg function. The model scheme is shown in Figure 4.

Research results, including 114 files, were used for network training. The set was prepared in a way similar to that applied to previous models. Results of the search for the best network are shown in Figure 4.

In order to find the optimum network, the structures with different number of neurons in hidden layer (3–20) were investigated. Average learning, validating and testing errors are shown in the Figure 4.

Table 2. Network learning and testing results

Learning error	Validating error	Testing error
0.01568	0.02914	0.05891

**Network input**   **Hidden layer**   **Output layer**
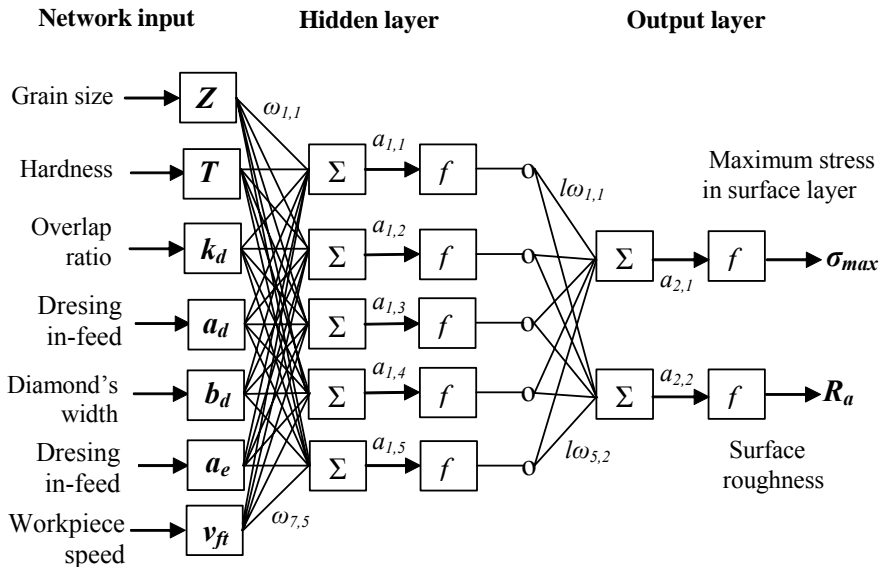
Fig. 4. Neural model of workpiece surface layer state
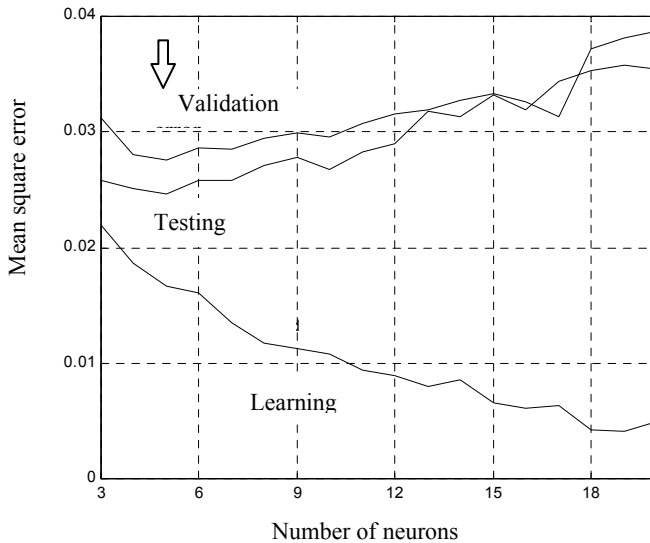
Fig. 5. Errors of different network structures

The network with the smallest average validating error (and five neurons in hidden layer) was selected for the model creation. Errors of selected network are shown in Table 2.

2.3. Example of the model application

On the basis of grinding wheel functional properties model, basic examples of the model function were shown.

In Figure 6, there is shown the relationship between grinding result and wheel characteristics in the case of wheels dressed with the following parameters: in-feed $a_d = 0.015$ mm, overlap ratio $k_d = 1.3$ (width of diamond $b_d = 0.9$ mm).
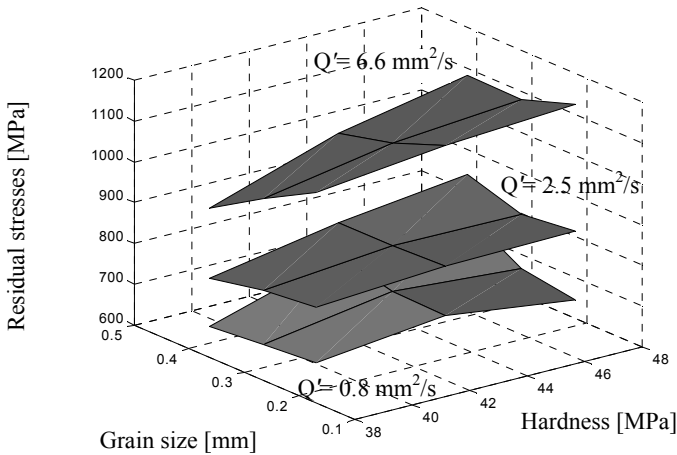

Fig. 6. The relationship between the grinding wheel characteristics
and the stress level in surface layer
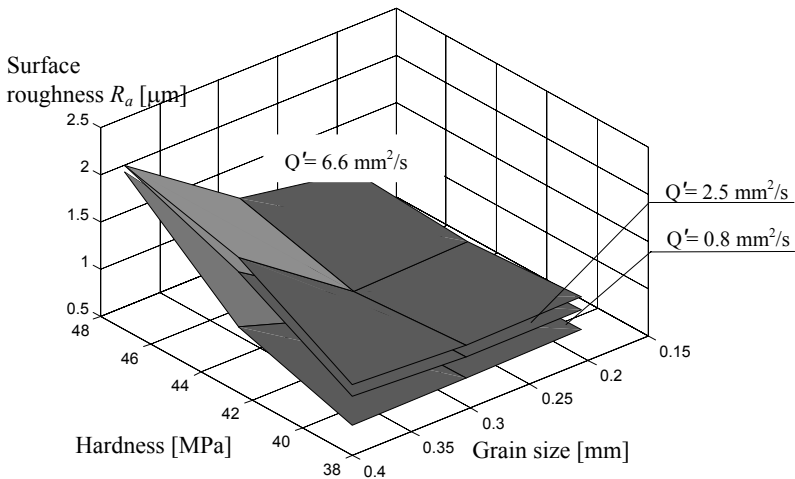
Fig. 7. The relationship between the grinding wheel characteristics
and the surface roughness parameter R_a

Moderate influence of wheel characteristics on stress level in workpiece surface layer was here observed. The increase in the wheel hardness (from 38.5 to 47.5 MPa) caused 5–10% increase in the stress level (higher stress values were achieved in the case of more intensive grinding). Grain-size increase (from 0.196 to 0.390 mm) did not influence clearly the stress values. Only in the case of wheel hardness *J*, the increase in the grain size caused 15% decrease in the stress level (from 1100 to 950 MPa).

The strongest influence was observed in the case of grinding intensity. In the range of parameters shown in Table 1, an average stress increased from 700 MPa (at $Q' = 0.8$ mm²/s) to 1100 MPa (at $Q' = 6.6$ mm²/s).

The influence of grinding intensity on the surface roughness was smaller (see Figure 7). This can prove that the topography of active cutting surface is stable, independently of grinding parameters. The increase in the grinding efficiency (from 0.8 to 6.6 mm²/s) increased the value of the surface roughness parameter R_a by about 0.2 μm. This can be due to the increase in the chatter amplitude in contact zone. The influence of wheel characteristics on the surface roughness parameter R_a was more important (Figure 7).

It was especially visible in the case of wheels with larger grain size and hardness. The influence of those two parameters was similar. The increase in those parameters caused twofold (up to 2 μm) increase in the surface roughness R_a. It should be mentioned that for the wheels with the grain size smaller than 0.29 mm and the hardness smaller than 43 MPa (K) the influence of wheel characteristics on surface roughness was little.

The influence of dressing process on grinding results for 60 K wheel is shown in Figure 8 and Figure 9.
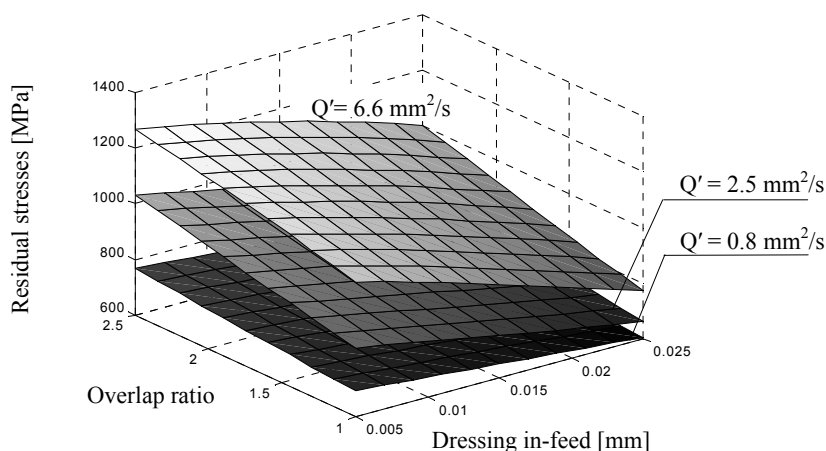

Fig. 8. The relationship between the dressing conditions
and the stress level in workpiece surface layer
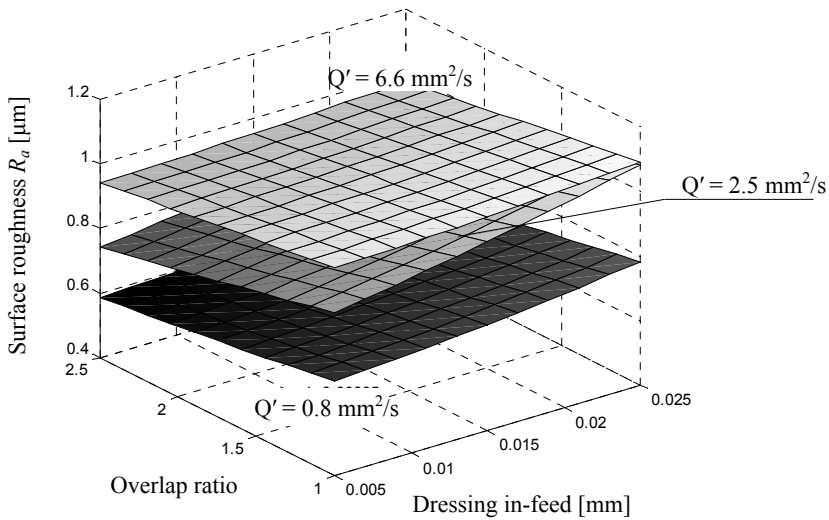
Fig. 9. The relationship between the dressing conditions
and the surface roughness parameter R_a

Proportional relationship between the dressing conditions and the stress level in workpiece surface layer and surface roughness for different grinding intensities is seen. The influences of the dressing in-feed and the overlap ratio were comparable. The decrease in the dressing in-feed and the increase in the overlap ratio k_d increased the residual stress by about $30-40\%$ (Figure 8) and decreased the surface roughness by about $15-20\%$ (Figure 9).

The increase in the grinding intensity resulted also in the increase in the stress level in workpiece surface layer (by about $100-200$ MPa) and in the increase in the surface roughness R_a (by about 0.2 μm).

3. Conclusion

The model of grinding wheel technological properties showed direct relations between wheel preparation state and particular surface layer features. It can be applied as a fast and compact database. It has already been applied in the hybrid advisory system during grinding process planning.

References

[1] Tönshoff H. K., Peters J., Inasaki I., Paul T.: *Modelling and Simulation of Grinding Processes*, Annals of the CIRP, Vol. 41 (2), 1992, pp. 677.
[2] Rowe W. B., Mills B., Qi H. S. Morgan M.N.: *Experimental Investigation of Head Transfer in Grinding*, Annals of the CIRP, Vol. 44 (1), 1995, pp. 329.

[3] Kruszyński B. W.: *Model of Gear-Grinding Process*, Annals of the CIRP, Vol. 44 (1), 1995, pp. 321.

[4] Kruszyński B., Wójcik R.: *Rola gęstości strumienia energii w kształtowaniu warstwy wierzchniej w procesie szlifowania*, XXIV Naukowa Szkoła Obróbki Ściernej, Kraków – Łopuszna, wrzesień 2001, pp. 215.

[5] Wójcik R., Kruszyński B.: *Wpływ gęstości strumienia energii na właściwości warstwy wierzchniej przy różnych odmianach kinematycznych szlifowania*, Projekt Badawczy No. 7T07D 008 15, 2000.

Modelowanie stanu warstwy wierzchniej przedmiotu po szlifowaniu

Przedstawiono przegląd spotykanych w literaturze sposobów prognozowania wyniku szlifowania. Omówiono ich zalety i ograniczenia. Korzystając z metodyki modelowania neuronowego, zaprezentowano sposób prognozowania wyników szlifowania pozostających trwale w przedmiocie obrabianym. Opracowano model pozwalający szybko określić wpływ charakterystyki ściernic i warunków ich ostrzenia na chropowatość powierzchni przedmiotu oraz na maksymalne naprężenia w warstwie wierzchniej. Przedstawiono praktyczną przydatność modelu.

Information about PhD thesis at the Civil Engineering Faculty and the Mechanical Engineering Faculty of the Wrocław University of Technology (WUT)

Title: *Non-stationary oscillations of the container filled with fluid (in Polish)*
Niestacjonarne drgania zbiornika wypełnionego cieczą

Author: Grzegorz Waśniewski
Supervisor: Professor Piotr Konderla
Promoting Council: Scientific Council of the Institute of Civil Engineering of WUT
Reviewers:
    Professor Paweł Śniady, Wrocław University of Technology
    Doctor Marian Klasztorny, Professor of Warsaw University of Technology
Date of PhD thesis presentation: September 29th, 1998
PhD thesis is available in Main Library and Scientific Information Centre of WUT
The paper contains: 101 pages, 28 figs, bibliography, 43 items
Keywords: *shell theory, fluid mechanics, numerical methods, FEM, BEM, Ritz vectors, tower water container, computer program*

Abstract: In the paper, the description of dynamic problem connected with the fluid–structure interaction (FSI) is presented. The system is composed of an elastic shell container filled with fluid. Separate physical and discrete models of both media and global discrete model of whole systems were designed. As far as numerical methods were concerned the hybrid approach was used: discrete equations of shell were obtained by the finite element method (FEM), for fluid region the boundary element method (BEM) was applied. Separate numerical models of two media were connected together using boundary conditions on the fluid–structure contact surface. Energy balance led to dynamic equation of motion in well-known traditional form. An algorithm for the Ritz vectors generation, which were used for orthogonalization of equation of motion, was given. Participation factor of each Ritz vector was formulated. Separate equations of motion were integrated using the Newmark method. In the paper, two numerical examples for tower water container were shown. In the first example, the sensitivity of eigenfrequency of geometrical parameters was calculated. The eigenfrequency of a whole system, the first eigenform of shell and fluid-free surface were shown. The second example presents solution of equation of motion for container under kinematic excitation. The oscillations of shelf and free-surface points were shown. The participation factor for the Ritz vectors and truncation error were calculated. Both examples were analysed in three cases: empty, partially filled and full container.

Title: ***Investigation of reduction of bulk material pressure in silo with flexible walls*** **(in Polish)**
Badania redukcji parcia materiału sypkiego w silosie o ścianach podatnych

Author: Adam Klimek
Supervisor: Professor Sylwester Kobielak
Promoting Council: Scientific Council of Building Engineering of Wrocław University of Technology
Reviewers:
Professor Wiesław Stachurski, Warsaw University of Technology
Professor Mieczysław Kamiński, Wrocław University of Technology
Date of PhD thesis presentation: December 1st, 1999
PhD thesis is available in Main Library and Scientific Information Centre of WUT
The paper contains: 119 pages, 95 figs, bibliography, 44 items
Keywords: *silo, barley, pressure reduction, wall flexibility*

Abstract: The paper deals with the influence of silo wall flexibility on the values of bulk material pressure. Investigations have been conducted on post-tensioned, flat-bottomed test silo model made from reinforced concrete. Silo bin has 4.0 m in height and 1.5 m in diameter and has a structure of Eurosilo type.

This influence of silo wall flexibility on barley pressure was established during filling, centric and eccentric discharges, during simultaneous filling and discharging. Pressure exerted on the silo bottom was measured as well. In the paper, simple theoretical trials to evaluate normal and tangential pressure reductions have been conducted.

Generalization of tests results and nomograms for description of normal and tangential pressures have been given. Calculation procedure and example of calculation of load reduction in the silo of Eurosilo type also have been described.

Based on the test results, the following general conclusions were drawn:

1. During filling an increase in the wall flexibility causes a decrease in normal pressure (up to 15%) and tangential pressure (up to 32%).

2. Reduction of a normal barley pressure is the highest at 0.03% of bulk material strains. Pressure reduction disappears at bulk material strains $> 0.07\%$.

3. Wall flexibility leads to the decrease of the coefficient $K = ph/pv$.

4. Load reduction during silo discharging occurs only in the dead materials zones.

5. Loads standard deviation increases with the increase of wall flexibility.

Title: ***Evaluation and shaping of sewer design based on reliability theory (in Polish)***
Ocena i kształtowanie konstrukcji przewodów kanalizacyjnych w ujęciu teorii niezawodności

Author: Bogdan Przybyła
Supervisor: Doctor Cezary Madryas
Promoting Council: conducted by Professor Jan Biliszczuk
Reviewers:

Professor Marek Roman, Warsaw University of Technology
Professor Paweł Śniady, Wrocław University of Technology

Date of PhD thesis presentation: November 17th, 1999

PhD thesis is available in Main Library and Scientific Information Centre of WUT

The thesis contains: 154 pages, 110 figs, bibliography, 98 items

Keywords: *sewer, reliability, damage, condition assessment, fuzzy sets, inspection, inspection program, network critical channels, mass service system*

Abstract: The paper contains a broad analysis of the kinds of damage done to sewers. The terms: *a state of complete sewer damage* and *a state of partial sewer damage* are defined. A classification of the kinds of sewer damage, including the consequences, is presented. A method enabling the comparison, according to estabilished criteria, of kinds of damage as regards the hazard they pose is proposed.

The sewer reliability description is given, including indices and also basic factors which make it difficult to estimate in practice these indices. Finally particularly reliable measures are specified. Furthermore, some problems of sewer condition assessment are considered. Two own methods, based on the fuzzy set theory, offering different levels of detail are proposed. Some details about the inspection of sewers are presented. A detailed sewer inspection program, combined with assessment methods and including rehabilitation, is proposed.

The concepts of *a system core* and *network critical channels* are introduced. The cost criterion was adopted to find critical costs, but because of difficulties in determining the level of unreliability costs, a practical method of determining network critical channels is presented. The optimum number of repair gangs for the servicing of a sewer network is calculated using mass service models.

Title: ***The influence of the ground movements and deformations on stability of flotation waste dams* (in Polish)**
Wpływ przemieszczeń i deformacji podłoża na stateczność zapór z odpadów flotacyjnych

Author: Marian Kowalczyk
Supervisor: Professor Elżbieta Stilger-Szydło
Promoting Council: Professor Stefan Gałczyński
Reviewers:
    Professor Henryk Bryś, Kraków University of Technology
    Professor Ryszard J. Izbicki, Wrocław University of Technology

Abstract: The paper deals with geotechnical aspects of the storage of copper ore flotation wastes in the Legnica–Głogów Copper District.

Taking advantage of over 30-year observations of movements and deformations of ground and dams made of local materials and flotation wastes, their interpretation was made by using multiple regression method.

Moreover, the influence of drainage of rock mass on the movements and deformations of one working waste storage "Żelazny Most" was estimated, in connection with underground exploitation of copper ore.

The stability on the hightest part of eastern dam was estimated and long-term prognosis of further deformations was made. Aside from engineering methods the method of finite elements was used. In our numerical calculations, we dealt with the ground centre being described as resilient-plastic body model and the border state of centre tension described by the Drucker–Prager rule. In terms of tensions it equals to the Coulomb–Mohr rule. The rheological model of body designed by Kelvin was used for estimating deformations.

Numerical analysis shows that reliable results of estimations might be the basis for calculation of the parameters describing rheological processes in ground. Identification of those parameters calculated by the method of backward analysis might be difficult in laboratory.

Title: ***The influence of axial forces on rail vibrations in CWR-track (in Polish)***
Wpływ sił osiowych na drgania szyn kolejowych w torze bezstykowym

Author: Radosław Mazurkiewicz
Supervisor: Doctor Marek Krużyński, Professor of WUT
Promoting Council: Institute of Civil Engineering
Reviewers:
    Professor Włodzimierz Czyczuła, Kraków University of Technology
    Professor Paweł Śniady, Wrocław University of Technology
Date of PhD thesis presentation: October 18th, 2000
PhD thesis is available in Main Library and Scientific Information Centre of WUT
The paper contains: 239 pages, 136 figs, bibliography, 138 items
Keywords: *CWR-track, axial force, rail vibrations, measurement of axial forces, COSMOS/M, dynamics*

Abstract: In this paper, a phenomenon of free vibrations of a CWR rail forced by percussive impulse applied perpendicularly to the rail head was diagnosed. The proposition that a relationship between the values of axial forces in a rail and a form of free vibrations of this rail exists was established. The aim of this work was to analyse the influence of axial force variations on the quantities which describe rail vibrations, and then to select these parameters for which mathematical formulas circumscribing their connections with axial forces can be stated. It was also intended to check the possibilities of practical evaluating axial forces from the formulas obtained. In the introductory part of the work, different sources of loading rails with axial forces were discussed. A review of existing methods of stresses and axial forces measurement was also described. The fundamental part of the paper are the chapters in which the assumptions, realization and the results of the research done in the exploited CWR track were presented. The method and the results of analysis performed for five parameters describing rail vibrations were presented. The parameters chosen were: vibration period, logarithmic decrement of damping, predominant frequency, number of amplitudes exceeding given level of accelerations, and time of vibration fading. In the further part of the paper, descriptions of several alternative models of a permanent way were included. These models served to do computer-aided simulations of free vibrations of a rail. The succeeding steps of models' design were presented, and the results were discussed.

Title: *The influence of buildability on effectiveness of building enterprises in the case of buildings' thermal modernisation (in Polish)*
Wpływ jakości technologicznej na efektywność przedsięwzięć budowlanych na przykładzie termomodernizacji budynków

Author: Mariusz Rejment
Supervisor: Professor Ewa Marcinkowska
Promoting Council: Professor Antoni Biegus
Reviewers:
    Professor Kazimierz Cieszyński, Warsaw University of Technology
    Professor Juliusz Mrozowicz, Wrocław University of Technology
Date of PhD thesis presentation: October 17th, 2001
PhD thesis is available in Main Library and Scientific Information Centre of WUT
The paper contains: 132 + 121 pages, 10 figs, bibliography, 199 items
Keywords: *economic effectiveness, buildability, thermal overcladdings*

Abstract: The main aim of the monograph was to recognise and estimate the influence of thermal overcladding of buildings on economic effectiveness of building thermal modernisation. The research on technical conditions of thermal overcladdings involved 497 apartment buildings in Wrocław. The results were used to form the database of technical conditions of building thermal overcladdings. The reason–effect relation for faults and defects was established using e.g. the statistical methods of data analysis. Three features describing thermal overcladding of buildings were separated. The features were used to indicate the defects caused by low buildability of thermal overcladdings. Next, the model was designed to estimate the influence of thermal overcladding buildability on ecomnomic effectiveness of building thermal modernisation. The model designed was based on the economic formula NPV (Net Present Value). The results obtained according to the model enabled us to accomplish the main aim of work and to prove the thesis.

Information for Authors

Send to: *Archives of Civil and Mechanical Engineering*
Polish Academy of Sciences, Wrocław Branch
Podwale 75, 50-414 Wrocław, Poland

Archives of Civil and Mechanical Engineering (ACME) publishes both theoretical and experimental papers which explore or exploit new ideas and techniques in the following areas: structural engineering (structures, machines and mechanical systems), mechanics of materials (elasticity, plasticity, rheology, fatigue, fracture mechanics), materials science (metals, composites, ceramics, plastics, wood, concrete, etc., their structures and properties, methods of evaluation), manufacturing engineering (process design, simulation, diagnostics, maintenance, durability, reliability). In addition to research papers, the Editorial Board welcome: state-of-the-art reviews of specialized topics, letters to the Editor for quick publication, brief work-in-progress reports, brief accounts of completed doctoral thesis (one page is maximum), and bibliographical note on habilitation theses (maximum 250 words). All papers are subject to a referee procedure, except for letters, work-in-progress reports and doctoral and habilitation theses, which are briefly reviewed by the Editorial Board.

The papers submitted have to be unpublished works and should not be considered for publication elsewhere.

The Editorial Board would be grateful for all comments on the idea of the journal.

Submit three copies, each complete with abstract, tables, and figures.
Detailed information about the Journal on web:
  http://www.pan.wroc.pl
  www.ib.pwr.wroc.pl/wydzial/czasopismoACME.html
  http://www.wmech.pwr.wroc.pl